Title

Influence of Interfacial Rheology on Instabilities of Multiphase Flows

Author

Li, Jiayu

Publication Date

2023

Peer reviewed|Thesis/dissertation

Influence of Interfacial Rheology on Instabilities of Multiphase Flows
By

JIAYU LI
DISSERTATION

Submitted in partial satisfaction of the requirements for the degree of

DOCTOR OF PHILOSOPHY

in

Chemical Engineering

in the

OFFICE OF GRADUATE STUDIES

of the

UNIVERSITY OF CALIFORNIA

DAVIS

Approved:

Harishankar Manikantan, Chair

Jiandi Wan

Stephanie Dungan

Committee in Charge

2023

Contents

List of Figures

Abstract

Influence of Interfacial Rheology on Instabilities in Multiphase Flows

Liquid-liquid interfaces are common in both nature and industry, arising in foams, respiratory droplets, thin films, coatings, and inkjet printing. Generally, surfactants are used to stabilize the interface against rupture and coalescence. However, interfacial instabilities can still occur even in the presence of surfactants. As surfaces deform, surfactants alter the surface flows by causing gradients in surface tension and inducing additional surface rheological effects. Quantitatively characterizing these effects has been a key research interest in the past decades. Our work examines the effects of surface rheology on the interfacial instabilities in two areas. First, we demonstrate the stabilizing effect of surface rheology in radial viscous fingering using linear stability analysis. We quantify the growth rates of perturbations to show that surface viscosity slows the growth of the instability and results in thicker fingers. In addition, we highlight the quantitative changes that are predicted to occur when a typical surface viscous surfactant is present. Our second area focuses on the effect of soluble surfactants on the instabilities in liquid jets. We use linear stability analysis to quantitatively show the stabilizing effects of increasing Marangoni stresses, surfactant adsorption and desorption time, and surface viscous stresses of soluble surfactants in jet fluid. In addition, we identify the surface viscous-like force contributed by the Marangoni flow with a finite adsorption and desorption time interval. Our work suggests that surface rheology should be considered as a potential factor in future models and experiments involving complex surfactant-laden interfaces.

Acknowledgments

I would like to express my gratitude to the individuals who have helped and supported me along the journey to the completion of my dissertation. First and foremost, I am deeply grateful to my PhD advisor, Professor Harishankar Manikantan, for his exceptional guidance, unwavering support, and insightful feedback throughout the entire research process. His dedication and patience made the transition much easier especially during the early stages of my PhD journey. His vast knowledge and expertise in the field have been instrumental in shaping this thesis and elevating its quality. I would also like to extend my sincere appreciation to the members of my thesis committee, Prof. Jiandi Wan and Prof. Stephanie Dungan, for their feedback throughout the process. Next, I would like to acknowledge the support and assistance I have received from the staff and faculty at Chemical Engineering. Furthermore, I want to thank all the colleagues and friends whom I met during my time in Davis for their support, encouragement, and stimulating discussions. In addition, I would like to express my gratitude to my friends, Spencer, Arnold, Rex, Ian, and especially my girlfriend, Ashley, for their feedback and encouragement. I also want to thank my “goodest” boy Miko, and my sister’s cats Bruce and Johnny, for their involuntary emotional support. Lastly, I would like to express my profound gratitude to my parents Pengcheng and Xiaohong, and my sister, Jiayao, for their unconditional love, unwavering support, and constant encouragement throughout this entire academic endeavor. I would not be the man I am today without them, and I am blessed to have them in my life.

Chapter 1 Introduction

1.1. Preamble

My dissertation contains two of my publications and a summary of some unfinished work I explored during my time at Davis. Other work focusing on the fluid rheology of bacteria biofilms is not included. Each publication in the dissertation focuses on the effect of surface rheology on the surface instability of a specific application. The current section aims to provide a general overview of the history of surface rheology and some of the recent developments. Each chapter includes more detailed introductions on the specific field.

1.2. Introduction

Fluid-fluid interfaces are common in both nature and industry, arising commonly in foams, respiratory droplets, thin films, coatings, and flotation. In most cases, stabilizing agents such as fatty acids, alcohols, proteins, and particles populate the interface. These surface-active agents or ‘surfactants’ modify the energetics and the dynamics of complex interfaces, stabilizing interfaces against rupture and coalescence. However, interfacial instabilities can still occur even in the presence of surfactants. These instabilities are often undesirable and present challenges in processes such as oil recovery, groundwater movement, and carbon dioxide sequestration in saline aquifers. In this work, we explored the impact of surface rheology on the instabilities of interfaces in viscous fingering and jet fluid. We cover some of the fundamentals of surface rheology and summarize the progress made so far in each field for the rest of the section.

Before we mention surface rheology, we will talk briefly about Marangoni flows. Marangoni flow is one of the most significant surface transport phenomena and is induced by surfactant surface tension gradients [1,2]. Plateau first observed the effect but attributed the surface resistance to a ‘superficial viscosity.’ Marangoni and Gibbs later recognized the phenomenon and elucidated the

effect with the argument of surface tension gradients [1]. The comprehensive mathematical analysis of the Marangoni effects was presented years later when Levich justified that Marangoni stress caused rising bubbles to behave as rigid spheres [3,4]. In recent decades, however, it becomes more evident that stabilizers also confer rheological properties to the interface and alter the behavior of surface flow [5–8]. Thus, separating and accounting for the influences of both Marangoni stress and surface rheological stresses on surface flows correctly has been an ongoing challenge in the studies of interfacial transport phenomena [8,9].

The theoretical development of surface rheology took a few decades to begin gaining more traction and becoming more prevalent. Boussinesq was the first to propose the incorporation of surface viscosities in interfacial transport equations theoretically in 1913. He explained the rigid-sphere-like behaviors of rising bubbles by ascribing the surface flow resistance to surface rheology. Boussinesq hypothesized the existence of a thin interfacial layer and set up a two-dimensional (2D) analog of three-dimensional (3D) Newtonian fluid with intrinsic surface shear (η_s) and dilatational (κ_s) viscosities [1,10]. While the original equations by Boussinesq were limited to the specific study, Scriven generalized the framework by treating the interface as an isotropic fluid continuum of any shape in 1960 [1,8,11]. The resulting equations describing a Newtonian fluid interface undergoing continuous change are usually referred to as the Boussinesq-Scriven model [1,11], which is commonly used to describe surface rheology in recent research works.

Recent experiments have unambiguously identified surface rheological stresses that may arise on complex interfaces [2,5–8]. Much like their 3D counterparts, surface viscosities resist the deformation of the 2D manifold that makes up the fluid interface. Indeed, surface shear viscosity ‘immobilizes’ the interface, enhancing film stability during the drainage motion of foams [12,13] and thin coatings [14], and retarding the buoyant rise of droplets [15]. However, detecting reliable

surface rheological signatures remains difficult in experiments as interfacial flows drive mixed surface deformations and a combination of surfactant transport properties, including surface convection, bulk diffusion, and adsorption/desorption. For example, insoluble surfactants modify the surface flow to behave as incompressible, modifying the resistance to the motion of an interfacial probe [2,16,17]. Demarcating a genuine interfacial rheological response is thus challenging, giving rise to a wide range of inferred values of surface viscosities [18]. Nevertheless, strategies to clearly measure surface viscous stresses via careful experimental designs of flow geometries, length scales, and time scales have been successful in recent years. The role of surface shear viscosity, for example, has been established using rotational flow geometries that only shear the interface and do not give rise to Marangoni effects [6,19]. Micro-rheological techniques have also established the existence of surface excess viscosities [20–22], with recent works tying together the micro- and macro-viscosity of complex interfaces [23]. Despite the current progress, however, properly differentiating between an 'intrinsic' and 'apparent' surface dilatational viscosity remains an open question, as systems that contain Marangoni flows with a finite adsorption or desorption time interval might introduce a surface-viscous-like force [2,3,9,16–18,24,25].

The coupling between surface and bulk (or subphase) flows presents yet another subtlety in the interpretation of systems with a non-trivial surface viscosity. The relative strength of surface viscous stresses to bulk viscous stress is typically quantified by the Boussinesq number,

$$Bq = \frac{\eta_s}{\eta L}, \tag{1}$$

where η_s is the surface shear viscosity, η is the bulk viscosity, and L is the characteristic length scale of the system. Alternatively, a dilatational surface viscosity, κ_s, may be used if the interface

resists dilation. Surface shear viscosities are typically measured using interfacial magnetic rods [19], micro-buttons [6,26], or with Couette and double-wall Couette rheometers [7,27], whereas surface dilatational viscosities are measured with oscillatory bubble/drop-based methods [7,28].

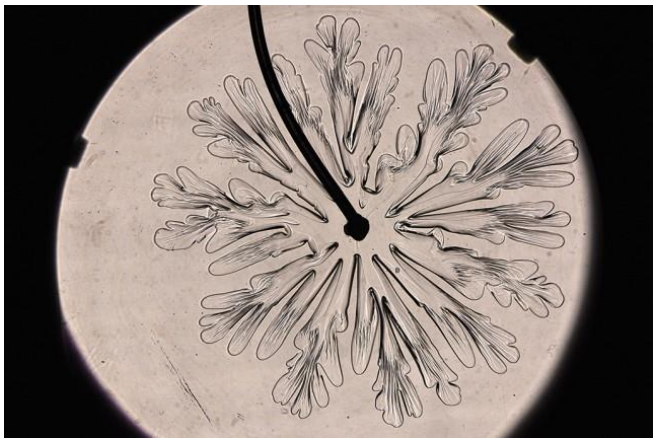

Figure 1.1. The formation of viscous fingers upon fluid displacement [29].

One instability that occurs commonly in multiphase fluid systems is viscous fingering: unstable finger-like protrusions develop as a less viscous fluid invades a more viscous fluid in confined geometry as shown in Fig.1.1 [29]. Viscous fingering is often observed in the petroleum industry, which uses Enhanced oil recovery (EOR) techniques to improve volumetric sweeping efficiency. Gas EOR methods are commonly used due to their improved microscopic sweep in the pores than waterflood methods. However, the oil recovery of gas EOR methods remains low due to channeling and viscous fingering [30]. Using foams instead of gas provides a potential solution to the problems in gas EOR methods: foams increase the effective viscosity of the displacement fluid (foams), block the high-permeable swept zones, and reduce the interfacial tensions due to surfactants at the surface, leading to the decrease in capillary forces [31]. When surfactants adsorb

at the fluid surface, they confer rheological properties to the surface that affect fluid surface deformation.

Saffman and Taylor were the first to quantify the fingering instability using a Hele-Shaw cell to simulate a porous medium [32]. The qualitative features of viscous fingering are now well understood. The exact details of the size and rate of growth of viscous fingers depend critically on the shape of the invading interface [33–38], geometry [39,40] and deformability [41] of the walls, and the presence of external fields that impact the flow [42]. However, despite decades of work, the role of surface rheological stresses on the Saffman-Taylor instability is yet unknown. Indeed, recent studies show asphaltenes and related complexes on oil-water interfaces strongly resist interfacial deformation [14,43–47], potentially modifying or even suppressing the instability. While more and more literature studies have begun to recognize and characterize the surface excess rheological stresses, no study has focused on the surface rheological impact on viscous fingering. In addition, the fundamental understanding of surface viscous contributions to fluid surface deformation is still lacking. Miscommunication often occurs in experiments associated with 1D deformations of foam liquid channels as contributions from both surface shear and dilatational viscosities were mistakenly treated as originating from a single surface viscosity [18,48]. Our published work provides here a quantitative description of the role of surface viscosity on the growth of viscous fingers in a system that mimics the fluid-fluid displacement in porous media.

Another case of interfacial instability is the instability of jet fluid. While the impact of surfactants on jet fluid stability has long been studied [49–51], the understanding of surface rheological effect on the dynamics of Newtonian jet fluid is limited [52,53]. The lack of understanding prompts the need to further understand the fundamental science behind the role of surface rheology. It has been well established that the presence of surfactants plays a role in the process of liquid jet thinning

and the formation of the satellite beads [53–61]. A few groups of researchers have identified that the presence of insoluble surfactants lowers the thinning rate of liquid jets [52,56,62,63]. In addition, some have proposed analytical solutions for the thinning rate that was affected by the surface rheological effects [64,65]. The work on the liquid jets with soluble surfactants remains mainly experimental. Soluble surfactants in liquid jets are found to increase the jet-breaking lengths in addition to playing a role in the formations and the sizes of the satellite beads [53,55,58,66–68]. However, the fundamental science and understanding of soluble surfactants in jet fluid stability are still lacking, specifically the adsorption and desorption kinetics of the soluble surfactants near the interface. In this work, we investigated the impact of soluble surfactants on a Newtonian liquid jet. We isolated and quantitatively showed the effects of the Marangoni stresses, the net flux of surfactant adsorption and desorption, and the surface viscous stresses via linear stability analysis. In addition, we identified the surface viscous-like force contributed by the Marangoni flow with a finite adsorption and desorption time interval. Lastly, we showed numerically that we can generalize the results from the linear stability analysis to the systems governed by established models such as Langmuir and Frumkin [69,70].

Chapter 2 Influence of surface rheology on viscous fingering

2.1. Preface

In this chapter, I am reprinting an article I published on the influence of surface rheology on viscous fingering; DOI: 10.1103/PhysRevFluids.6.074001. It is somewhat surprising that no one has investigated the impact of surface rheological effect in Saffman-Taylor instability. In this work, we demonstrate, for the first time, the stabilizing effect of surface rheology in radial viscous fingering using linear stability analysis. We present the equations governing the dynamics on the interface using the Boussinesq-Scriven model [11] in cylindrical coordinates. We analyze the effect of surface rheology on the growth of interfacial perturbations in a radial Hele-Shaw cell and illustrate that surface viscous stresses have a stabilizing effect: the most unstable wavenumber as well as the corresponding growth rate decreases with increasing surface viscosity. Based on these, we postulate that surface viscous resistance slows the growth of the instability and results in thicker fingers. Finally, we also show that incorporating surface rheology in radial viscous fingering potentially better captures past experimental data. Our work suggests that surface rheology should be considered as a potential factor in future models and experiments involving complex surfactant-laden interfaces.

2.2. Introduction

Fluid-fluid interfaces are common in both nature and industry, arising commonly in foams, respiratory droplets, thin films, coatings, and flotation. In most cases, stabilizing agents such as fatty acids, alcohols, proteins, and particles populate the interface. These surface-active agents or ‘surfactants’ modify the energetics and the dynamics of complex interfaces, stabilizing interfaces against rupture and coalescence. However, interfacial instabilities can occur even in the presence

of surfactants. These instabilities are often undesirable and present challenges in processes such as oil recovery, groundwater movement, and carbon dioxide sequestration in saline aquifers.

One such instability that occurs commonly in multiphase fluid systems is viscous fingering: unstable finger-like protrusions develop as a less viscous fluid invades a more viscous fluid in confined geometry. Saffman and Taylor were the first to quantify this instability using a Hele-Shaw cell to simulate a porous medium [32]. The qualitative features of viscous fingering are now well understood. The exact details of the size and rate of growth of viscous fingers depend critically on the shape of the invading interface [33–38], geometry [39,40] and deformability [41] of the walls, and the presence of external fields that impact the flow [42]. However, despite decades of work, the role of surface rheological stresses on the Saffman-Taylor instability is yet unknown. Indeed, recent studies show asphaltenes and related complexes on oil-water interfaces strongly resist interfacial deformation [14,43–47], potentially modifying or even suppressing the instability. We present here a quantitative description of the role of surface viscosity on the growth of viscous fingers in a system that mimics the fluid-fluid displacement in porous media.

Recent experiments have unambiguously identified surface rheological stresses that may arise on complex interfaces [2,5–8]. Much like their 3D counterparts, surface viscosities resist the deformation of the 2D manifold that makes up the fluid interface. Indeed, surface shear viscosity ‘immobilizes’ the interface, enhancing film stability during the drainage motion of foams [12,13] and thin coatings [14], and retarding the buoyant rise of droplets [15]. However, detecting reliable surface rheological signatures remains difficult in experiments as interfacial flows drive mixed surface deformations and a combination of surfactant transport properties, including surface convection, bulk diffusion, and adsorption/desorption. For example, insoluble surfactants modify the surface flow to behave as incompressible, modifying the resistance to the motion of an

interfacial probe [2,16,17]. Demarcating a genuine interfacial rheological response is thus challenging, giving rise to a wide range of inferred values of surface viscosities [18]. Nevertheless, strategies to clearly measure surface viscous stresses via careful experimental designs of flow geometries, length scales, and time scales have been successful in recent years. The role of surface shear viscosity, for example, has been established using rotational flow geometries that only shear the interface and do not give rise to Marangoni effects [6,19]. Micro-rheological techniques have also established the existence of surface excess viscosities [20–22], with recent works tying together the micro- and macro-viscosity of complex interfaces [23]. Despite the current progress, however, properly differentiating between an 'intrinsic' and 'apparent' surface dilatational viscosity remains an open question, as systems that contain Marangoni flows with a finite adsorption or desorption time interval might introduce a surface-viscous-like force [2,3,9,16–18,24,25].

The coupling between surface and bulk (or subphase) flows presents yet another subtlety in the interpretation of systems with a non-trivial surface viscosity. The relative strength of surface viscous stresses to bulk viscous stress is typically quantified by the Boussinesq number,

$$Bq = \frac{\eta_s}{\eta L}, \tag{2.1}$$

where η_s is the surface shear viscosity, η is the bulk viscosity, and L is the characteristic length scale of the system. Alternatively, a dilatational surface viscosity, κ_s, may be used if the interface resists dilation. Surface shear viscosities are typically measured using interfacial magnetic rods [19], micro-buttons [6,26], or with Couette and double-wall Couette rheometers [7,27], whereas surface dilatational viscosities are measured with oscillatory bubble/drop-based methods [7,28].

In this work, we illustrate, for the first time, the role of surface rheology in radial viscous fingering. We first present the equations governing the dynamics on the interface using the Boussinesq-Scriven model [11] in cylindrical coordinates. We then analyze the effect of surface rheology on the growth of interfacial perturbations in a radial Hele-Shaw cell and illustrate that surface viscous stresses have similar stabilizing effects on the interface as surface tension. We predict the expected finger width that might be observed in experiments and demonstrate that stronger surface viscous effects result in slower growth of fingers and larger finger width. We end with a comparison to past theoretical models and the quantitative changes that are predicted to occur when a typical surface viscous surfactant is present.

2.3. Governing equations

Thin fluid films confined between parallel walls (Fig. 2.1) are mathematically analogous to flow in a porous medium and are commonly used to simulate and analyze fluid-fluid displacement problems [32,33]. The fluid velocity in such a Hele-Shaw cell follows Darcy's law:

$$\boldsymbol{u}_j = -M_j \boldsymbol{\nabla} p_j, \qquad j = 1,2, \tag{2.2}$$

where M_j is the fluid mobility and p_j is the pressure. We follow the notations in Fig. 2.1 where fluid 1 invades fluid 2. Mobility depends on the gap width between the plates of the Hele-Shaw cell, b, and the bulk viscosity, η_j:

$$M_j = \frac{b^2}{12\eta_j}, \qquad j = 1,2. \tag{2.3}$$

Defining $\phi_j = M_j p_j$ as the velocity potential to build on previous works in this geometry [38,71], we express the fluid velocity as

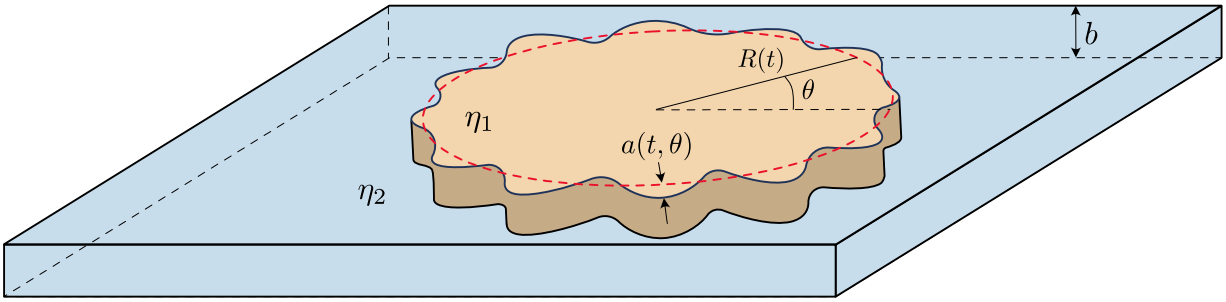

Figure 2.1. Geometry of a less viscous fluid (phase 1) radially invading a more viscous fluid (phase 2). η_j, with $j = 1,2$, is the fluid viscosity, b is the gap width of the Hele-Shaw cell, $R(t)$ is the interfacial radius in the base state, and $a(t,\theta)$ is the perturbed displacement around $R(t)$.

$$\boldsymbol{u}_j = -\boldsymbol{\nabla}\phi_j = -\frac{\partial \phi_j}{\partial r}\hat{\boldsymbol{e}}_r - \frac{1}{r}\frac{\partial \phi_j}{\partial \theta}\hat{\boldsymbol{e}}_\theta, \qquad j = 1,2. \tag{2.4}$$

Surface rheological stresses enter as boundary conditions to the velocity potentials. In what follows, we outline the Boussinesq-Scriven model for a Newtonian interface.

2.3.1. Boussinesq-Scriven model in cylindrical coordinates

The mathematical description of a complex interface with its 2D viscosities goes back to Boussinesq, who sought to explain the rigid-sphere-like behavior of rising bubbles by ascribing the immobilization of the fluid interface to surface rheology. Boussinesq hypothesized the existence of a thin interfacial layer and set up a 2D analog of 3D Newtonian fluid with intrinsic surface shear (η_s) and dilatational (κ_s) viscosities [1,10]. Scriven generalized the framework by treating the interface as an isotropic fluid continuum that comprises a 2D manifold of any shape [1,8,11]. The resulting equations describing a Newtonian fluid interface undergoing continuous change are usually referred to as the Boussinesq-Scriven model [1,11].

The model originates from the 2D form of Cauchy's momentum conservation equation at the interface [72],

$$\rho_s \frac{D\boldsymbol{u}}{Dt} = \boldsymbol{n} \cdot [\![\boldsymbol{\sigma}]\!] + \boldsymbol{\nabla}_s \cdot \boldsymbol{\sigma}_s, \tag{2.5}$$

where ρ_s is the surface mass density, $[\![\boldsymbol{\sigma}]\!] = \boldsymbol{\sigma}_2 - \boldsymbol{\sigma}_1$ is the hydrodynamic stress jump across the interface. $\boldsymbol{n}$ is the normal vector pointing towards the outer phase and $\boldsymbol{\nabla}_s = \boldsymbol{I}_s \cdot \boldsymbol{\nabla} = (\boldsymbol{I} - \boldsymbol{nn}) \cdot \boldsymbol{\nabla}$ is the surface gradient operator.

Stresses on the interface originate from surface tension γ and surface excess rheological stresses [2,11]:

$$\boldsymbol{\sigma}_s = \gamma \boldsymbol{I}_s + \boldsymbol{\tau}_{rheol}, \tag{2.6}$$

where $\boldsymbol{I}_s = \boldsymbol{I} - \boldsymbol{nn}$ is the surface identity tensor and $\boldsymbol{\tau}_{rheol}$ captures the deviatoric relationship between stresses and strain rates on the interface.

Substituting Eq. (2.6) into Eq. (2.5), we obtain

$$\rho_s \frac{D\boldsymbol{u}}{Dt} + \boldsymbol{n} \cdot \boldsymbol{\sigma}_1 - \boldsymbol{n} \cdot \boldsymbol{\sigma}_2 = \boldsymbol{\nabla}_s \gamma - \gamma (\boldsymbol{\nabla}_s \cdot \boldsymbol{n}) \boldsymbol{n} + \boldsymbol{\nabla}_s \cdot \boldsymbol{\tau}_{rheol}, \tag{2.7}$$

The constitutive relation for the surface stress tensor $\boldsymbol{\tau}_{rheol}$ depends on the details of the rheological response of the interface. We will consider the 2D Newtonian approximation proposed by Boussinesq and generalized by Scriven, wherein $\boldsymbol{\tau}_{rheol}$ takes the form [2,11]

$$\boldsymbol{\tau}_{rheol} = [(\kappa_s - \eta_s) \boldsymbol{\nabla}_s \cdot \boldsymbol{u}] \boldsymbol{I}_s + \eta_s [\boldsymbol{\nabla}_s \boldsymbol{u} \cdot \boldsymbol{I}_s + \boldsymbol{I}_s \cdot (\boldsymbol{\nabla}_s \boldsymbol{u})^T], \tag{2.8}$$

where η_s is the surface shear viscosity, κ_s is the intrinsic surface dilatational viscosity, and $\boldsymbol{u} = \boldsymbol{u}_1 = \boldsymbol{u}_2$ is the fluid velocity at the interface. Note that the intrinsic surface dilatational viscosity, κ_s, is a property of surfactant in contrast to the apparent surface dilatational viscosity, which might arise due to a finite adsorption or desorption time [2,25]. η_s and κ_s are exact surface analogs of the fluid viscosity and dilatational viscosity that appear in the 3D deviatoric stress tensor,

respectively. Unlike 3D fluids, however, interfaces are generally easier to compress and, thus, exchange mass and momentum with the bulk phase(s).

Substituting Eq. (2.8) into Eq. (2.7) and simplifying, we obtain:

$$\rho_s \frac{D\boldsymbol{u}}{Dt} - (\boldsymbol{n}\cdot\boldsymbol{\sigma}_2 - \boldsymbol{n}\cdot\boldsymbol{\sigma}_1) = \boldsymbol{\nabla}_s\gamma - \gamma(\boldsymbol{\nabla}_s\cdot\boldsymbol{n})\boldsymbol{n} + (\kappa_s - \eta_s)\boldsymbol{\nabla}_s(\boldsymbol{\nabla}_s\cdot\boldsymbol{u}) - (\kappa_s - \eta_s)(\boldsymbol{\nabla}_s\cdot\boldsymbol{u})[\boldsymbol{\nabla}_s\cdot\boldsymbol{n}]\boldsymbol{n} + \boldsymbol{\nabla}_s\cdot\{\eta_s[\boldsymbol{\nabla}_s\boldsymbol{u}\cdot\boldsymbol{I}_s + \boldsymbol{I}_s\cdot(\boldsymbol{\nabla}_s\boldsymbol{u})^T]\}, \quad (2.9)$$

which is the general Boussinesq-Scriven equation [11]. The first term on the left-hand side (LHS) of Eq. (2.9) captures the fluid and surfactant inertia, which is negligible in overdamped or low-Reynolds-number flows. The second term on the LHS represents the coupling to the subphase via viscous traction from the bulk fluid. The first term on the right-hand side (RHS) of Eq. (2.9) depicts the Marangoni stress, which can also be expressed in terms of surface pressure, $\boldsymbol{\nabla}_s\gamma = -\boldsymbol{\nabla}_s\Pi$, where the surface pressure is $\Pi = \gamma_0 - \gamma$, with γ_0 being the surface tension of a clean interface. The second term on the RHS represents the curvature pressure in the normal direction. In a static system with no surface rheological stresses, Eq. (2.9) simplifies to the Young-Laplace equation. Additionally, in systems containing only insoluble surfactants, the surface divergence of $\boldsymbol{u}$ is zero as interfaces are incompressible [2,16].

We wish to connect Eq. (2.9) to the radial geometry of an initially circular bubble invading a Hele-Shaw cell. Neglecting the inertial term in Eq. (2.9), simplifying the unit normal vector to $\boldsymbol{n} = \hat{\boldsymbol{e}}_{\boldsymbol{r}}$, and expressing the velocity in terms of potential, the normal stress balance becomes (Appendix A.2),

$$-(p_1 - p_2) - 2\eta_1 \frac{\partial^2 \phi_1}{\partial r^2} + 2\eta_2 \frac{\partial^2 \phi_2}{\partial r^2} = -\gamma \left(\frac{2}{b} + \boldsymbol{\nabla_s} \cdot \boldsymbol{n}\right)$$
$$- \left[(\kappa_s - \eta_s)(\boldsymbol{\nabla_s} \cdot \boldsymbol{n}) + 2\eta_s \frac{1}{r}\right]\left(-\frac{1}{r^2}\frac{\partial^2 \phi_1}{\partial \theta^2} - \frac{1}{r}\frac{\partial \phi_1}{\partial r}\right), \quad (2.10)$$

where $2/b$ is the additional correction for the transverse curvature in a Hele-Shaw cell of gap size b. Equation (2.10) illustrates a key feature of one-dimensional deformation: azimuthally stretching a cylindrical interface is an anisotropic deformation and excites both shear and dilatational responses. A surfactant with finite surface shear viscosity alone will therefore resist a purely stretching deformation in this geometry. Equation (2.10) serves as a boundary condition to the governing equation for ϕ_j [Section 2.2].

We make the common assumption that surface tension is spatially uniform and do not consider the effect of Marangoni stress in this study. This assumption is valid when the scale of tangential flow u_θ driven by the surface tension gradients is much smaller than the normal velocity u_r. In the case of soluble surfactants, this assumption is also valid when the rate of adsorption/desorption is much faster than the rate of deformation to maintain a near-equilibrium surface coverage. However, finite-time adsorption or desorption of soluble surfactants at the interface leads to local variations in surface tension, introducing an apparent dilatational viscosity, $\kappa_{s,app}$, which further complicates the system [2,25]. Analytically tracking these contributions would require solving a surfactant conservation equation simultaneously with Eq. (2.10). For simplicity, we assume constant surface coverage in what follows. In addition, note that this analysis uses the Boussinesq-Scriven model with a Newtonian constitutive relation for the interface. Insoluble surfactants undergo phase transitions upon compression and can display strongly non-Newtonian behavior [2,26,74]. For simplicity and as the first step towards illustrating the effect of interfacial rheology in this viscous

fingering, we will assume that surface viscosities remain constant so that the Newtonian model is valid.

2.3.2. Radial viscous fingering

In a typical radial viscous fingering experiment, a less viscous fluid 1 is injected at a constant volumetric flow rate Qb at the center of a Hele-Shaw cell filled with a more viscous fluid 2, as shown in Fig. 2.1. The circular domain of the less viscous fluid 1 destabilizes as it expands and forms finger-like protrusions. The mass balance on the fluid in the Hele-Shaw cell is

$$\pi R^2 b - \pi R_0^2 b = Qbt, \tag{2.11}$$

where R is the radius of the unperturbed interface, R_0 is the initial radius, and b is the gap width of the Hele-Shaw cell. Here, Q is the area flow rate (per unit gap width) and is held constant in this study. The system is dynamically stable until a critical radius R_c, beyond which instability occurs leading to finger formation.

We are primarily interested in the mechanisms of destabilization at R_c and will approach this problem in terms of a linear stability analysis. In particular, we seek to investigate the early stages of the transition from an undisturbed interface to the appearance of sinusoidal disturbances when the fluid interface has a non-trivial surface viscosity. To this end, we define the velocity potential as $\phi_j = \phi_{0j} + \phi_{1j}$, where ϕ_{0j} is the potential in the base state and ϕ_{1j} is the potential in the perturbed state. The velocity potential satisfies the continuity equation, $\nabla^2 \phi_j = 0$.

2.3.2.1 Base state

The unperturbed base state corresponds to fluid 1 maintaining a circular shape of radius $R(t)$ as it invades fluid 2. In such a base state, the kinematic condition at the interface $r = R(t)$ is

$$\frac{\partial r}{\partial t} = \frac{\partial \phi_{0j}}{\partial r}\bigg|_{r=R}. \tag{2.12}$$

Solving Eq. (2.11) and Eq. (2.12) gives

$$\frac{\partial \phi_{0j}}{\partial r} = -\frac{Q}{2\pi r}. \tag{2.13}$$

In the base state, the radial curvature in the projected plane is $\boldsymbol{\nabla} \cdot \boldsymbol{n} = 1/R(t)$. The normal stress balance for the base-state flow is then given by Eq. (2.10),

$$\begin{aligned} -(p_{01} - p_{02})|_{r=R} - 2\eta_1 \frac{\partial^2 \phi_{01}}{\partial r^2}\bigg|_{r=R} + 2\eta_2 \frac{\partial^2 \phi_{02}}{\partial r^2}\bigg|_{r=R} \\ = -\gamma\left(\frac{2}{b} + \frac{1}{R(t)}\right) - \left(\frac{\kappa_s + \eta_s}{R(t)}\right)\left(-\frac{1}{r}\frac{\partial \phi_{01}}{\partial r}\right)\bigg|_{r=R}. \end{aligned} \tag{2.14}$$

2.3.2.2 Perturbed state

We introduce perturbations about the base state in the form of an unsteady radial displacement around $R(t)$ with azimuthally varying amplitude:

$$a(t, \theta) = A_0 f(t) \exp(in\theta), \tag{2.15}$$

where $f(t)$ depicts the growth rate of a mode of wavenumber n and $|A_0| \ll R(t)$. Here, n is an integer and roughly represents the number of viscous fingers along the interface in the linear limit. The radius of the perturbed interface is the sum of the radius at the base state and the perturbation:

$$r = R(t) + a(t, \theta). \tag{2.16}$$

Retaining only terms to $O(a)$, the kinematic condition at the interface becomes

$$\frac{\partial r}{\partial t} = \frac{\partial (R + a)}{\partial t} = \frac{\partial \phi_{0j}}{\partial r}\bigg|_{r=R} + a\frac{\partial^2 \phi_{0j}}{\partial r^2}\bigg|_{r=R} + \frac{\partial \phi_{1j}}{\partial r}\bigg|_{r=R}. \tag{2.17}$$

Solving the Laplace equation for the perturbed potential and satisfying the kinematic condition Eq. (2.17) gives [38,71],

$$\phi_{1j}(r,\theta,t) = (-1)^j A_0 f(t) \exp(in\theta) \left(\frac{r}{R(t)}\right)^{n(-1)^{j-1}} \left(\frac{Q}{2n\pi R(t)} + \frac{R}{n}\frac{f'(t)}{f(t)}\right). \tag{2.18}$$

As mentioned above, surface tension is assumed to be spatially uniform and $u_\theta = 0$. Thus, the only boundary condition is in the normal direction. The normal stress balance for the perturbed state can be obtained using Eq. (2.10) by substituting $r = R(t) + a(t,\theta)$ and retaining only terms to $O(a)$:

$$\begin{aligned}
&\left[p_{01} + 2\eta_1 \frac{\partial^2 \phi_{01}}{\partial r^2} - \left(p_{02} + 2\eta_2 \frac{\partial^2 \phi_{02}}{\partial r^2}\right)\right]\Bigg|_{r=R} \\
&\qquad + a\frac{\partial}{\partial r}\left[p_{01} + 2\eta_1 \frac{\partial^2 \phi_{01}}{\partial r^2} - \left(p_{02} + 2\eta_2 \frac{\partial^2 \phi_{02}}{\partial r^2}\right)\right]\Bigg|_{r=R} \\
&\qquad + \left[p_{11} + 2\eta_1 \frac{\partial^2 \phi_{11}}{\partial r^2} - \left(p_{12} + 2\eta_2 \frac{\partial^2 \phi_{12}}{\partial r^2}\right)\right]\Bigg|_{r=R} \\
&\qquad = \gamma\left(\frac{2}{b} + \frac{1}{R(t)} - \frac{a}{R(t)^2} - \frac{1}{R(t)^2}\frac{\partial^2 a}{\partial \theta^2}\right) \\
&- \left[(\kappa_s - \eta_s)\left(\frac{1}{R} - \frac{a}{R(t)^2} - \frac{1}{R(t)^2}\frac{\partial^2 a}{\partial \theta^2}\right) + 2\eta_s\left(\frac{1}{R}\left(1 - \frac{a}{R}\right)\right)\right]\left[\frac{1}{R(t)}\left(1 - \frac{a}{R(t)}\right)\right]\left[\left(\frac{\partial \phi_{01}}{\partial r}\right)\Big|_{r=R}\right. \\
&\qquad + a\frac{\partial}{\partial r}\left(\frac{\partial \phi_{01}}{\partial r}\right)\Big|_{r=R} \\
&\qquad \left. + \left(\frac{\partial \phi_{11}}{\partial r}\right)\Big|_{r=R}\right].
\end{aligned} \tag{2.19}$$

The LHS of Eq. (2.19) is the difference of normal stresses across the fluid interface, whereas the RHS is the Laplace pressure and surface viscous stresses. To obtain the dispersion relation between

the growth rate and the wavenumber, n, we subtract contributions from the base state normal stress balance [Eq. (2.14)] from Eq. (2.19):

$$a\frac{\partial}{\partial r}\left[p_{01}+2\eta_1\frac{\partial^2\phi_{01}}{\partial r^2}-\left(p_{02}+2\eta_2\frac{\partial^2\phi_{02}}{\partial r^2}\right)\right]\Bigg|_{r=R}$$
$$+\left[p_{11}+2\eta_1\frac{\partial^2\phi_{11}}{\partial r^2}-\left(p_{12}+2\eta_2\frac{\partial^2\phi_{12}}{\partial r^2}\right)\right]\Bigg|_{r=R}+\gamma\left(\frac{a}{R(t)^2}+\frac{1}{R(t)^2}\frac{\partial^2 a}{\partial\theta^2}\right)$$
$$=-\frac{(\kappa_s+\eta_s)}{R(t)^2}\left[a\frac{\partial}{\partial r}\left(\frac{\partial\phi_{01}}{\partial r}\right)\Big|_{r=R}+\left(\frac{\partial\phi_{11}}{\partial r}\right)\Big|_{r=R}\right]$$
$$-\left[(\kappa_s+\eta_s)\left(-\frac{2a}{R(t)^3}\right)+(\kappa_s-\eta_s)\frac{n^2a}{R(t)^3}\right]*$$
$$\left[\left(\frac{\partial\phi_{01}}{\partial r}\right)\Big|_{r=R}+a\frac{\partial}{\partial r}\left(\frac{\partial\phi_{01}}{\partial r}\right)\Big|_{r=R}+\left(\frac{\partial\phi_{11}}{\partial r}\right)\Big|_{r=R}\right]. \tag{2.20}$$

Substituting $p_j=\phi_j/M_j$, $\eta_j=b^2/(12M_j)$, expressing ϕ_j in terms of the base state and perturbed state with Eq. (13) and Eq. (2.18) respectively, and substituting $a(t,\theta)=A_0f(t)\exp(in\theta)$, Eq. (2.20) becomes (Appendix A.3)

$$-\gamma\frac{n^2-1}{R(t)^2}+Q\{\frac{(n-1)M_1-M_2(n+1)}{2M_1M_2n\pi R(t)}-\frac{b^2[M_1(n-1)+M_2(n+1)]}{12M_1M_2\pi R(t)^3}$$
$$-\frac{n^2(\kappa_s-\eta_s)-2(\kappa_s+\eta_s)}{2\pi R(t)^4}\}$$
$$=\left[\frac{(M_1+M_2)R(t)}{M_1M_2n}+\frac{b^2[M_1(n+1)+M_2(n-1)]}{6M_1M_2R(t)}+\frac{\kappa_s+\eta_s}{R(t)^2}\right]\frac{f'(t)}{f(t)}\ . \tag{2.21}$$

In linear stability theory, $f(t)$ is proportional to $\exp(\sigma t)$, where σ is the growth rate and is equal to $f'(t)/f(t)$. Note that $\sigma(R(t))$ is time-dependent through its implicit relation to the changing radius $R(t)$. As n is an integer and $n>1$, the RHS of Eq. (2.21) is positive and can be treated as a scaled growth rate of perturbations. The terms on the LHS each represents contributions from surface tension, driving pressure, viscous normal stresses, and surface viscous stresses respectively.

in the radial direction. The negative signs in front of the terms reveal the stabilizing effects of surface tension and viscous normal stresses. While dilatational viscosity (κ_s) has a stabilizing effect, Eq. (2.21) reveals a surprising destabilizing effect of surface shear viscosity (η_s) in the radial direction. As the intrinsic dilatational viscosity seems to be usually more dominant [75–77], we here assume $\kappa_s \gg \eta_s$.

We nondimensionalize Eq. (2.21) using characteristic values of $T = 2b^2\pi/Q$ for time and the gap width, b, for length to give

$$-\frac{n^2-1}{\xi^2}P - \frac{m(n+1)-(n-1)}{n\xi} - \frac{m(n+1)+(n-1)}{6\xi^3} - \frac{n^2-2}{12\xi^4}\frac{\kappa_s}{\mu_2 b} = \left[\frac{(1+m)\xi}{n} + \frac{m(n-1)+(n+1)}{6\xi} + \frac{1}{12\xi^2}\frac{\kappa_s}{\eta_2 b}\right]\alpha, \tag{2.22}$$

where

$$\xi = \frac{R(t)}{b}, \tag{2.23}$$

$$m = \frac{M_2}{M_1} = \frac{\eta_1}{\eta_2}, \tag{2.24}$$

$$\alpha = T\sigma = \frac{2b^2\pi}{Q}\sigma, \tag{2.25}$$

$$Ca = \frac{\dot{R}\eta_2}{\gamma} = \frac{1}{12P\xi}, \qquad P = \frac{\pi b\gamma}{6Q\eta_2}. \tag{2.26}$$

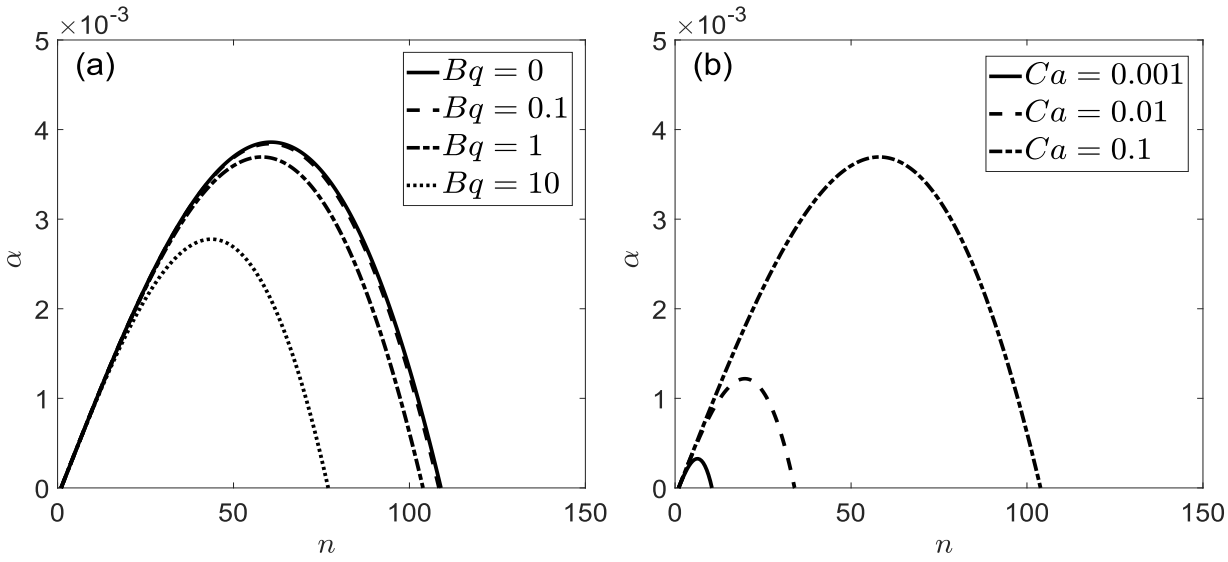

Figure 2.2. (a) Dimensionless growth rate α as a function of wavenumber n at $Ca = 0.1, \xi = 100$. Both the maximum growth rate α_{max} and the corresponding wavenumber n_{max} decrease with increasing Boussinesq number Bq, indicating that surface viscosity stabilizes perturbations. (b) Dimensionless growth rate α as a function of wavenumber n at $Bq = 1, \xi = 100$. This reveals the classically known effect of surface tension in suppressing the instability upon decreasing the Capillary number Ca.

The choice of the dimensionless quantity P is motivated by being able to describe the system in terms of externally controllable quantities and is adapted from past experiments in viscous fingering [38]. A Boussinesq number naturally emerges in Eq. (2.22) and depends on the Hele-Shaw cell gap width, b, as

$$Bq_b = \frac{\kappa_s}{\eta_2 b}. \tag{2.27}$$

Bq_b captures the relative strength of surface viscous stresses to bulk (outer fluid) viscous stress. As previously discussed, both shear and dilatational contributions appear together in an azimuthally stretching deformation. The effect of surface rheology decreases when Bq_b becomes

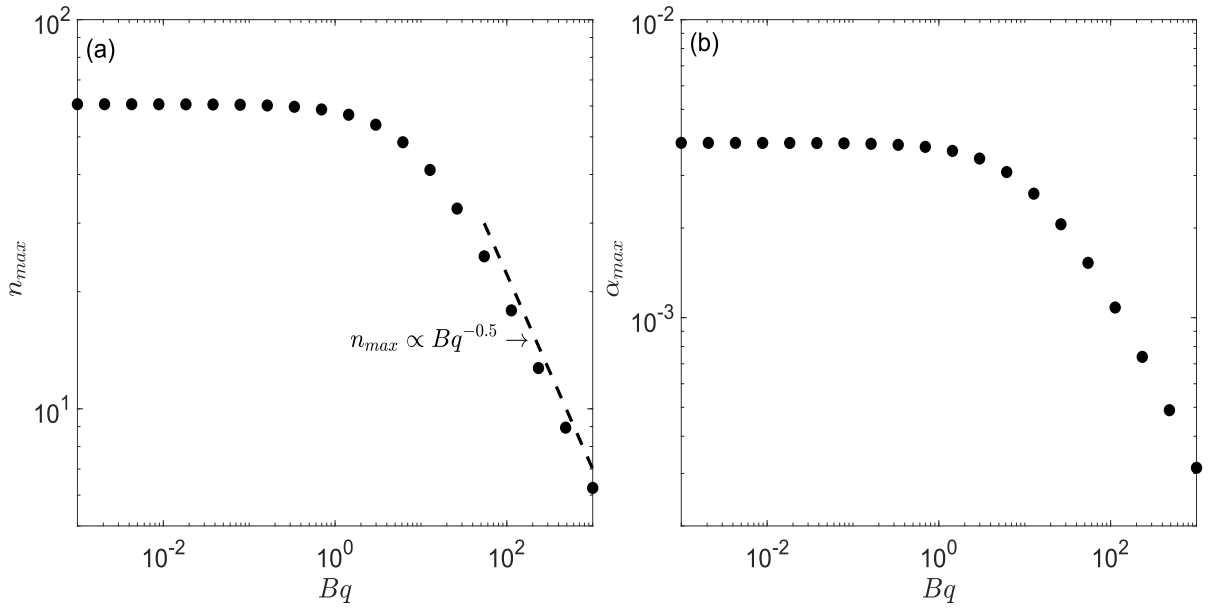

Figure 2.3. (a) The most unstable wavenumber n_{max} as a function of Boussinesq number Bq at $Ca = 0.1$ and $\xi = 100$. n_{max} asymptotes to a constant value as $Bq \to 0$ (corresponding to the effect of surface tension alone) and decreases as a power law for $Bq \gtrsim 1$. The dashed line with a slope of -0.5 is shown as a guide. (b) Maximum growth rate α_{max} follows a similar trend, shown here for a constant $Ca = 0.1$.

small. In the limits of $Bq_b \to 0$, Eq. (2.22) retrieves the classic result of Kim et al. [38]. Inverting Eq. (2.22) for the dimensionless growth rate α gives

$$\alpha = -\frac{\left(6P\xi + \frac{Bq_b}{2\xi}\right)n^3 + (m+1)n^2 - \left[6\xi(P+\xi) - m(6\xi^2+1) + 1 + \frac{Bq_b}{\xi}\right]n + 6(m+1)\xi^2}{\xi^2\left(6(m+1)\xi^2 + (m+1)n^2 - (m-1)n + \frac{n}{2}\frac{Bq_b}{\xi}\right)}. \tag{2.28}$$

Alternatively, we can use the instantaneous base state radius, $R(t)$, as a characteristic length scale, upon which the ratio of surface to bulk viscous stresses is characterized by a modified Boussinesq number:

$$Bq = \frac{Bq_b}{\xi} = \frac{\kappa_s}{\eta_2 R(t)}. \tag{2.29}$$

The new length scale $R(t)$ is appropriate as $R(t)^2$ characterizes the area over which bulk viscous stresses dissipate when the inner fluid expands radially.

Often, the invading inner fluid is significantly less viscous than the outer fluid, as is the case in oil recovery with pressurized air. In this case, $M_1 \gg M_2$ ($\eta_1 \ll \eta_2$) and $m = M_2/M_1 \approx 0$. Eq. (2.28) then simplifies to

$$\alpha = -\frac{\left(6P\xi + \frac{1}{2}Bq\right)n^3 + n^2 - [6\xi P + 6\xi^2 + 1 + Bq]n + 6\xi^2}{\xi^2\left(6\xi^2 + n^2 + n + \frac{n}{2}Bq\right)}. \tag{2.30}$$

This is the final form of the dispersion relation $\alpha(n)$. In what follows, we discuss the significance of the surface viscous terms in Eq. (2.30) and their effects on controlling the instability.

2.4. Effect of surface rheology

Figure 2.2 shows the dispersion relation with either Ca or Bq held constant. The key observation is that surface viscous stresses act to suppress the instability at constant surface tension. The maximum growth rate and the window of unstable wavenumbers decrease as surface viscous stresses become dominant relative to bulk viscous stress (Fig. 2.2a). The change is most prominent at large wavenumbers, suggesting that surface viscosity disproportionately resists deformations associated with thinner fingers. This result is consistent with the kinematic interpretation that thinner fingers with a higher local curvature stretch the interface more than wider fingers of the same amplitude, and are thus met with a stronger surface viscous resistance to deformation.

Figure 2.2b illustrates the well-known effect of surface tension on the Saffman-Taylor instability. The growth rates and the range of unstable wavenumbers decrease with increasing surface tension (or decreasing Capillary number, Ca) at constant Bq. The stabilizing effect of surface tension

alone in this geometry, as given by Eq.(2.30) in the limit of $Bq \to 0$, is consistent with the results of Logvinov [78].

We can quantify the effect of surface rheology on the most unstable finger by analytically tracking the maxima of the dispersion relation. To determine the mode n_{max} that corresponds to the maximum growth rate α_{max}, we assume n is continuous and set the derivative of Eq. (2.30) to zero:

$$\frac{\partial \alpha}{\partial n} = 0 = \left(3P\xi + \frac{1}{4}Bq\right)n_{max}^4 + \left(6P\xi + \frac{1}{2}Bq\right)\left(1 + \frac{1}{2}Bq\right)n_{max}^3 + \left[18\xi^2\left(3P\xi + \frac{1}{4}Bq\right) + 3\xi P + (3\xi^2 + 1) + \frac{3}{4}Bq\right]n_{max}^2 - 6\xi^2\left[3\xi^2 + 1 + 3P\xi + \frac{3}{4}Bq\right]. \quad (2.31)$$

We numerically invert Eq. (2.31) to obtain $n_{max}(Bq)$, which is plotted in Fig. 2.3. The most unstable wavenumber, n_{max}, is mostly constant for $Bq \lesssim 1$. As the system shifts to the interface-dominated regime ($Bq \gtrsim 1$), n_{max} decreases as a power-law model shown in Fig. 3a, decaying as $n_{max} \propto 1/\sqrt{Bq}$ for realistic values of n_{max}. We note that the power-law changes as $Bq \to \infty$: however, this limit is unrealistic as wavenumbers are discrete and required to be greater than 1. We can further use the maximum wavenumber in our dispersion relation Eq. (2.30) to obtain the maximum linear growth rate α_{max} of the finger (Fig. 2.3b), which follows the trend of n_{max} and begins to decrease as a power law as Bq increases within a realistic range.

We can estimate the most unstable finger width predicted by our linear analysis as follows. The fastest-growing wavenumber, n_{max}, corresponding to the maxima of the dispersion relation results in a wavelength $\lambda = 2\pi R(t)/n_{max}$. Assuming the interface has the same number of peaks and troughs, the most likely observable finger width is then $\lambda/2 = \pi R(t)/n_{max}$. The proportionality

between the finger width and $R(t)$ suggests a strategy to adjust the selection of observable viscous fingers at the interface in an experiment. From Fig. 2.2a, we see that the most unstable wavenumber decreases with increasing Bq, suggesting again that thinner fingers are less likely when surface viscous effects are dominant. In addition, the effect is amplified at larger Bq. Surface viscous effects thus add to the various other external factors that can control the formation of viscous fingers. For example, recent studies have shown that a gradual variation of the geometry of the flow passage and porous media can retard viscous fingering [39,40]. Elastic boundaries also offer a novel method to delay the onset of instabilities and suppress viscous fingering [41]. Alternatively, opposing the hydraulic flow with secondary electro-osmotic flows induced by an external electric field can also effectively control the formations of viscous fingers [42]. Our work shows that surface rheology is an additional and yet unexplored factor that controls the size and stability of viscous fingers.

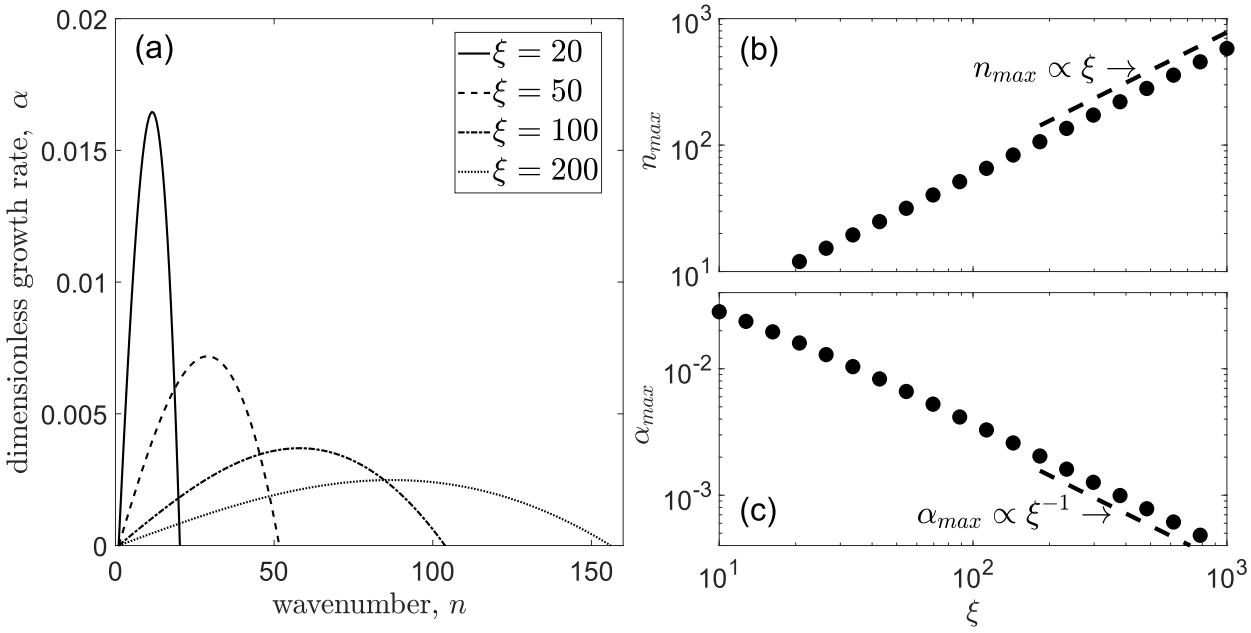

Figure 2.4. (a) Dimensionless growth rate α as a function of wavenumber n at $Ca = 0.1, Bq = 1$, and various values of normalized radius ξ. (b-c) The maximum growth rate α_{max} decreases and the corresponding wavenumber n_{max} increases with increasing ξ, indicating more fingers if perturbed at a larger radius. The dashed lines with slopes of 1 and -1 are shown as guides.

Importantly, note that the radial injection flow is time-dependent and the growth rate $\sigma(R(t))$ depends implicitly on time via the normalized radius $\xi(t) = R(t)/b$. Examining the nonlinear long-time behavior will require analyzing the cascade of higher-order modes and tip-splitting [38] or integrating perturbations over time to extract the wavenumber that exhibits the maximum total growth over time [79–81]. Here, instead, we illustrate the early-time growth at different radii should the system be stable until it reaches that radius (e.g., via slower injection rates). Figure 2.4 illustrates the dimensionless growth rate α as a function of wavenumber n at $Ca = 0.1$ and $Bq = 1$ when perturbations grow at different normalized radii ξ. The most unstable wavenumber, n_{max}, increases linearly with increasing ξ as shown in Fig. 2.4b. The corresponding maximum linear growth rate α_{max} decreases as a power law $\alpha_{max} \propto 1/\xi$. Consequently, we expect more fingers to emerge at a larger radius although finger widths remain independent of R (as $\lambda \sim R(t)/n_{max}$ and

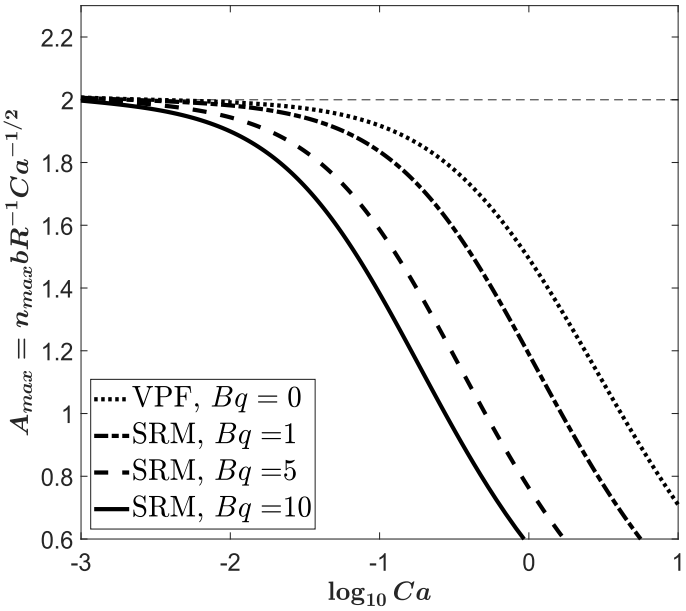

Figure 2.5. The surface rheology model (SRM) developed here predicts lower values of the modified wavenumber A_{max} at larger Ca when compared with the viscous potential flow (VPF) model [38]. A_{max} departs further from past predictions with increasing Bq, especially at large Ca. The dashed horizontal line represents the expected value of A_{max} in the classic Saffman-Taylor problem which neglects viscous normal stresses and surface viscous stresses.

$n_{max} \propto \xi \propto R$). Fingers that emerge at a larger radius also grow at a slower pace as compared to those perturbed at a smaller radius, consistent with past work on optimal fluid injection rate to suppress instability [82].

Finally, we compare our predictions for the impact of surface viscosity relative to classic theories of viscous fingering. A commonly used normalization of the most unstable wavenumber, $A_{max} = bn_{max}/(R\sqrt{Ca})$, is motivated by the value of n_{max} expected in the classic Saffman-Taylor problem: neglecting viscous normal stresses and surface viscous stresses in the radial Hele-Shaw geometry gives (Appendix A.3) [37,71] :

$$n_{max} = \frac{1}{\sqrt{3}}\left[12Ca\frac{R(t)^2}{b^2} + 1\right]^{\frac{1}{2}}. \tag{2.32}$$

Consequently, A_{max} should be constant – indeed, approximately 2 when $R \gg b$ – in the absence of viscous normal stresses and surface viscous stresses. Viscous normal stresses lower the most unstable wavenumber at large Ca, as shown by the viscous potential flow (VPF) model [38]. To incorporate the effect of surface rheology, we rearrange Eq. (2.31) for the Capillary number in terms of n_{max}, ξ, and Bq to get

$$Ca = -\frac{n_{max}^4 + 2\left[1 + \frac{1}{2}Bq\right]n_{max}^3 + (18\xi^2 + 1)n_{max}^2 - 6\xi^2}{4(n_{max}^2 - 6\xi^2)\left[(3\xi^2 + 1) + \frac{3}{4}Bq\right] + n_{max}^2 Bq\{(n_{max} + 1)^2 + (18\xi^2 - 1) + n_{max}Bq\}}. \tag{2.33}$$

Figure 2.5 shows the results of the theoretical predictions of A_{max} from the VPF model and our surface rheological model (SRM) obtained using Eq. (2.33) with ξ=100. SRM retrieves the VPF model in the limit of $Bq = 0$. As Bq increases, SRM deviates from VPF and predicts lower values of A_{max} especially when Ca is large. Even marginal interfacial rheology, with $\kappa_s = O(1)\ mN \cdot s/m$ so that $Bq = O(1)$, seems to modify past models significantly, as shown in Fig. 2.5. In fact, the surface dilatational viscosity κ_s of many common classes of surfactants that are used in industry and engineering can be as high as $O(100)\ mN \cdot s/m$ [28,83]. Thus, we predict that the presence of surfactants with non-trivial surface rheology would quantitatively change the rate of growth of unstable fingers.

2.5. Conclusion

We have examined, for the first time, the role of interfacial rheology in radial viscous fingering. The interface becomes more stable with increasing surface viscosity. Perturbations with smaller

wavelengths are preferentially suppressed, leading us to expect stabler and wider fingers. The wavenumber n_{max} that corresponds to the maximum growth rate α_{max} approximates to $n_{max} \propto 1/\sqrt{Bq}$ for $Bq \gtrsim 1$ within a realistic range. This suppression of the instability is in addition to the classically known effect of surface tension and normal viscous stresses. We theoretically predict that the surfactants with non-trivial surface rheology decrease the most unstable wavenumber when compared to the classic viscous potential flow (VPF) model developed by Kim et al. [38], especially in regions of large Ca. We hope this work helps motivate careful and controlled future experiments and models involving complex surfactant-laden interfaces.

We have neglected surface wetting effects and interfacial surface tension gradients for simplicity. However, surface wetting effects may improve the theoretical predictions as shown in systems without added surfactants [84,85]. First-order surface wetting effects could be incorporated by adding an extra term, $-2\gamma J Ca^{2/3}/b$, to the right-hand side of Eq. (2.10) [34,35,37]. J can be obtained numerically [34], and the resulting relation between Ca, Bq, and n_{max} could then be obtained following the steps in this study. Accounting for tangential flow and changes in surface tension might further improve the accuracy of the model. This would require simultaneously solving an azimuthal stress balance for the Marangoni stress along with the normal stress balance shown in our analysis. Finite-time transport of soluble molecules on and off the interface can also lead to a viscous-like dissipation at the interface [2]. Such an apparent dilatational viscosity, $\kappa_{s,app}$, that emerges even in the absence of an intrinsic surface viscosity but instead due to adsorption/desorption, can alter the instability in qualitatively similar ways to what we have described. We leave these as future problems.

Chapter 3 Impact of soluble surfactants on liquid jets

3.1. Preface

The chapter is the reprint of the paper" impact of soluble surfactants on liquid jets", which is currently under review for the Journal of Chemical Physics. In this chapter we aim to focus on the rheological impact of soluble surfactants on the surface instabilities in liquid jets. Interfaces are common in both nature and industry, arising in foams, respiratory droplets, coatings, and inkjet printing. Generally, surfactants are used to stabilize the interface against rupture and coalescence. However, interfacial instabilities can still occur even in the presence of surfactants. As surfaces deform, surfactants alter the surface flows by causing gradients in surface tension and inducing additional surface rheological effects. Quantitatively characterizing these effects has been a key research interest in the past decades. This work focuses on the effect of soluble surfactants on the instabilities in liquid jets. Recent studies have shown that insoluble surfactants delay thread thinning and suppress instabilities in Newtonian jet fluids. However, the understanding of soluble surfactants in jet fluid stability is still lacking, specifically the adsorption and desorption kinetics of the soluble surfactants near the interface. In this work, we use linear stability analysis to quantitatively show the stabilizing effects of increasing Marangoni stresses, surfactant adsorption and desorption time, and surface viscous stresses of soluble surfactants in jet fluid. In addition, we identify the surface viscous-like force contributed by the Marangoni flow with a finite adsorption and desorption time interval. Our work suggests that surface rheology should be considered as a potential factor in future models and experiments involving complex surfactant-laden interfaces.

3.2. Introduction

Surface active agents or surfactants are widely used in a variety of applications, including coating flows [86,87], spreading films [88,89], foams and emulsions [90–92], and inkjet printing [57,93].

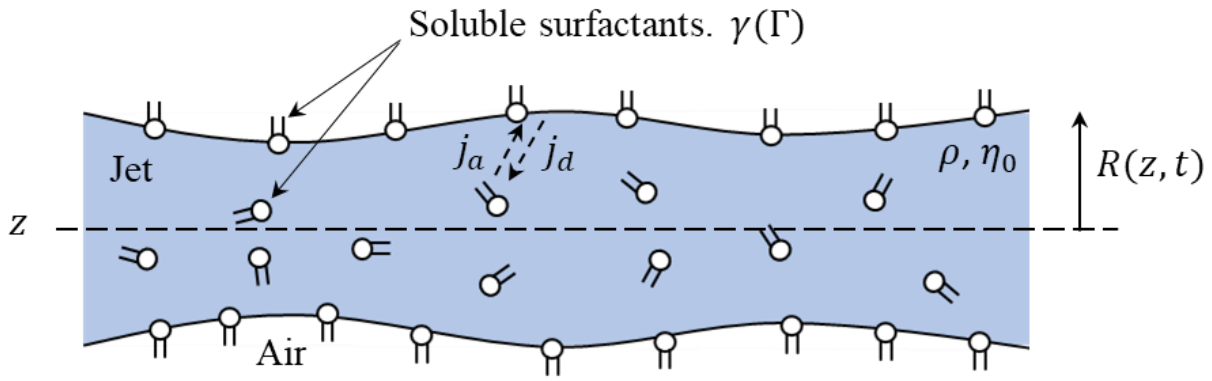

Figure 3.1, Schematic of a Newtonian liquid jet with a monolayer of soluble surfactants. The bulk phase has the density ρ and viscosity η_0. The soluble surfactants exchange between the bulk phase and the air-liquid interface at an adsorption rate j_a and a desorption rate j_d. The surfactants also give the surface a surface tension γ which depends on the surface concentration Γ.

The presence of surfactants confers rheological properties to the interface, altering the dynamics of surface flows [5–8].

Surface deformations lead to surfactant concentration gradients in the plane of the fluid interface, which give rise to Marangoni stresses directing interfacial flow from regions of low to high surface tension. Additionally, surfactant-laden interfaces may display an intrinsic surface rheological response that affects surface flows and deformations [5–7]. Like in 3D fluids, a surface shear viscosity η_s characterizes resistance to 2D shear deformations in the plane of the interfaces. This is measured using geometries involving shearing alone, such as translating needles [94], magnetic rods, [19], and rotating micro-buttons [6,26]. On the other hand, a surface dilatational viscosity κ_s characterize 2D resistance to uniform dilatation or compression of the surface, and is measured using methods involving oscillatory droplets and bubbles [7,28,95]. As both the Marangoni stresses and surface rheological stresses play controlling roles in the dynamics of surface deformation, separately identifying and measuring these stresses becomes critical in interfacial engineering.

Separating these surface stresses might is not always straightforward. For instance, reverse Marangoni flows set up by insoluble surfactants constrains tangential flow around a translating disk or particle to be 2D incompressible [2,96]. This changes the associated 3D bulk flow and modifies the total viscous resistance to particle motion. Experiments set up to measure the surface rheology of insoluble surfactants, if not carefully controlled to only involve interfacial shear, could therefore cause potential misinterpretations of the results [16,17]. On the other hand, surfaces with soluble surfactants can restore the surface concentration gradients through the exchange of surfactants between the surfaces and the bulk. The rate of the exchange affects the strength of the Marangoni flows, which may again lead to partial immobilization of the interface. As a result, Marangoni flows with a finite adsorption and desorption time likely leads to an "apparent" surface viscosity, which further complicates the task of properly demarcating various effects [2,3,9,18,24,25].

We wish to demonstrate, for the first time, this interplay of surface stresses in the context of the stability of a thin viscous jet. While the impact of surfactants on jet fluid stability has long been studied [49–51], very few previous works acknowledge the effects of surface rheology [52,53], and even these are limited to studying insoluble surfactants. It has been well established that insoluble surfactants lowers the thinning rate of liquid jets [52,56,62,63] and modifies the formation of satellite beads [53–61]. Numerical studies also revealed that increasing surface viscous stresses would greatly delay thread thinning, deform the primary droplets, and suppress the growth of secondary droplets [97,98]. In addition, analytical solutions modeling the thread thinning also highlighted the importance of surface viscosities in the thinning process in both the limit of dominant surface diffusion, where the thread thins exponentially, and the limit of dominant surface convection, where the thread thins following a power-law [64,65]. However, insights on

liquid jets with soluble surfactants remains limited, with no analytical efforts to date. Experimentally, soluble surfactants in liquid jets are found to increase the jet-breaking lengths [66,67] in addition to playing a role in the formations and the sizes of the satellite beads [53,58,61,68]. A fundamental quantitative understanding of soluble surfactants in jet fluid stability is still lacking, specifically addressing adsorption and desorption kinetics and the role of the apparent surface viscosity mentioned above.

In this work, we investigate the impact of soluble surfactants on a Newtonian liquid jet. We isolate and quantitatively show the effects of the Marangoni stresses, the net flux of surfactant adsorption and desorption, and the surface viscous stresses via linear stability analysis. In addition, we identify the surface viscous-like force contributed by the Marangoni flow with a finite adsorption and desorption time. Lastly, we show numerically that we can generalize the results from the linear stability analysis to more realistic sorption kinetics governed by Langmuir and Frumkin models [69,70].

3.3. Problem description

3.3.1. Governing equations

We model a thin liquid column as a slender axisymmetric jet of Newtonian fluid containing surfactants. This jet is initially cylindrical but is allowed to axisymmetrically deform via the interplay of surface tension and fluid flow. The radius $R(z,t)$ is assumed to vary slowly along the length of the jet [Fig. 3.1], allowing us to retain only the leading terms in an expansion in the radius [52,99]. In this leading-order description, mass and momentum conservation take the form [52,100,101]:

$$\frac{\partial R}{\partial t} + u\frac{\partial R}{\partial z} + \frac{R}{2}\frac{\partial u}{\partial z} = 0, \tag{3.1}$$

$$\rho\left(\frac{\partial u}{\partial t} + u\frac{\partial u}{\partial z}\right) = -\frac{\partial(\kappa\gamma)}{\partial z} + \frac{2}{R}\frac{\partial \gamma}{\partial z} + \frac{3\eta_0}{R^2}\frac{\partial}{\partial z}\left(R^2\frac{\partial u}{\partial z}\right) + \frac{9}{2R^2}\frac{\partial}{\partial z}\left(\eta_s R\frac{\partial u}{\partial z}\right) + \frac{1}{2R^2}\frac{\partial}{\partial z}\left(\eta_d R\frac{\partial u}{\partial z}\right), \tag{3.2}$$

where $u(z,t)$ is the axial velocity, ρ is the bulk fluid density, γ is the surface tension, κ is the interfacial curvature, η_0 is the bulk fluid viscosity, η_s is the surface shear viscosity, and η_d is the surface dilatational viscosity. The left-hand side of Eq. (3.2) captures fluid inertia, whereas the first three terms on the right-hand side (RHS) correspond to familiar pressure and viscous contributions in the Navier-Stokes equation. Pressure relates to the dynamic surface tension via the Young-Laplace relation, with the interfacial curvature written as

$$\kappa = \frac{1}{R(1+R_z^2)^{1/2}} - \frac{R_{zz}}{(1+R_z^2)^{3/2}}, \tag{3.3}$$

where R_z and R_{zz} represents the partial derivatives $\partial R/\partial z$ and $\partial^2 R/\partial z^2$, respectively. As the jet profile and surfactant concentration evolve, gradients in both curvature κ and surface tension γ contribute to the pressure gradient via the first two terms in the RHS of Eq. (3.2). These terms are thus the curvature pressure and the Marangoni stress, respectively.

The last two terms in Eq. (3.2) arise from surface rheology and, barring a few exceptions, have not been accounted for in past studies. They arise from treating the interface between the jet and surrounding fluid as a 2D viscous manifold following the Boussinesq-Scriven framework [1,11,52] and then expanding in small radius. Notably, in this slender jet limit, shear and dilatational viscosities are indistinguishable from each other: this is also the case in other one-dimensional

surface deformations such as in dip coating [87] and in the interfaces of Plateau borders within foams [102].

In addition to the mass and momentum conservation equations, we take the leading order of the convection-diffusion equation for the surfactant surface concentration, Γ, and obtain the 1-D surfactant transport equation as

$$\frac{\partial \Gamma}{\partial t} + u\frac{\partial \Gamma}{\partial z} + \frac{\Gamma}{2}\frac{\partial u}{\partial z} = D_s \frac{\partial^2 \Gamma}{\partial z^2} + j_n, \tag{3.4}$$

where D_s is the surfactant diffusivity, $j_n = j_a - j_d$ accounts for the net exchange of surfactant molecules between the bulk and the interface between the kinetic fluxes of adsorption, j_a, and desorption, j_d. Here, we assume Frumkin kinetics [15] and express the net flux as

$$j_n = j_a - j_d = k_a C_0(\Gamma_\infty - \Gamma) - k_d \Gamma \, exp\left(-\frac{\beta \Gamma}{k_B T}\right), \tag{3.5}$$

where k_a and k_d are the adsorption and desorption rate constants, C_0 is the bulk surfactant concentration, k_B is Boltzmann's constant, T is the absolute temperature, and Γ_∞ is the surface concentration at maximum packing [3,70,103]. β represents intermolecular interactions, which are attractive when $\beta > 0$ and repulsive when $\beta < 0$. When $\beta = 0$, we recover the simpler Langmuir model.

Additionally, we assume that the fluid is surfactant-rich and that there are no diffusion limitations to transport within the bulk fluid: in other words, we take C_0 to be a constant. Substituting j_n in Eq. (3.4) gives

$$\frac{\partial \Gamma}{\partial t} + u\frac{\partial \Gamma}{\partial z} + \frac{\Gamma}{2}\frac{\partial u}{\partial z} = D_s \frac{\partial^2 \Gamma}{\partial z^2} + \frac{\Gamma_\infty - \Gamma}{t_a} - \frac{\Gamma}{t_d} exp\left(-\frac{\beta \Gamma}{k_B T}\right), \tag{3.6}$$

where $t_a = 1/k_a C_0$ and $t_d = 1/k_d$ are characteristic adsorption and desorption times.

To close the system of equations, we specify the relation between the dynamic surface γ and the local surfactant concentration Γ via the associated Frumkin isotherm [3,70]:

$$\gamma = \gamma_0 + k_B T \Gamma_\infty ln\left(1 - \frac{\Gamma}{\Gamma_\infty}\right) + \frac{\beta \Gamma^2}{2}, \tag{3.7}$$

where γ_0 is the surface tension of a 'clean' interface (i.e., when $\Gamma = 0$).

3.3.2. Non-dimensionalization

We non-dimensionalize continuity [Eq. (3.1)], momentum conservation [Eq. (3.2)], and surfactant transport [Eq. (3.6)] equations using characteristic values of initial radius R_0 for length, the unperturbed surface tension γ_0 for forces (per unit length), and the undisturbed initial value Γ_0 for surface concentration. A natural time scale $t_R = \sqrt{\rho R_0^3/\gamma_0}$ emerges from the balance of inertial ($\sim \rho R_0/t_R^2$) and capillary ($\sim \gamma_0/R_0^2$) forces: this is indeed the Rayleigh time scale [104] associated with the breakup of an inviscid fluid thread (or, equivalently, a characteristic velocity $v = R_0/t_R$). We can then rewrite Eq (3.1), (3.2), and (3.6) in their dimensionless forms as

$$\frac{\partial \tilde{R}}{\partial \tilde{t}} + \frac{\tilde{R}}{2}\frac{\partial \tilde{u}}{\partial \tilde{z}} + \tilde{u}\frac{\partial \tilde{R}}{\partial \tilde{z}} = 0, \tag{3.8}$$

$$\frac{\partial \tilde{u}}{\partial \tilde{t}} + \tilde{u}\frac{\partial \tilde{u}}{\partial \tilde{z}} = -\frac{\partial(\tilde{\gamma}\tilde{\kappa})}{\partial \tilde{z}} + \frac{2}{\tilde{R}}\frac{\partial \tilde{\gamma}}{\partial \tilde{z}} + \frac{3Oh}{\tilde{R}^2}\frac{\partial}{\partial \tilde{z}}\left(\tilde{R}^2\frac{\partial \tilde{u}}{\partial \tilde{z}}\right) + \frac{Oh}{2\tilde{R}^2}\frac{\partial}{\partial \tilde{z}}\left(Bq_d\tilde{R}\frac{\partial \tilde{u}}{\partial \tilde{z}}\right) + \frac{9Oh}{2\tilde{R}^2}\frac{\partial}{\partial \tilde{z}}\left(Bq_s\tilde{R}\frac{\partial \tilde{u}}{\partial \tilde{z}}\right), \tag{3.9}$$

$$\frac{\partial \tilde{\Gamma}}{\partial \tilde{t}} + \tilde{u}\frac{\partial \tilde{\Gamma}}{\partial \tilde{z}} + \frac{\tilde{\Gamma}}{2}\frac{\partial \tilde{u}}{\partial \tilde{z}} = \frac{1}{Pe}\frac{\partial^2 \tilde{\Gamma}}{\partial \tilde{z}^2} + \frac{\tilde{\Gamma}_\infty - \tilde{\Gamma}}{\tau_a} - \frac{\tilde{\Gamma}}{\tau_d}exp\left(-\frac{\tilde{\beta}\tilde{\Gamma}}{\tilde{E}_0}\right), \tag{3.10}$$

where tildes represent dimensionless variables, τ_a and τ_d are the dimensionless characteristic adsorption and desorption times, $\widetilde{\beta}$ represents the dimensionless β and is expressed as

$$\tilde{\beta} = \frac{\beta \Gamma_0^2}{\gamma_0}, \tag{3.11}$$

and $\widetilde{E}_0$ is defined as

$$\widetilde{E}_0 = \frac{k_B T \Gamma_0}{\gamma_0}, \tag{3.12}$$

which will be discussed in more details in Sec 3.3.3 below.

Three dimensionless numbers also emerge in the equations: the Ohnesorge number,

$$Oh = \frac{\eta_0}{\sqrt{\rho R_0 \gamma_0}}, \tag{3.13}$$

represents the ratio of viscous to inertial forces for a capillary velocity γ_0/η_0, and is an indicator of the relative importance of fluid viscosity in the problem. $Oh \to 0$ in the classic inviscid analysis of the Rayliegh-Plateau instability. Alternatively, Oh may be interpreted the ratio of the viscous capillary relaxation time $(\eta_0 R_0/\gamma_0)$ to the Rayleigh time t_R.

The second dimensionless group is the Peclet number

$$Pe = \frac{v R_0}{D_s}, \tag{3.14}$$

which captures the relative strength of convection to diffusion of surfactant molecules on the fluid interface. And finally, the Boussinesq number

$$Bq_s = \frac{\eta_s}{\eta_0 R_0}, \tag{3.15}$$

represents the relative strength of surface shear viscous stress to bulk viscous stress. The surface shear viscosity, η_s, can be replaced by the surface dilatational viscosity, κ_s, to characterize the surface resistance to dilatation and gives a Boussinesq number associated with dilation Bq_d.

In what follows, we first examine the linear stability of a Newtonian liquid jet with soluble surfactants. Our objective is to (a) analyze the relative roles and interplay of surface stresses and surfactant transport on and off the interface, and (b) to identify different surfactant processes that play identical roles in determining jet stability, and so might be otherwise indistinguishable or misinterpreted in an experiment.

3.3.3. Linear stability analysis

We introduce perturbations about the base state R_0 via normal modes that are periodic in z and grow or decay in time:

$$\tilde{R}(\tilde{z},\tilde{t}) = 1 + \varepsilon e^{\sigma\tilde{t}+ik\tilde{z}}. \tag{3.16}$$

Here, $\varepsilon \ll 1$ is the dimensionless amplitude of the perturbation, σ is the dimensionless growth rate, and k is the dimensionless wavenumber. Similarly, we can express the perturbed axial velocity and surface concentration in their dimensionless forms:

$$\tilde{u}(\tilde{z},\tilde{t}) = \delta\tilde{u}e^{\sigma\tilde{t}+ik\tilde{z}}, \tag{3.17}$$

$$\tilde{\Gamma}(\tilde{z},\tilde{t}) = 1 + \delta\tilde{\Gamma}e^{\sigma\tilde{t}+ik\tilde{z}}, \tag{3.18}$$

where $\delta\tilde{u}$ and $\delta\tilde{\Gamma}$ are the corresponding dimensionless perturbed amplitudes, respectively.

The linearized Frumkin isotherm becomes

$$\tilde{\gamma} = 1 - \tilde{E}_0\tilde{\Gamma} + \frac{\tilde{\beta}\tilde{\Gamma}^2}{2}, \tag{3.19}$$

where

$$\tilde{E}_0 = \frac{\Gamma}{\gamma_0}\frac{d\Pi_{\text{ideal}}}{d\Gamma}\bigg|_{\Gamma_0} = \frac{k_B T\Gamma_0}{\gamma_0} \tag{3.20}$$

can be written as the dimensionless Marangoni modulus in the ideal gas limit, Γ_0 is the initial surface concentration, and $\Pi = \gamma - \gamma_0$ is the surface pressure.

We can solve for $\delta\tilde{u}$ by substituting Eq. (3.16) and Eq. (3.17) into Eq. (3.8) to obtain

$$\delta\tilde{u} = \frac{2i\sigma\varepsilon}{k}. \tag{3.21}$$

Following this, we obtain $\delta\Gamma$ by substituting Eq. (3.17), (3.18) into Eq. (3.10) and subtracting the base state (See Appendix B.1):

$$\delta\tilde{\Gamma} = \frac{\sigma\varepsilon}{\sigma + k^2/Pe + 1/\tau_a \ + (1 - \tilde{\beta}/\tilde{E}_0)\exp(-\tilde{\beta}/\tilde{E}_0)/\tau_d}, \tag{3.22}$$

Finally, we extract the dispersion relation between growth rates and wavenumbers by substituting Eq. (3.16) – Eq. (3.19) into Eq. (3.9) to get (See Appendix B.2)

$$2\sigma = \left(1 - \tilde{E}_0 + \frac{\tilde{\beta}}{2}\right)\frac{k^2 - k^4}{\sigma} + \frac{(\tilde{\beta} - \tilde{E}_0)k^2}{\sigma + \frac{k^2}{Pe} + \frac{1}{\tau_a} + \frac{\left(1 - \frac{\tilde{\beta}}{\tilde{E}_0}\right)\exp\left(-\frac{\tilde{\beta}}{\tilde{E}_0}\right)}{\tau_d}} - (6 + Bq_d + 9Bq_s)Ohk^2 \tag{3.23}$$

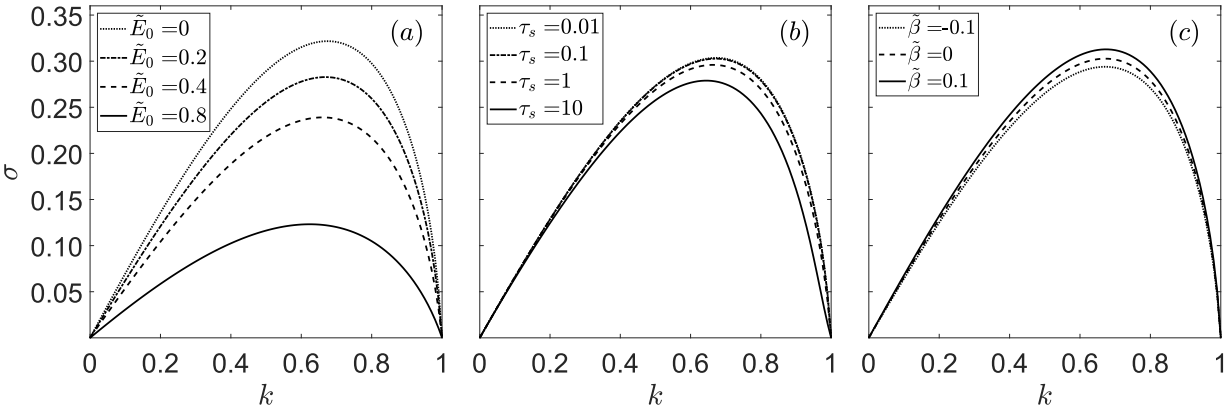

Figure 3.2, Dispersion relations between the dimensionless growth rate, σ, and the dimensionless wavenumber, k, at $Pe = 1000$, $Bq_s = 0$. (a) The Marangoni modulus, $\tilde{E}_0$, varies with $\tau_s = 0.1$, $Oh = 0.04$, $Bq_d = 1$ and $\tilde{\beta} = 0$. An increasing $\tilde{E}_0$, which means a stronger Marangoni response, suppresses the growth rate. (b) The characteristic kinetic flux time, τ_s, varies with $\tilde{E}_0 = 0.1$, $Oh = 0.04$, $Bq_d = 1$ and $\tilde{\beta} = 0$. An increasing τ_s, which indicates longer adsorption/desorption time and a stronger Marangoni response, suppresses the instability. (c) Intermolecular repulsions ($\tilde{\beta} < 0$) facilitate more stabilized systems than intermolecular attractions ($\tilde{\beta} > 0$) at with $\tilde{E}_0 = 0.1$, $\tau_s = 0.1$ $Oh = 0.04$, and $Bq_d = 1$.

Here, we assume Bq_s and Bq_d are constant and do not depend on the surface concentration, Γ (although this is straightforward to generalize; see, for example, Ref. [52,64,65,97]). Note that in the ideal gas limit, $0 \leq \tilde{E}_0 < 1$. Investigating The regime of $\tilde{E}_0 \geq 1$ requires a different approach and is beyond the scope of the current work [97,105]. Setting $\tilde{E}_0 = 0$, $Bq_s = 0$, and $Bq_d = 0$ reduces Eq. (3.23) to the dispersion relation describing the evolution of a surfactant-free, viscous thread [106]. Bulk fluid viscosity, represented via the Ohnesorge number, always acts to dampen the growth of the instability. Further setting $Oh = 0$ reduces Eq. (3.23) recovers the classic inviscid Rayleigh-Taylor instability dispersion. When surfactants are present, stability is governed by the interplay of the Marangoni modulus $\tilde{E}_0$, the characteristic timescale for adsorption and desorption τ_s, the intermolecular interaction parameter $\tilde{\beta}$, the Boussinesq number associated with surface dilation Bq_d, the Boussinesq number associated with surface shear Bq_s, the Ohnesorge

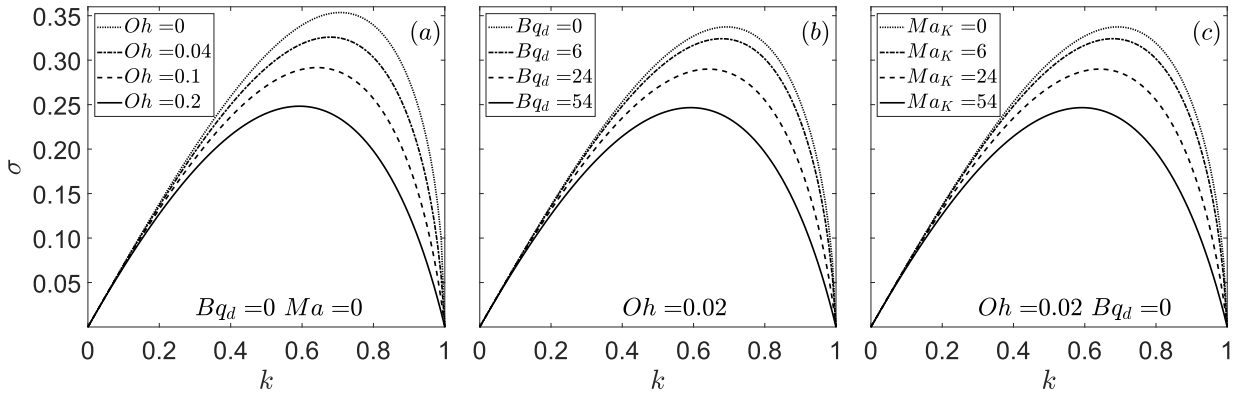

Figure 3.3, Dispersion relations between the dimensionless growth rate, σ, and the dimensionless wavenumber, k. Liquid jets with (a) clean interface, (b) insoluble surfactants with $\tilde{E}_0 = 0.01$, and (c) soluble surfactants with $\tilde{E}_0 = 0.01$ at different values of Oh, Bq_d, Ma_K give similar dispersion relations.

number Oh, and the Peclet number Pe. In what follows, we show and discuss the significance of each parameter on controlling the instability.

3.4. Results and discussion

3.4.1. Surface stabilization due to 'apparent' surface viscosities

We can evaluate the impact of changing each controlling variable while holding the other parameters constant. As Bq_d and Bq_s have the same mathematical forms, we look at the effect of surface viscous stresses by only varying the magnitude of Bq_d and set $Bq_s = 0$. In the case of $\tilde{\beta} = 0$, we define a net characteristic timescale for an adsorption-desorption controlled flux as

$$\frac{1}{\tau_s} = \frac{1}{\tau_a} + \frac{1}{\tau_d}. \tag{3.24}$$

Fig. 3.2 shows the dispersion relations with different values of the dimensionless Marangoni modulus $\tilde{E}_0$, the net kinetic flux of adsorption and desorption τ_s, and the factor associated with intermolecular interaction $\tilde{\beta}$. As $\tilde{E}_0$ increases, we observe a decrease in both the dimensionless

maximum growth rate, σ_{max}, and the corresponding dimensionless wavenumber, k_{max}. The observation is consistent with the expectation that a larger $\tilde{E}_0$ indicates a larger change in the surface pressure in response to a change in the surface concentration, leading to larger Marangoni stresses. Stronger Marangoni stresses more strongly resist surface deformations and lead to a smaller growth rate. Such an effect of a stronger Marangoni response has been previously explored in the case of insoluble surfactants [52,97,105]. Previously unexplored dynamics emerge when the surfactant is soluble, as depicted in Fig. 3.2(b). A larger τ_s indicated a longer time scale for surfactants to exchange between the interface and the bulk, leading to a slower relaxation of surface concentration gradients. As a result, the Marangoni response is relatively stronger and acts to suppress the instability like in the insoluble case. Faster adsorption/desorption 'remobilizes' the interface [25,107], suppressing surface concentration gradients and weakening Marangoni flow, leading to a more unstable interface as τ_s decreases. Surface diffusion plays a qualitatively similar role, acting to quench surface concentration gradients and weaken the Marangoni effect with decreasing Pe.

Intermolecular interactions between adsorbed surfactants also result in macroscopic effects that seem indistinguishable without more careful analysis. Jets are stabilized as intermolecular interactions change from attraction ($\tilde{\beta} > 0$) to repulsion ($\tilde{\beta} < 0$). This can be qualitatively explained by two potential mechanisms. This can be qualitatively explained by two potential mechanisms. First, as the intermolecular interactions are repulsive or $\tilde{\beta} < 0$, it decreases the surface tension and stabilize the surface [Eq. (3.19)]. Second, the repulsive intermolecular interactions could slow down the recovery of the surface concentration gradient by hindering the adsorption of the surfactants in the bulk, resulting in a longer duration of the Marangoni flow. On the contrary, when $\tilde{\beta} > 0$ and the surfactants attract each other, the surface tension would increase

and lead to surface destabilization. In addition, the attractive intermolecular interactions would facilitate the recovery of the surface concentration gradient as the surfactants in the bulk adsorbs to the surface. Indeed, as summarized by Kralchevsky et al. and Manikantan et al. [2,70], surface pressure with a positive $\tilde{\beta}$ experiences a smaller change in response to a change in surface concentration, leading to weaker Marangoni stresses. We have also analyzed the effect of surface diffusion and observed a relatively small decrease in the growth rates as we increased Pe (See Appendix B3). The results suggest that the change in Pe, at least in the linear stability analysis, does not play a significant role.

A key finding of our analysis is that finite-time adsorption/desorption has an effect that is qualitatively similar and quantitatively indistinguishable from a surface viscosity. Such an 'apparent surface rheology' has been reported in systems such as dip coating, translation of bubble, oscillation of drops, and foams [2,3,9,18,24,25]. To see this effect, we consider our dispersion relation Eq. (3.23) in the limit of negligible surface diffusion and fast adsorption in Langmuir kinetics ($\tilde{\beta} = 0$), where $Pe \to \infty$ and $\tau_s \leq 0.1$, we can simplify the terms in Eq. (3.23) as $k^2/Pe \to 0$ and $\sigma \ll 1/\tau_s$. Then, the simplified dispersion equation becomes

$$2\sigma = \left(1 - \tilde{E}_0\right)\frac{-k^4 + k^2}{\sigma} - (6 + Bq_d + 9Bq_s + Ma_K)Ohk^2, \tag{3.25}$$

where

$$Ma_K = \frac{E_0 t_s}{\eta_0 R_0} \tag{3.26}$$

is a modified Marangoni number that represents the relaxation of surface concentration gradients due to Marangoni convection versus due to adsorption/desorption [2,9]. E_0 is the dimensional

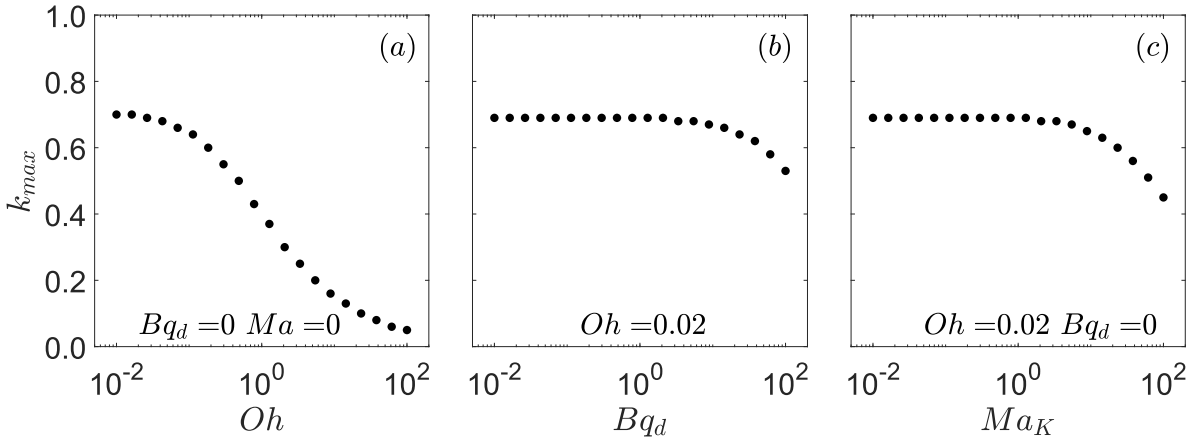

Figure 3.4, The most dominant wavenumber, k_{max}, of the liquid jets with (a) a clean interface, (b) insoluble surfactants with $\tilde{E}_0 = 0.01$, and (c) soluble surfactants with $\tilde{E}_0 = 0.01$ at different values of Oh, Bq_d, and Ma_K.

Marangoni modulus and t_s is the dimensional characteristic time of the net adsorption and desorption kinetic fluxes.

A larger Ma_K implies that the interface has stronger resistance to deformation and behaves as 2-D incompressible. As highlighted in Eq. (3.25), Ma_K is a viscous-like term and behaves as an "apparent" surface viscosity as it has the same mathematical form as Bq_s and Bq_d. As a result, it is likely to mischaracterize the surface viscous contributions during experiments where soluble surfactants are present in the system [6,16–18]. Fig.3.3 highlights this effect: liquid jets with clean interfaces, insoluble surfactants, or soluble surfactants may display indistinguishable growth spectra due to bulk viscous dissipation, surface viscous dissipation, or Marangoni-induced apparent surface dissipation. At least in the initial stages of growth of perturbations, therefore, surfactant-free viscous jets evolve in. a manner indistinguishable from jets dominated by contributions from either intrinsic or apparent surface viscosities. Conversely, Eq. (3.25) highlights the complex interplay and indistinguishability of surface transport processes of completely different origin: it may therefore be difficult or even impossible to tease out individual effects

without complementary experiments where one physical effect is separated without triggering the other.

We can track the fastest-growing wavenumber, k_{max}, corresponding to the maximum growth rate, σ_{max}, and estimate the perturbation wavelength $\lambda = 2\pi R(t)/k_{max}$. We show the change in k_{max} in different systems with various Oh, Bq_d, and Ma_K in Fig.3.4. As the liquid jets with clean interfaces are perturbed, the most dominant wavenumber decreases as Oh increases. In the systems with insoluble and soluble surfactants, k_{max} stays approximately constant and then decreases as the values of Bq_d and Ma_K increase. The results suggest that mainly the initial fluid properties in Oh such as ρ, η_0, R_0, and γ_0 define the perturbation wavelength of the liquid jet. As the jet thins, the changes in Bq_d and Ma_K do not significantly affect the wavelength of the perturbed jet. In the next section, we show that the stabilizing effect of $\tilde{E}_0$, τ_s, and Bq_d demonstrated in the linear stability analysis can be generalized to the systems using Langmuir and Frumkin isotherms via numerical simulation.

3.4.2. Numerical simulations

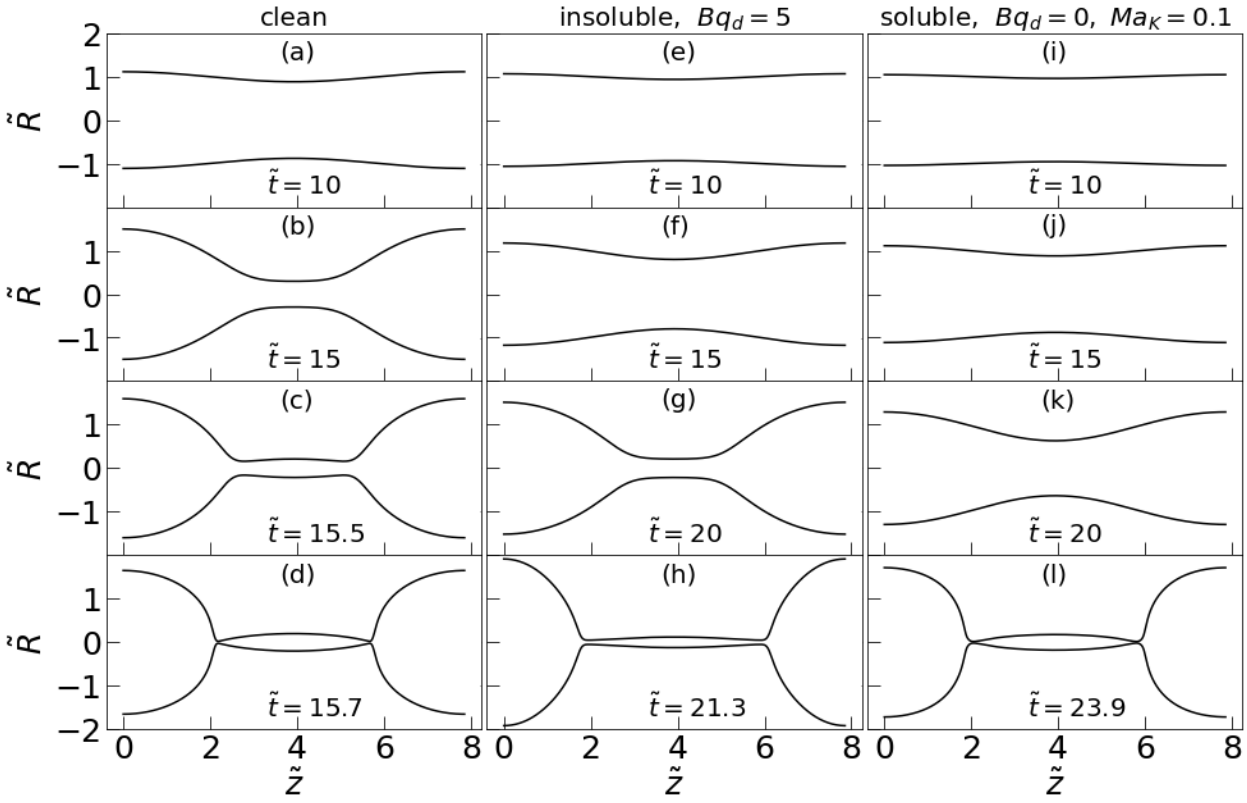

Figure 3.5, Newtonian liquid jets with (a)-(d) clean interface, (e)-(h) insoluble surfactants at $\tilde{E}_0 = 0.1$, and (i)-(l) soluble surfactants at $\tilde{E}_0 = 0.1$ and $\tau_s = 0.01$ at different times with $Oh = 0.04$, $Bq_s = 0$, $Pe = 1000$ using the Langmuir ($\tilde{\beta} = 0$) isotherm and kinetics. Systems with surfactants show increased stability.

We solve Eq. (3.13) - (3.15) using an explicit finite difference method with five hundred grid points. The initial dimensionless timestep is set to 10^{-5} and is changed to 10^{-7} after $\tilde{t} = 15$. We perturb the dimensionless radius as $\tilde{R}(z,t) = 1 + 0.01\cos(k\tilde{z})$, where the dimensionless wavenumber $k = 0.8$. Other parameters used in the numerical simulations are as follows: $Oh = 0.04$, $Bq_s = 0$, and $Pe = 1000$. We use both the Langmuir model and the Frumkin model to describe the isotherms and adsorption/desorption kinetics in the simulations at $\tilde{\Gamma}_\infty = 10$.

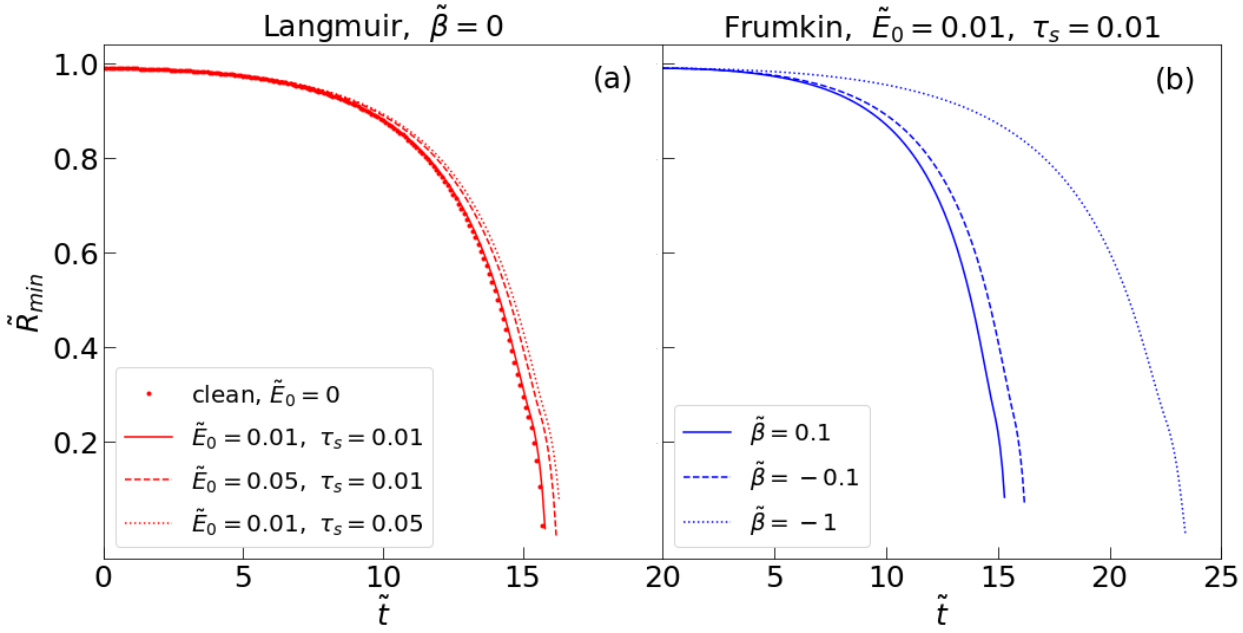

Figure 3.6, Newtonian liquid jets with $Oh = 0.04$, $Bq_s = 0$, $Bq_d = 0$, $Pe = 1000$ with a clean interface and at various $\tilde{E}_0$, τ_s, and $\tilde{\beta}$ in time for Langmuir isotherm (left) and Frumkin isotherm. Increasing $\tilde{E}_0$or τ_s or decreasing $\tilde{\beta}$ stabilizes the jet as indicated by the minimum radius $\tilde{R}_{min}$.

3.4.2.1 Newtonian jets with clean interface, insoluble surfactants, and soluble surfactants

We first show the simulation results of the Newtonian liquid jets with clean interface, insoluble surfactants, and soluble surfactants using the Langmuir model in Fig. 3.5. Fig. 3.5 (a)-(d) illustrate the development of a Newtonian liquid jet with a clean interface before breaking. As we add insoluble surfactants to the system and apply surface viscous stresses as shown in Fig. 3.5 (e)-(h), we can observe a more stabilized system comparing to the results of a clean interface at $\tilde{t} = 15$. The stabilizing effect of the surface rheological stresses is consistent with what we have observed in linear stability analysis [Sec. 3.4.1]. In addition, we observe the continuous thinning of the liquid jet without any formations of the satellite beads throughout the simulation at $k = 0.8$. Thus,

increasing the surface viscous stresses serves as a potential solution to avoid the undesirable formations of satellite droplets in certain applications such as inkjet printing [108,109]. In the case of soluble surfactants shown in Fig.3.5 (i)-(l), we again observe the stabilizing effect of the viscous-like surface stresses due to the Marangoni flows with a finite adsorption and desorption time interval at $\tilde{t} = 15$, highlighting its similarity to the intrinsic surface viscous stresses.

3.4.2.2 Effects of various parameters in jet fluid stability

We vary the dimensionless Marangoni modulus, $\tilde{E}_0$, the dimensionless characteristic net kinetic timescale, τ_s, and the dimensionless intermolecular interaction factor, $\tilde{\beta}$, to analyze the effect of each parameter in the numerical models using the Langmuir and Frumkin isotherms and kinetics [69,70]. While the linear stability results apply only to the early time when the instabilities are small, we show the entire results in $\tilde{t}$ to highlight the differences and use the radius at the midpoint of the liquid jet $\tilde{R}_{mid}$ to demonstrate the development of the instabilities in Fig. 3.6. We vary the values of $\tilde{E}_0$ and τ_s in the Langmuir model and only vary $\tilde{\beta}$ in the Frumkin model to demonstrate the effect of each parameter. Note that the Langmuir model can be retrieved from the Frumkin model by setting $\tilde{\beta} = 0$.

As we increase the values of $\tilde{E}_0$ and τ_s as shown in Fig.3.6 (a), we observe a slower development of the jet thinning, indicating their stabilizing effects. The results are consistent with the results of linear stability analysis [Sec. 3.4.1], which show that both higher $\tilde{E}_0$ and τ_s values indicate relatively stronger Marangoni responses and lead to the suppression of instabilities. As we decrease the value of $\tilde{\beta}$ in Fig.3.6 (b), which indicates stronger repulsive intermolecular interactions, we observe a slower development of jet thinning that is consistent with the linear stability results. While the results shown here correspond to the dimensionless wavenumber $k =$

0.8, we observe similar results at $k = 0.2$. We also hold the bulk concentration constant as we are only interested in the linear regime. Accurately simulating and analyzing the jet thinning dynamics in the long term requires another mass conservation equation on the bulk concentration, which becomes more significant as the liquid jet develops into a thread.

3.5. Conclusion

We have examined the role of soluble surfactants in Newtonian liquid jets. The interface becomes more stable as the Marangoni modulus, the characteristic net adsorption and desorption time, and the surface viscosities increase. We have identified that the Marangoni flow with a finite adsorption and desorption time produces a surface viscous-like force, which acts as an "apparent" surface viscosity as the associated Marangoni number has the same mathematical form as the Boussinesq number. The similarity between the intrinsic surface viscosities and "apparent" surface viscosities draws attention to the significance of clearly differentiating the surface viscous contributions in systems with soluble surfactants. We have also drawn similar conclusions from numerical simulations using Langmuir and Frumkin models. We have observed that surface viscous stresses have the potential to prevent the formation of satellite beads. In addition, the repulsive intermolecular interactions between surfactants can be an alternative factor to suppress the instabilities in liquid jets.

While we have focused on the role of soluble surfactants in a simple system with Newtonian fluid, we can reach similar conclusions with the systems using viscoelastic liquid jets. Following the Oldroyd-B model [101,110] and performing linear stability analysis, we can add the following term to the RHS of Eq. (3.23) to capture the stresses associated with viscoelasticity

$$-\frac{6(1-\mathrm{B})Oh}{\sigma De+1}k^2, \tag{3.27}$$

where B is the ratio of the viscosity from the solvent contribution to the total viscosity and $De = \tau_r/t_R$ is the Deborah number which is the ratio of relaxation time τ_r, to the Rayleigh timescale t_R. The added stresses do not affect the stabilizing effect of $\tilde{E}_0$, τ_s, and Bq_d. As the satellite beads form more easily with viscoelastic liquid jets, we again observe the suppressions of the formation of satellite beads when Bq_d becomes large enough (See Appendix B.4).

Chapter 4 Remaining work

4.1. Preamble

The chapter contains an ensemble of unpublished theoretical analysis and experimental data obtained during my doctoral research. Some of the theoretical analysis will help future graduate students in the group to understand the topic better. In addition, the experimental results and some of the challenges documented here provide some references and ideas for future experimental designs of similar projects.

4.2. Bubble oscillation

Only a handful of studies have evaluated the individual role of surface shear viscosity (η_s) and surface dilatational viscosity (κ_s) respectively in surface deformation. Stoodt and Slattery conducted experiments using a capillary rise technique and found that κ_s was two orders of magnitude greater than η_s upon displacement of residual oil [77]. Buzza et al. predicted a similar dominance of the intrinsic surface dilatational viscosity in a theoretical analysis on incompressible foams [76]. In this study, we aim to provide the theoretical work that illustrates both surface shear viscosity (η_s) and surface dilatational viscosity (κ_s) contribute to 1D deformation. In addition, we will investigate the role of each surface viscosity during the oscillation of a 2D single bubble and present this technique as potentially an alternative way to obtain the value of surface dilatational viscosity (κ_s) when the value of surface shear viscosity (η_s) is known. We hypothesize that while both η_s and κ_s contribute to the 1D oscillatory deformation, the magnitude of κ_s could be much larger than η_s in certain surface concentrations, leading to the neglection of η_s.

4.2.1. Theory

The Boussinesq-Scriven model in cylindrical coordinates reveals both surface shear and surface dilatational viscosities contribute to 1D deformations. We use this work to provide the experimental data to verify and confirm the hypothesis that the role of surface dilatational viscosity is much larger than the corresponding surface shear viscosity in the deformation of a 2D single bubble. We perturb the bubble radius, velocity, pressure, and surface concentration as follows,

$$R(t) = R_0 + \delta R e^{i\omega t}, \tag{4.1}$$

$$u_r(r,t) = \delta u_r e^{i\omega t}, \tag{4.2}$$

$$P(r,t) = P_0 + \delta P e^{i\omega t}, \tag{4.3}$$

$$\Gamma(t) = \Gamma_0 + \delta\Gamma e^{i\omega t}, \tag{4.4}$$

where R_0, P_0, and Γ_0 are the initial radius, pressure, and surface concentration, respectively, δR, δu_r, δP, and $\delta\Gamma$ are the corresponding perturbed amplitude, and ω is the oscillatory frequency. To find the expressions of δu_r & δP, we solve the continuity and stokes equations listed below:

$$\nabla \cdot u = 0, \tag{4.5}$$

$$\rho \frac{\partial u}{\partial t} = -\nabla \mathrm{P} + \mu \nabla^2 u, \tag{4.6}$$

where ρ is the fluid density. Solving these equations using the perturbed variables to obtain

$$\delta u_r(r) = \frac{i\omega R_0}{r} \delta R, \tag{4.7}$$

$$\delta P(r) = \rho \omega^2 R_0 \ln\left(\frac{r}{L}\right) \delta R, \tag{4.8}$$

where L is the length where the perturbation decays to 0, i.e., $\delta P(L) = 0$.

We can solve for the expression of $\delta\Gamma$ via the surfactant transport equation at the surface:

$$\frac{\partial \Gamma}{\partial t} + \nabla_s \cdot (\Gamma u_s) + \Gamma(\nabla_s \cdot n)(u \cdot n) = D_s \nabla_s^2 \Gamma + j_n, \tag{4.9}$$

where $\boldsymbol{u_s}$ is the surface flow velocity, $\boldsymbol{n}$ is the normal vector, D_s is the surfactant diffusivity, and j_n accounts for the surfactant flux between the surface and the bulk. Simplifying the surfactant transport equation above to the current geometry where there is no surface flow or flow gradient due to uniform dilation, we obtain

$$\frac{\partial \Gamma}{\partial t} + \Gamma\left(\frac{1}{R}\right)(u_r) = j_n. \tag{4.10}$$

When surfactants are insoluble, we set $j_n = 0$. Solving Eq. (4.10) using the perturbed $u_r(r,t)$ and $\Gamma(t)$ to obtain the expression of $\delta\Gamma$ for insoluble surfactants as

$$\delta\Gamma_{\text{insol}} = -\frac{\delta R \Gamma_0}{R_0}. \tag{4.11}$$

To obtain the values of the surface viscosities, we need the normal stress balance from the Boussinesq-Scriven model in cylindrical coordinates, which is written as

$$(p_1 - p_2) - 2\eta_1 \frac{\partial u_r}{\partial r}|_{r=R} + 2\eta_2 \frac{\partial u_r}{\partial r}|_{r=R} = \gamma\left(\frac{2}{b} + \frac{1}{r}\right)|_{r=R} + \left(\frac{\kappa_s + \eta_s}{r^2}\right) u_r|_{r=R}, \tag{4.12}$$

where the surface tension is expressed as

$$\gamma = \gamma(\Gamma_0) + \frac{\partial \gamma}{\partial \Gamma}|_{\Gamma_0} \delta\Gamma e^{i\omega t} = \gamma_0 - \frac{E_0}{\Gamma_0} \delta\Gamma e^{i\omega t}. \tag{4.13}$$

Applying oscillatory perturbations to Eq. (4.12) to obtain the dynamic stress balance with insoluble surfactants at the interface:

$$\frac{\delta P_1(R) - \delta P_2(R)}{\delta R}\frac{R_0}{\gamma_0/R_0} = -1 + R_0\left(\frac{2}{b} + \frac{1}{R_0}\right)\frac{E_0}{\gamma_0} - 2i\frac{(\eta_1 - \eta_2)\omega R_0}{\gamma_0} + i\frac{\omega(\kappa_s + \eta_s)}{\gamma_0}, \quad (4.14)$$

where δP_1 is the induced amplitude of the pressure, δR is the amplitude of the measured radius response, R_0 is the initial radius of the interface at equilibrium, γ_0 is the equilibrium surface tension, b is the gap width of the Hele-Shaw cell, $E_0 = \Gamma\frac{\partial \Pi}{\partial \Gamma}\Big|_{\Gamma_0}$ is the Marangoni modulus with Γ being the surface concentration and Π being the surface pressure, ω is the oscillation frequency, η_1 and η_2 are the inner and outer fluid viscosity respectively, η_s is the surface shear viscosity, and κ_s is the surface dilatational viscosity. We can obtain the left-hand-side of Eq. (4.14) by measuring the experimental oscillatory pressure change and the response of the interfacial radius. $\delta P_2(R)$ can be obtained by solving Eq. (4.8) and is written as

$$\delta P_2(R_0) = \rho\omega^2 R_0 \ln\left(\frac{R_0}{L}\right)\delta R. \quad (4.15)$$

We can then synchronize the two measurements to match the data which represents the out-of-phase response to the theoretical values shown on the right-hand-side of Eq. (4.14) to determine $\kappa_s + \eta_s$.

We can also express Eq. (4.14) in dimensionless terms as shown below

$$\delta\tilde{P}_1 - \delta\tilde{P}_2(R) = \left[-1 + R_0\left(\frac{2}{b} + \frac{1}{R_0}\right)Ma * Ca + i(-2 + Bq_\kappa)Ca\right]\delta\tilde{R}, \quad (4.16)$$

where the capillary number is written as

$$Ca = \frac{(\eta_1 - \eta_2)\omega R_0}{\gamma_0}, \quad (4.17)$$

the Marangoni number is

$$Ma = \frac{E_0}{(\eta_1 - \eta_2)R_0\omega}, \tag{4.18}$$

and the Boussinesq number is

$$Bq_\kappa = \frac{(\kappa_s + \eta_s)}{(\eta_1 - \eta_2)R_0}. \tag{4.19}$$

We compare the values of $\kappa_s + \eta_s$ obtained from the experimental data with the independently measured values of κ_s and η_s from the literature to determine the contributions of each viscosity. We also explore a range of different surface concentrations to confirm the hypothesis that while both viscosities contribute to 1D deformations, κ_s can have a much larger contribution compared to the corresponding η_s at certain surface concentrations.

4.2.2. Experimental setup

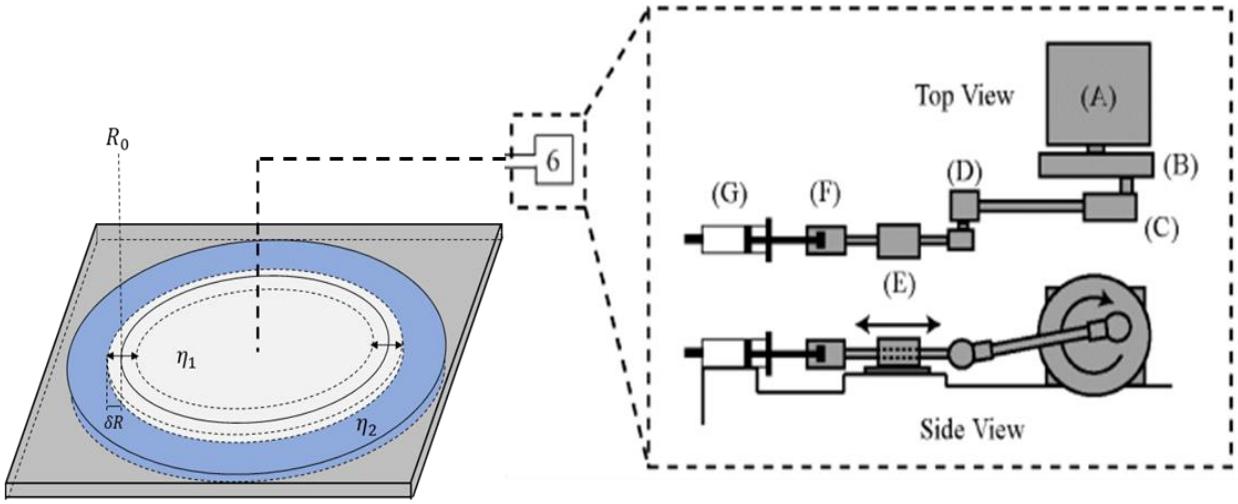

Figure 4.1. Schematic of the Hele-Shaw cell connected to an oscillatory motor [111]: (A) DC motor, (B) rotating wheel attached to motor axel, (C) ball joint rod, (D) universal joint, (E) pillow block, (F) syringe holder, and (G) syringe. The bubble oscillates from an initial radius R_0 with a variation of δR.

The schematic diagram of the oscillatory motor is similar to the design by Alvarez et al. [111] as shown in Fig. 4.1. We connect the oscillatory pump to a Hele-Shaw cell via a tube and use a pressure transducer to measure the induced pressure. A camera will be placed above the Hele-Shaw cell to capture the interfacial movements. We will individually timestamp the measurement of pressure and radius for synchronization in post-processing to determine the out-of-phase contributions. Fig. 4.2 shows the experimental setup of the oscillatory motor we used in the experiment. We connected a 5 ml syringe at the end of the oscillatory motor so that the plunger would move with the motor rod. The syringe barrel will be fixed during the experiment so that the oscillatory motion of the plunger would provide the oscillatory pressure of the inner phase. The air was delivered through a rubber tube connected with the syringe via a Luer Lock syringe tip. We used a control switch to determine the angular speed of the wheel and, thus, the oscillatory speed.

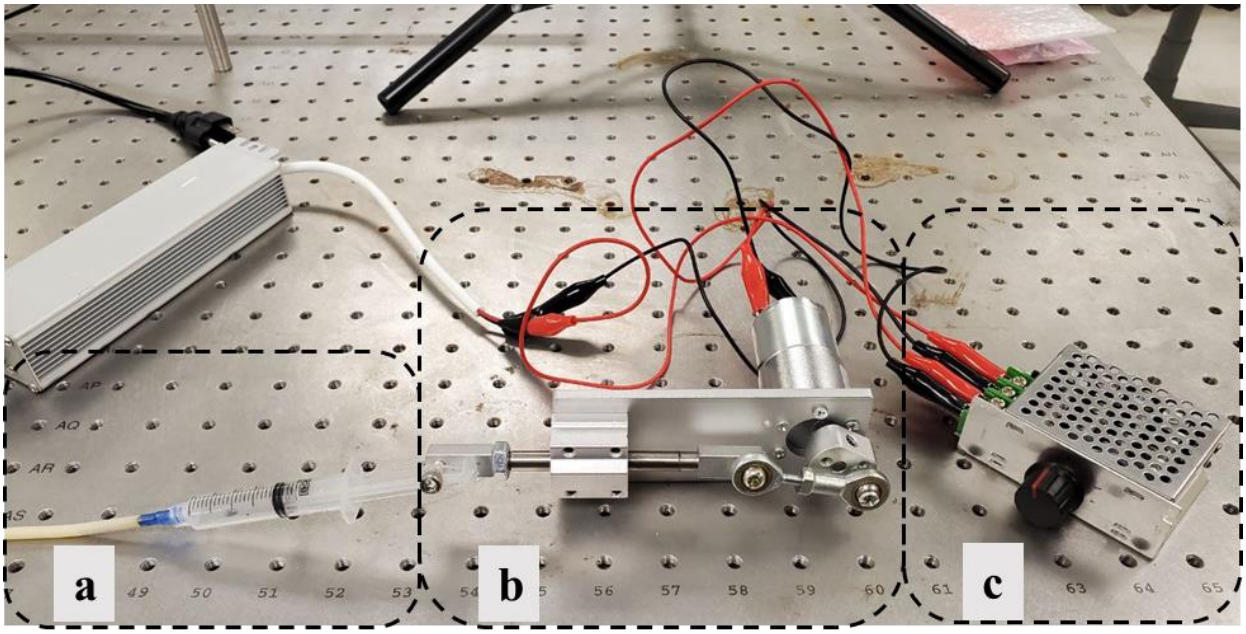

Figure 4.2. Experimental setup of the oscillatory motor connected with a 5 ml syringe. a) shows the syringe connected with the rubber tube via a Luer Lock tip to provide oscillatory pressure for the inner phase. b) shows the oscillatory motor connected with the power supply and the control switch. c) shows the control switch used to determine the oscillatory speed of the motor.

We used Dipalmitoyl phosphatidylcholine (DPPC, 500mg Powder, Avanti Polar Lipids, Inc, CAS 63-89-8), an insoluble surfactant common in lung alveoli, and Arachidyle alcohol (AA, 5g, Powder, Sigma-Aldrich, CAS 629-96-9), another insoluble surfactant common in cosmetics, for the experiment. We chose DPPC as it has been relatively well studied with both values of η_s and κ_s available in the literature [28,112]. We chose AA as it can form a Newtonian monolayer when the surface pressure Π is above 15 mN/m [74]. While the value of η_s of AA is available in literature, κ_S is not.

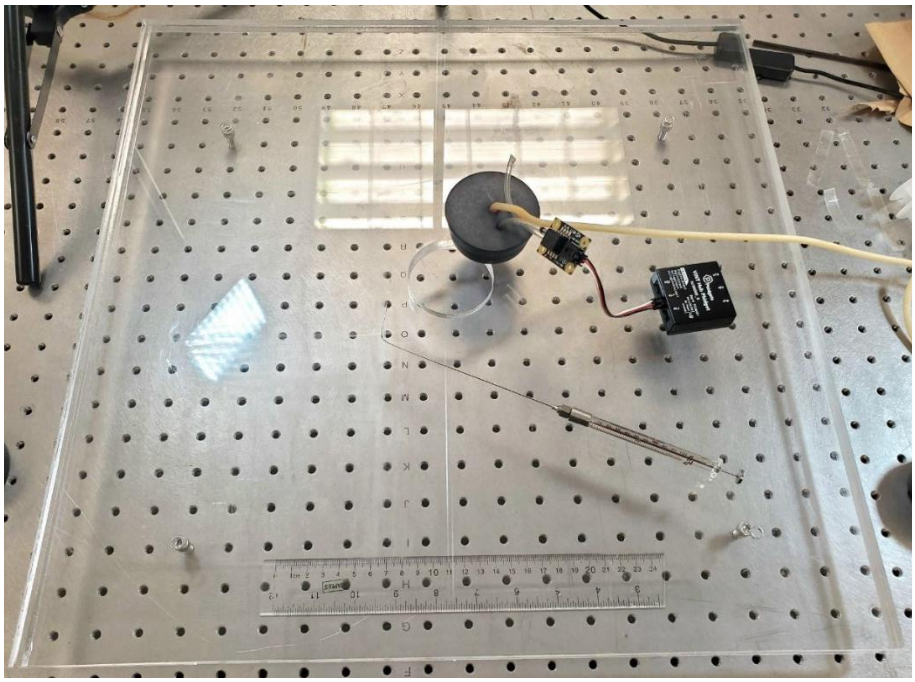

Figure 4.3. Experimental setup of the Hele-Shaw cell with the black circular rubber stopper, the Phidget pressure sensor, and the 10 μm syringe used in the experiments. We used the syringe to deposit the surfactant solution on the inner interface through the circular opening at the top of the Hele-Shaw cell. After hexane was evaporated, the stopper was pushed into the circular opening to seal the inner phase.

We used two acrylic sheets that were 50 cm tall, 50 cm wide, and 0.5 inch thick to construct the Hele-Shaw cell as shown in Fig. 4.3. We used laser to cut a hole with a radius of 4 cm at the center of the top sheet. A rubber stopper connecting the inlet tube and the Phidget pressure sensor would be pushed in the center opening as we start the experiment. Four washers with measured thickness were used to set the gap between the Hele-Shaw cells. We used air as the inner phase and liquid glycerol as the outer phase. We deposited the bulk glycerol solution between the Hele-Shaw cells with the gap width being 0.93 mm After the glycerol solution was deposited, we slowly pumped the air in to form a small circle with the initial radius being 5 cm. The surfactants dissolved in the hexane solutions were then deposited via a 10 μm syringe onto the inner surface of the glycerol

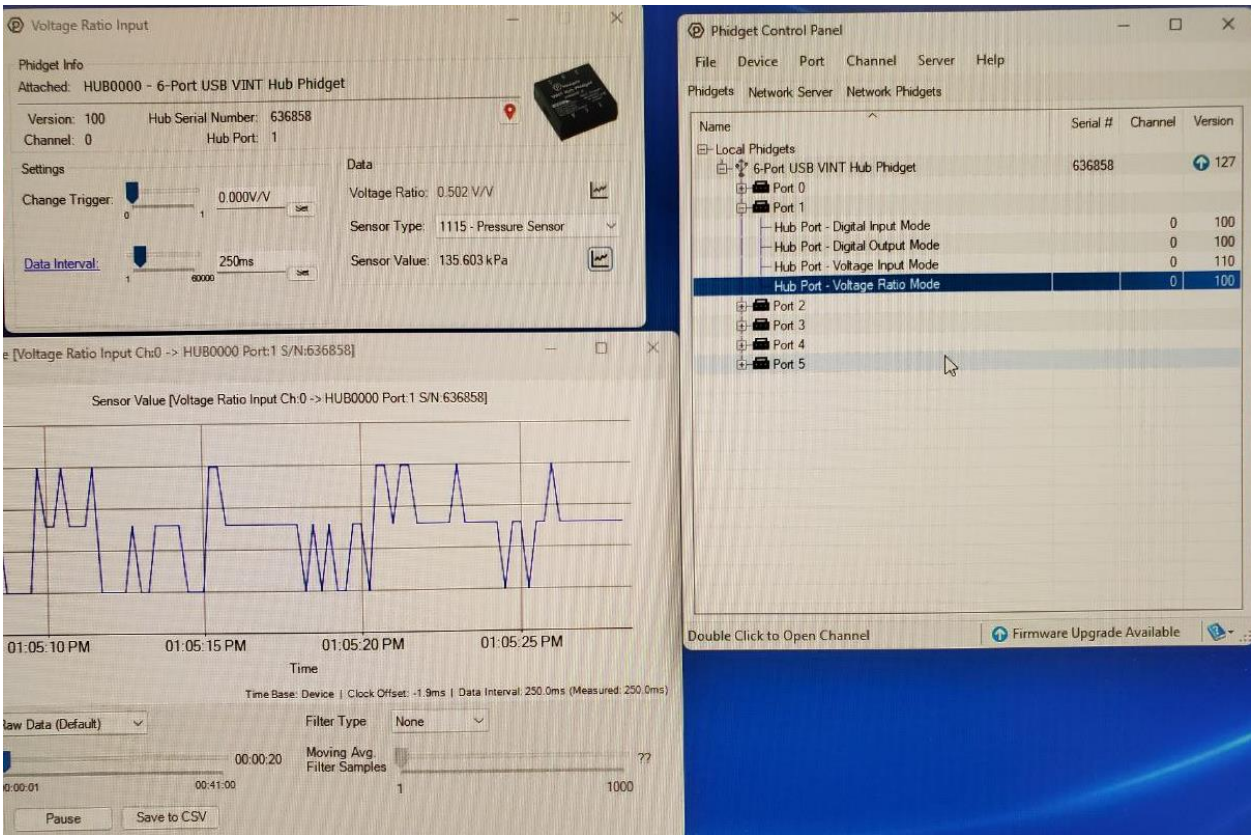

Figure 4.4. Phidget program interface. The pressure sensor function can be accessed by double clicking the "Hub Port-Voltage Ratio Mode" under the port in use (Port 1 in this figure) in the Phidget Control Panel. After the window "Voltage Ratio Input" appears, one can select "1115-Pressure Sensor" option in the drop-down menu under Data section. Clicking the graph icon to the right of "Sensor Value" can open a real-time graph of the measured pressure as shown at the bottom left.

solution. We let the hexane evaporate for at least 30 min before connecting the inner opening with the tube and the pressure sensor. The initial surfactant surface concentration was initially set to be two Angstrom/molecule. As we conducted more experiments, more surfactant surface concentrations were explored. The experiments were carried out at room temperature around 20 deg C and a relative humidity of 20% to 50% depending on the day. The initial bubble radius was set to be 5 cm and 12 cm for different experiments. Multiple Hele-Shaw cell gap widths were also

explored at 0.93 mm and 2.1 mm. The frequencies of the oscillation were investigated at 0.02 Hz and 0.04 Hz.

To measure the pressure of the inner phase, we used Phidget pressure sensor. The pressure sensor shown in Fig 4.3 was connected to the computer via a USB cable. The Phidget software, which is free to download on their official website, would automatically detect the sensor upon opening as shown in Fig. 4.4. As the sensor was plugged into Port 1 of the hub, the control panel would provide a list of options under Port 1. Double clicking the "Hub Port-Voltage Ratio Mode" under Port 1 in the Phidget Control Panel would open the "Voltage Ratio Input" window. We could then select the "1115-Pressure Sensor" option in the drop-down menu under Data section on the right side of the window. Clicking the graph icon to the right of "Sensor Value" can open a real-time graph of the measured pressure as shown at the bottom left. Saving all the measured pressure data to a CSV file was also an option.

4.2.3. Challenges and discussions

We processed the film from the experiments and processed the video using image-capturing software such as ImageGrab. We compared the timestamp of when the bubble oscillated and the time when the oscillatory motor rotated. Based on the theoretical analysis, the oscillation of the bubble should experience a slight delay than the oscillation of the pump due to the presence of surfactants at the bubble interface. One of the key challenges we faced was that the order of the time delay is around 0.1 second, which is close to the video capturing frame and is small enough to be within the human error in terms of the image selection when determining when the bubble finished one cycle of oscillation. The second challenge is the lack of an automated process to consistently process the video and select the image marking the point of the bubble completing an

oscillatory cycle. All image selections relied on human judgment, which may introduce error and inconsistency.

The preliminary experimental data we obtained were not able to produce reasonable results when estimating the surface viscosities of the surfactants. The subpar results were likely due to the challenges pointed out above. In terms of future planning, we believe a better camera with a high frame rate is necessary. In addition, using more advanced video processing software which has the capability to track surfaces would provide both efficiency and consistency to the data analysis. Addressing these two needs would provide accurate and meaningful data to estimate the surfactant surface viscosities.

4.3. Extensional work on viscous fingering

4.3.1. Experiments

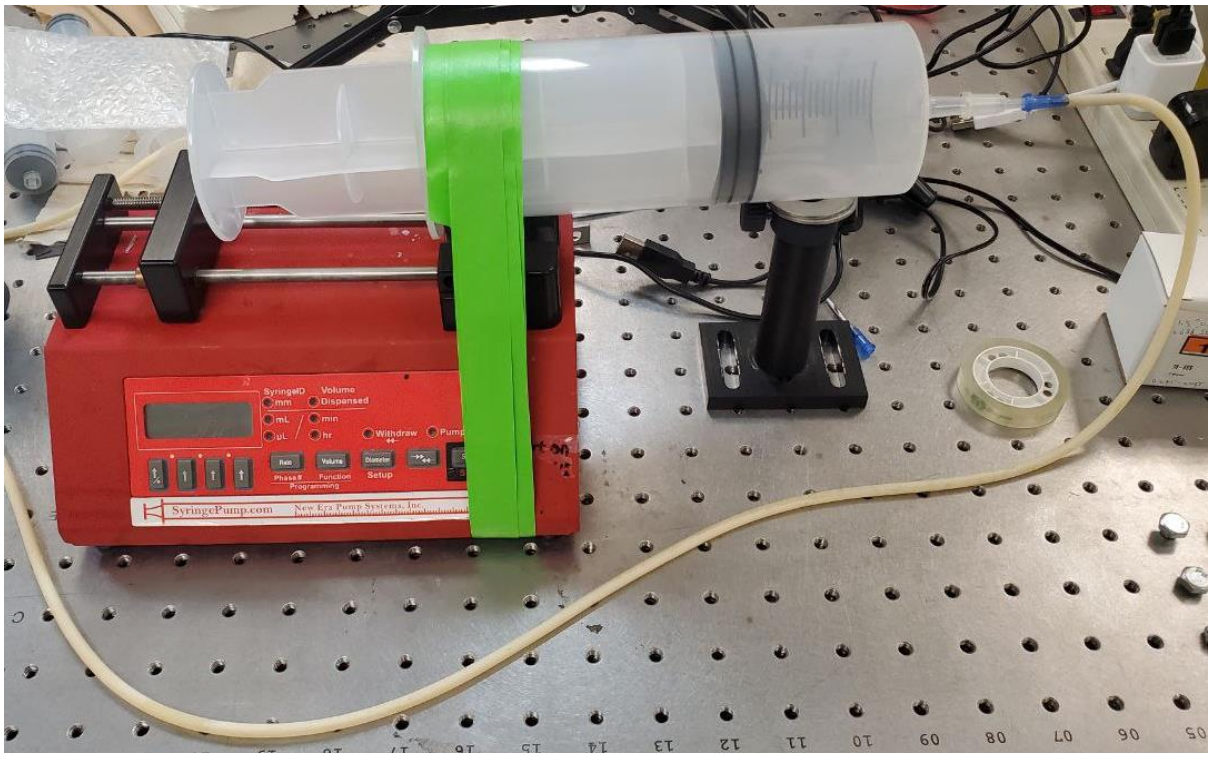

Figure 4.5. Experimental setup of the syringe pump holding a 500 ml syringe. We set the syringe pump to 74.1ml/min to produce an actual air flow rate of $0.39\ ml/s$. The air then flows through the rubber tube to provide pressure as the inner phase.

We aimed to conduct experiments to investigate the effect of surfactants on viscous fingering in both the short term and the long term. The experimental set up was similar to the schematic shown in Fig. 4.1 except the oscillatory pump was switched to a syringe pump instead to support the viscous fingering experiments. The set up of the Hele-Shaw cell is shown in Fig. 4.3. Similar to the oscillatory experiment mentioned in the previous section, we used air as the inner phase and liquid glycerol as the outer phase. We deposited the bulk glycerol solution between the Hele-Shaw cells with the gap width being $0.93\ mm$. We slowly pump the air in to form a small circle with the initial radius being $5\ cm$ after the glycerol solution was deposited. The surfactants dissolved in hexane solutions were then deposited via a syringe onto the inner surface of the glycerol solution. We let the hexane evaporate for at least $30\ min$ before connecting the inner opening with the tube

and the Phidget pressure sensor. The initial surfactant surface concentration was again set to be two Angstrom/molecule, initially. As we conducted more experiments, more surfactant surface concentrations were explored. We used Dipalmitoyl phosphatidylcholine (DPPC), an insoluble surfactant common in lung alveoli, and Arachidyle alcohol (AA), another insoluble surfactant common in cosmetics, for the experiments. The syringe pump was NE-1000 from The New Era Pump Systems, Inc. We installed a 500 ml syringe and set the syringe pump to 74.1ml/min to produce an actual air flow rate of 0.39 ml/s as shown in Fig. 4.5. In what follows, we show the experimental results and discuss what we have learned from the experimental observations. We hypothesized that with the addition of surfactants at the interface, the formation of the viscous fingers would be delayed and the number of fingers formed would be reduced.

4.3.1.1 Experiments using DPPC.

We explored various flow rates, gap widths, and surfactant concentrations in order to obtain consistent results. However, the results fluctuated depending on the day of the experiment. Certain experiments showed results that were consistent with our hypothesis while others did not. We document some of the results we obtained in this chapter.

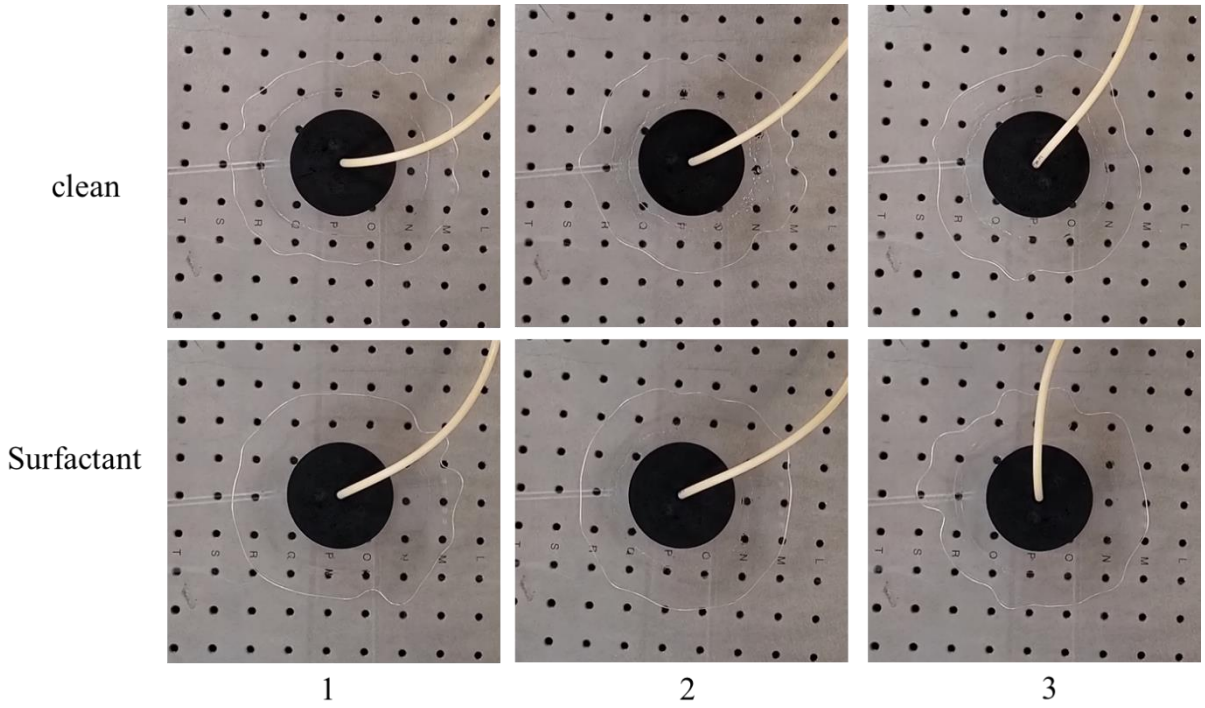

Figure 4.6. Results of three repeats of viscous fingering experiments using DPPC with a flowrate of $0.35ml/s$, gap width of $0.93\,mm$, an initial surface concentration of 2 angstrom/molecule at $t = 30s$. The initial radius was set to be $5\,cm$. The top row represents the experiments with clean interfaces and the bottom row shows the experiments with surfactants.

Figure 4.6 shows the three repeats of viscous fingering experiments using DPPC with a flowrate of $0.35ml/s$, gap width of $0.93\,mm$, an initial surface concentration of 2 angstrom/molecule taken at $t = 30s$. The initial radius was set to be $5\,cm$. The top row represents the experiments with clean interfaces and the bottom row shows the experiments with surfactants. While experiments 1 and 2 show some degree of suppression of finger formation when surfactants were added, the results of experiment 3 were not as obvious.

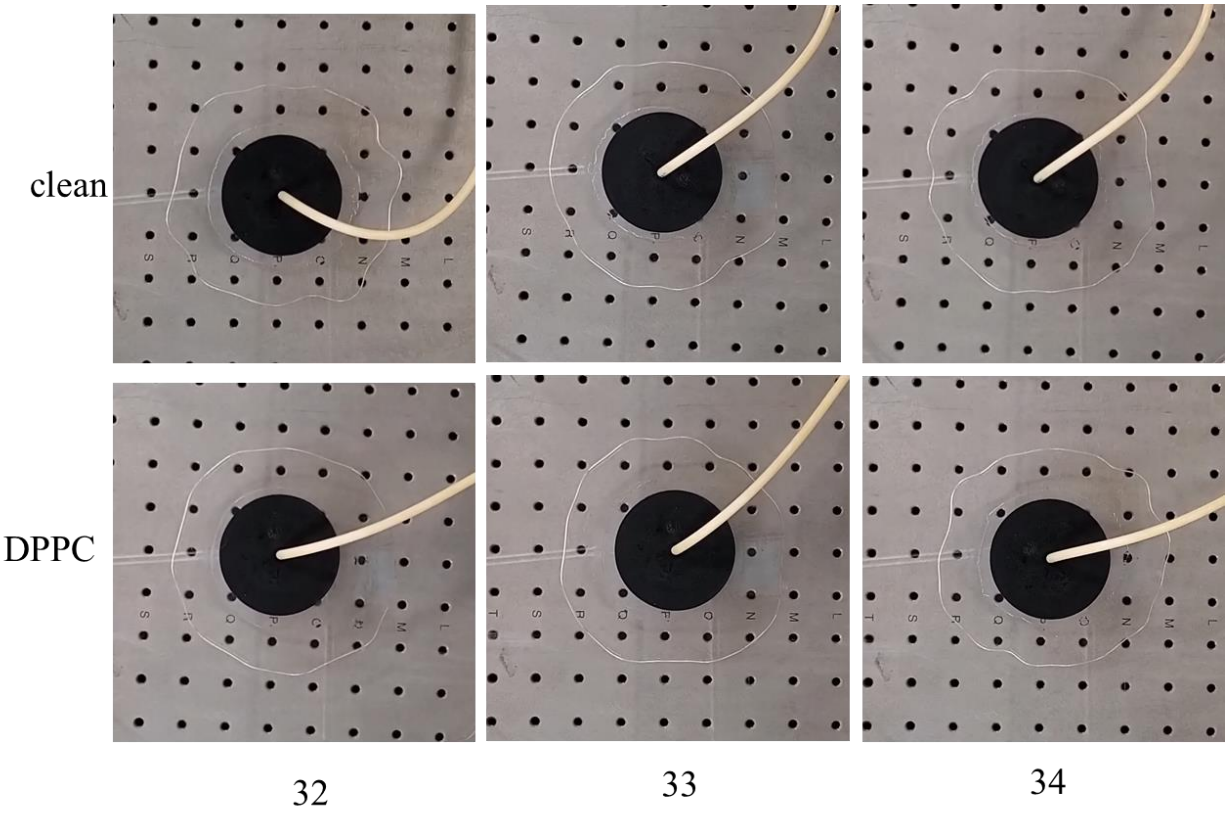

Figure 4.7. Results of three repeats of viscous fingering experiments using DPPC with a flowrate of $0.39ml/s$, gap width of $0.93\,mm$, an initial surface concentration of 2 angstrom/molecule at $t = 30s$. The initial radius was set to be 4 cm. The top row represents the experiments with clean interfaces and the bottom row shows the experiments with surfactants.

Figure 4.7 shows the results of three repeats of viscous fingering experiments using DPPC at $0.39ml/s$ with a surface concentration of 2 angstrom/molecule taken at $t = 30s$. The initial radius was set to be 4 cm. The top row represents the experiments with clean interfaces and the bottom row shows the experiments with surfactants. We again observed some suppression of the viscous finger formation in trail 32. However, trials 33 and 34 produced similar results between the experiment with the clean interface and the one with DPPC deposited.

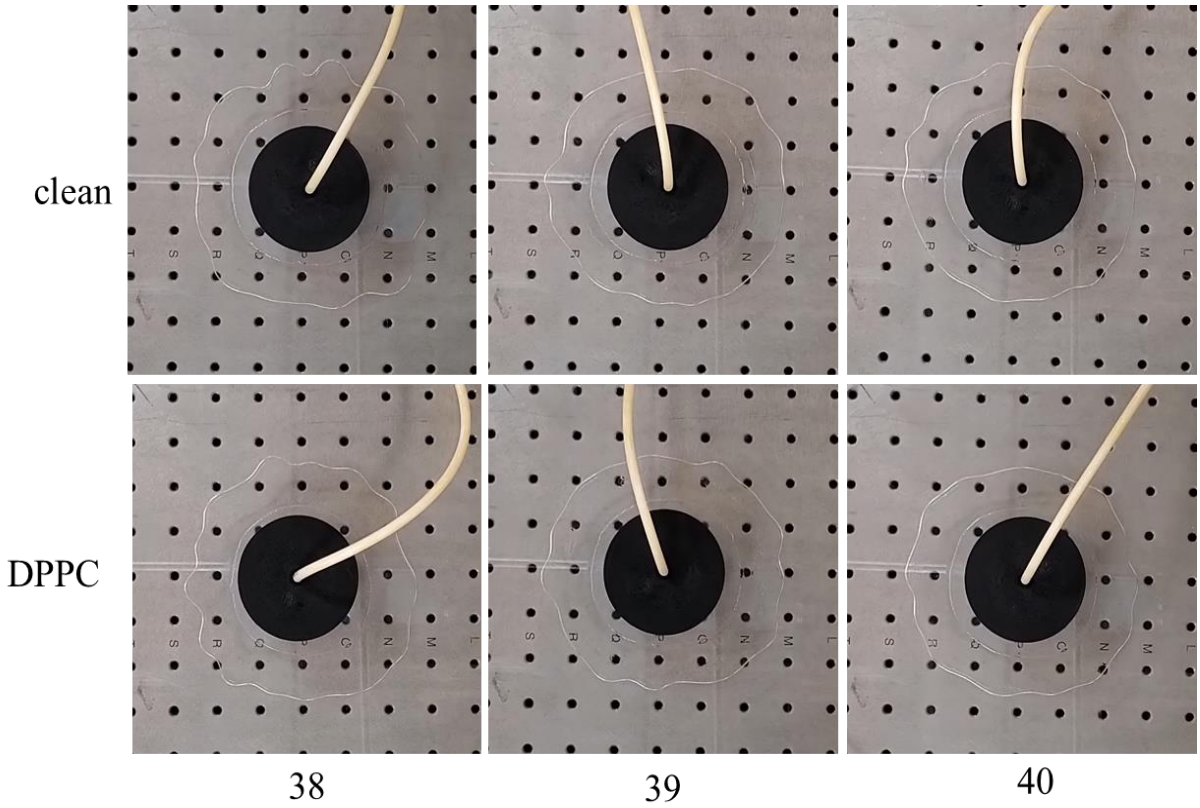

Figure 4.8. of three repeats of viscous fingering experiments using DPPC with a flowrate of 0.39ml/s, gap width of 0.59 mm, an initial surface concentration of one angstrom/molecule at $\text{t} = 30\text{s}$. The initial radius was set to be 4 cm. The top row represents the experiments with clean interfaces and the bottom row shows the experiments with surfactants.

We also explored a thinner gap width and obtain the results to investigate whether the gap width would make a difference in the consistency of the results. Fig 4.8 shows the results of three repeats of viscous fingering experiments using DPPC at $0.39ml/s$ with a surface concentration of one angstrom/molecule taken at $t = 30s$. The initial radius was set to be $4\ cm$. The top row represents the experiments with clean interfaces and the bottom row shows the experiments with surfactants. For all these three experiments, we did not observe any obvious suppression of viscous finger formations after DPPC was deposited.

4.3.1.2 Experiments using AA.

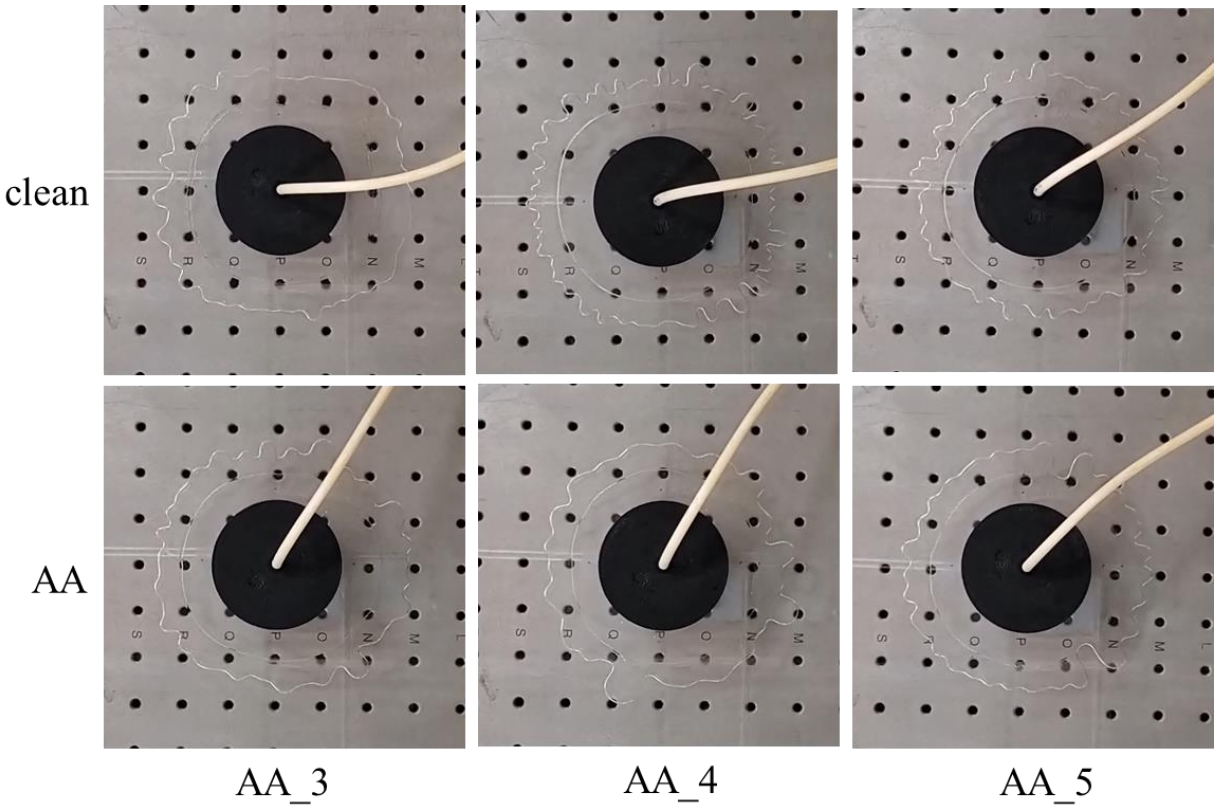

Figure 4.9. Results of three repeats of viscous fingering experiments using AA with a flowrate of 1 ml/s, gap width of 0.59 mm, an initial surface concentration of one angstrom/molecule taken at t = 5s. The initial radius was set to be 5 cm. The top row represents the experiments with clean interfaces and the bottom row shows the experiments with surfactants.

We decided to switch to a faster flow rate for experiments using AA. Fig 4.9 shows the results of three repeats of viscous fingering experiments using AA at 1 ml/s with a surface concentration of one angstrom/molecule taken at $t = 5s$. The initial radius was set to be 5 cm. The top row represents the experiments with clean interfaces and the bottom row shows the experiments with surfactants. One can argue that for trial AA_4, we observed some suppression of viscous finger

formation and the formation of wider fingers. However, we did not observe too much difference for trials AA_3 and AA_5.

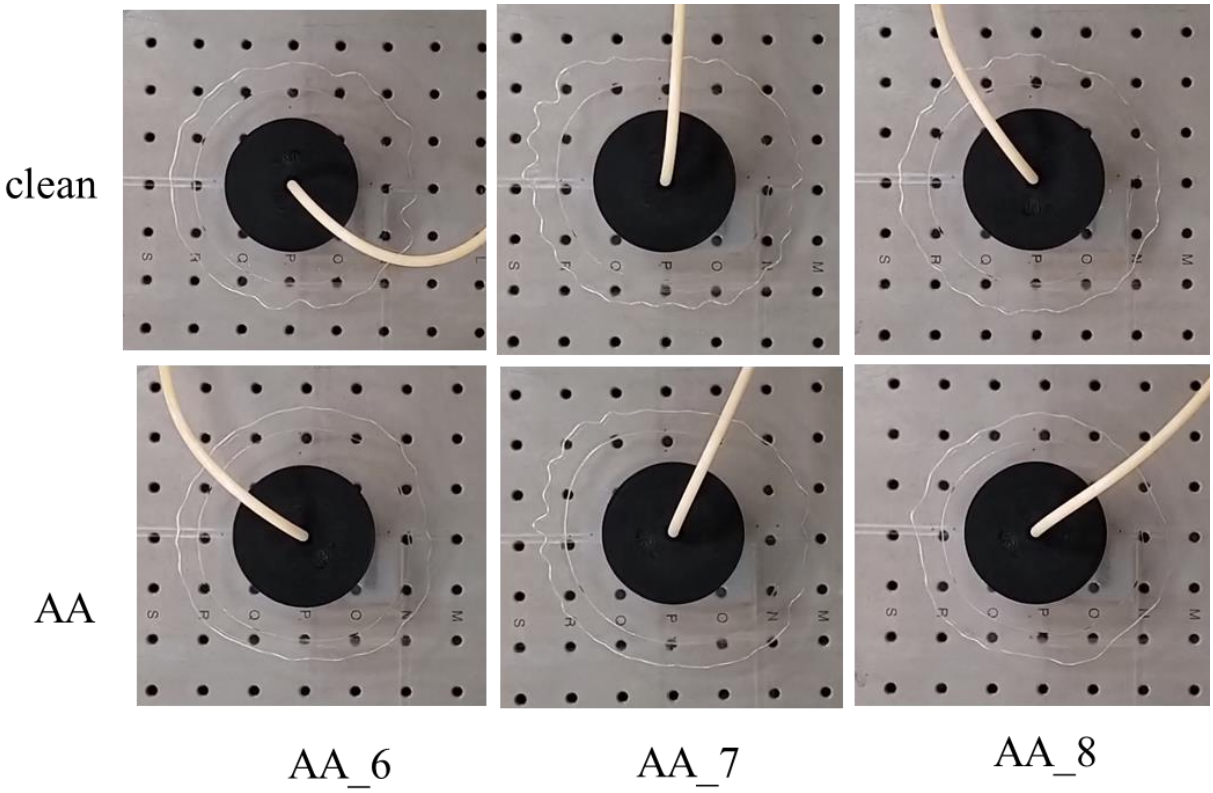

Figure 4.10. Results of three repeats of viscous fingering experiments using AA with a flowrate of 1 ml/s, gap width of 0.59 mm, an initial surface concentration of one angstrom/molecule taken at t = 5s. The initial radius was set to be 5 cm. The top row represents the experiments with clean interfaces and the bottom row shows the experiments with surfactants.

Figure 4.10 shows the results of another set of three repeats of viscous fingering experiments using AA at 1 ml/s with a surface concentration of one angstrom/molecule taken at $t = 5s$. We again observed some inconsistency among the three repeats. While trail AA_6 showed some promising results that were consistent with the hypothesis of surfactants slowed the viscous finger formation, trials AA_7 and AA_8 did not produce different results when the surfactants were added. We also did a number of other repeated experiments that were at various flow rates, surface concentrations,

and gap widths, but the main issue was inconsistency similar to the experimental results documented in this section.

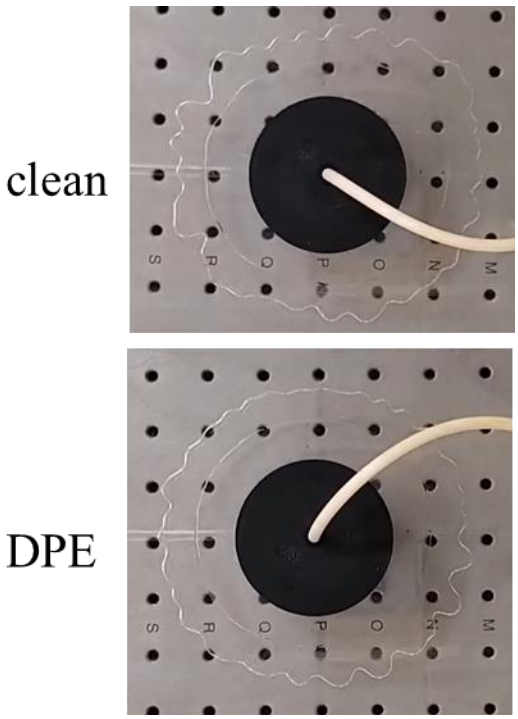

Figure 4.11. Results of three repeats of viscous fingering experiments using DPE with a flowrate of $1\ \mathrm{ml/s}$, gap width of $0.59\ \mathrm{mm}$, an initial surface concentration of one angstrom/molecule at $t = 5\mathrm{s}$. The initial radius was set to be $5\ \mathrm{cm}$. The top row represents the experiments with clean interfaces and the bottom row shows the experiments with surfactants.

We also explored other large molecules as they would exhibit stronger surface rheology effects. We used 1-palmitoyl-2-(10,12-tricosadiynoyl)-sn-glycero-3-phosphoethanolamine by Avanti or 16:0-23:2 Diyne PE (DPE) for short to increase the effect of surface viscosity in hope to obtain more appreciable results. However, the results remained inconsistent. Fig. 4.11 shows one set of results of viscous fingering produced using DPE compared to the experiment with a clean interface. The results were again not as obvious after we added the surfactants.

Overall, the main issue was consistency. While we were able to observe the suppression of viscous finger formations after we added surfactants for some experiments, we were not able to generate consistent results. Approximately half of the total number of experiments we ran failed to show an appreciable difference between the experiments with clean interfaces and the ones with surfactants deposited. One big issue we noticed was the glycerol sticking to the top and bottom of the inner surfaces of the Hele-Shaw cell, which meant the newly generated interfaces may be depleted of surfactants as the glycerol interface with surfactants would be stuck to the surface. While we did use a glycerol and water mixture to tackle this problem, the results were still inconsistent. Another factor that might affect the experiments would be the evaporation of the hexane solvent. In both experiments with the clean interface and with surfactants, we deposited hexane solution to the interface and then waited for the solvent to evaporate. It was critical not to conduct viscous fingering experiments while there was hexane residue left. Hexane residue at the inner surface acted almost as a lubricant that helped glycerol to slide more easily, leading to faster and more viscous finger formations. The last factor that may affect the viscous fingering experiments was the relative humidity of the room. As water was soluble in glycerol, the glycerol viscosity maybe decreased slightly while we were depositing glycerol on the Hele-Shaw cell and waiting for the hexane to evaporate. While designing for the experiments, one limiting factor that controlled the gap width of the Hele-Shaw cell was the width of the cannula attached to the tip of the syringe. Although we were able to reduce the gap width to $0.59\ mm$, any gap width that is smaller would be difficult as the cannula would not fit in between the Hele-Shaw gap to deposit the surfactants to the inner surface.

As a result, all future designs should take the factors mentioned above into consideration. The current experiments were carried out on a relatively large scale. Future students may design and

prepare experiments that are on a smaller scale to achieve better control. A different Hele-Shaw cell material could also be explored. We used acrylic instead of glass as it is easier for customization via drilling or laser cutting. However, there might be an alternative option that provides the same flexibility as acrylic while providing a smoother surface that prevents the bulk fluid from sticking.

4.3.2. COMSOL simulations

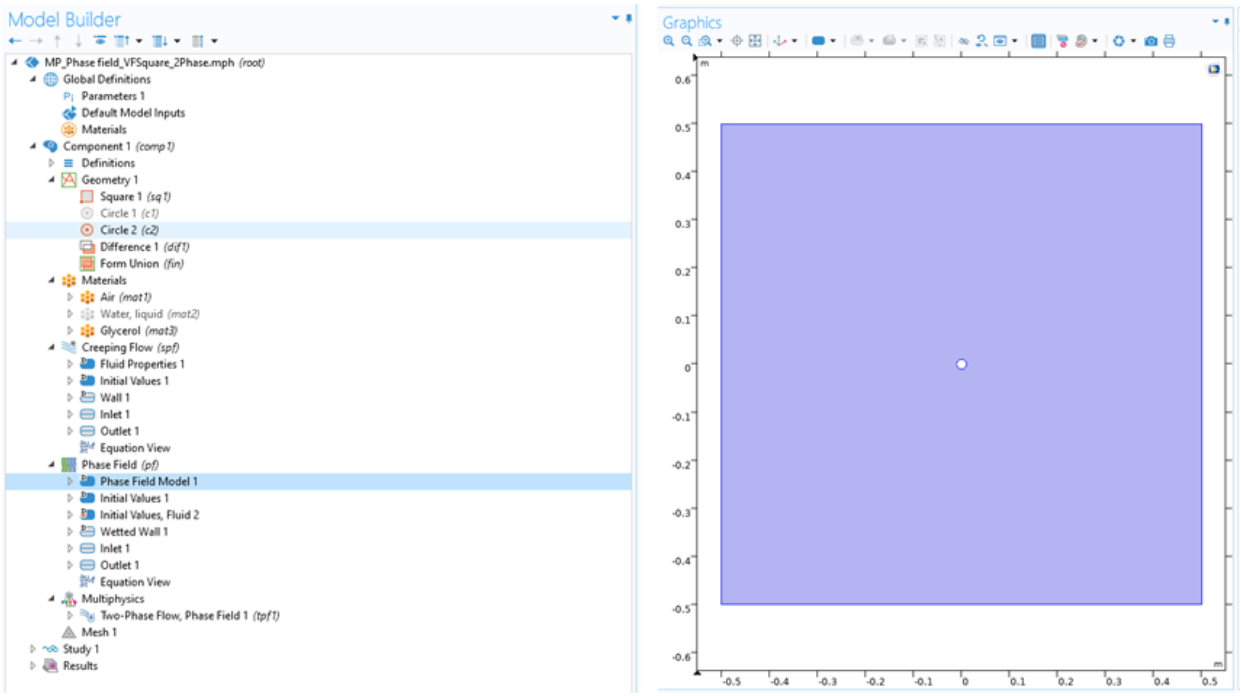

Figure 4.12. COMSOL interface using the phase Field method to design viscous fingering simulation.

We explored using COMSOL to simulate viscous fingering with surfactants present at the interface. We ran a 2-D simulation with the height and width of the Hele-Shaw cell being $1m$. The gap width of the Hele-Shaw cell was set to be $0.93\ mm$. We used air as the inner phase and glycerol as the

outer phase. The initial radius of the inner phase was set to be $1\ cm$. The inlet flow rate was the inner boundary condition and was $1e-6\ m^s/s$.

The first method we tried was the phase field method in the CFD module of COMSOL as shown in Fig. 4.12. The method used a phase factor, ϵ_{pf} (SI: m), to control the "interface" thickness. The "interface" consisted of a concentration gradient of the two phases. The smaller the phase factor, the shaper the concentration gradient would be across the "interface." We used the default value of ϵ_{pf}, which was half of the maximum mesh element size in the region through which the interface passes. There was also a mobility tuning parameter, χ (SI: $m * s/kg$), associated with the phase field method. The tuning parameter determines the time scale of the Cahn-Hilliard diffusion and governs the diffusion-related time scale for the interface. We used the default value of $1\ m \cdot s/kg$ as it was recommended as a good starting point for most models.

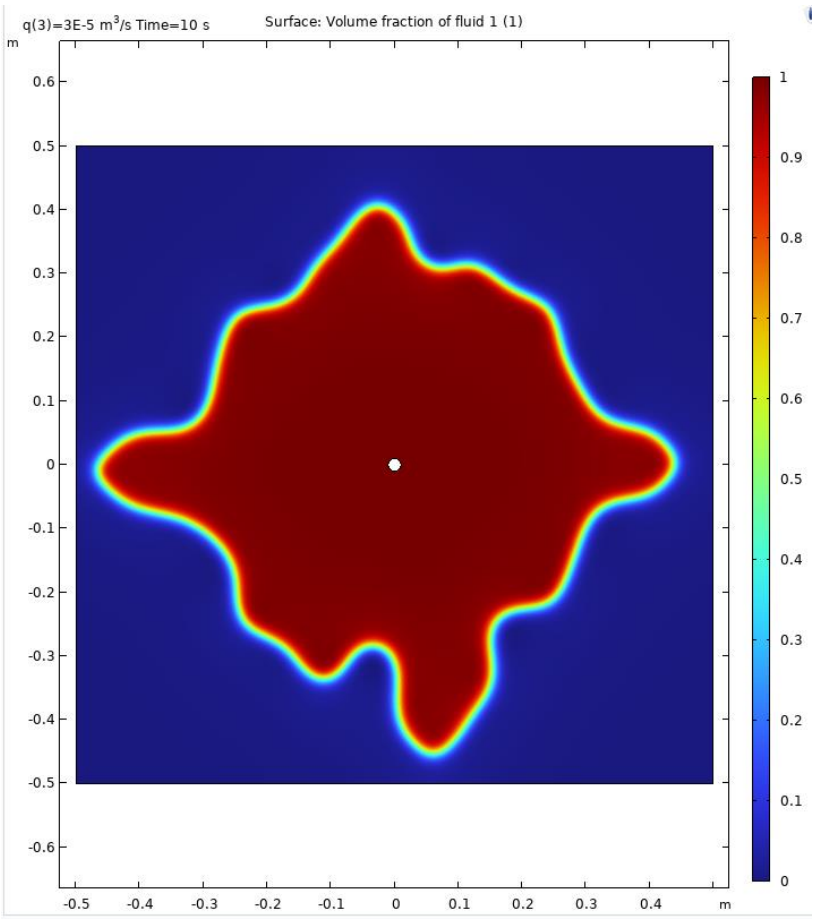

Figure 4.13. Viscous fingering simulation using COMSOL phase field method at simulation time $t = 10s$. The inner phase is air (red) and the outer phase is glycerol (blue).The gap width of the Hele-Shaw cell was 0.93 mm. The initial radius of the inner phase was set to be 1 cm. The inlet flow rate was the inner boundary condition and was $1e-6\ m^s/s$.

Figure 4.13. shows the viscous fingering simulation results at simulated time $t = 10s$ obtained using the settings described above. We obtained good results showing distinct fingering phenomena of air invading glycerol. The simulated "interface" was represented by a concentration gradient and was shown in the simulated result. As there was no specified interface, it was difficult to define the surfactant surface concentration using an isotherm. In addition, the Marangoni flows due to the surface concentration gradient would not be captured as there was not a defined interface in this method.

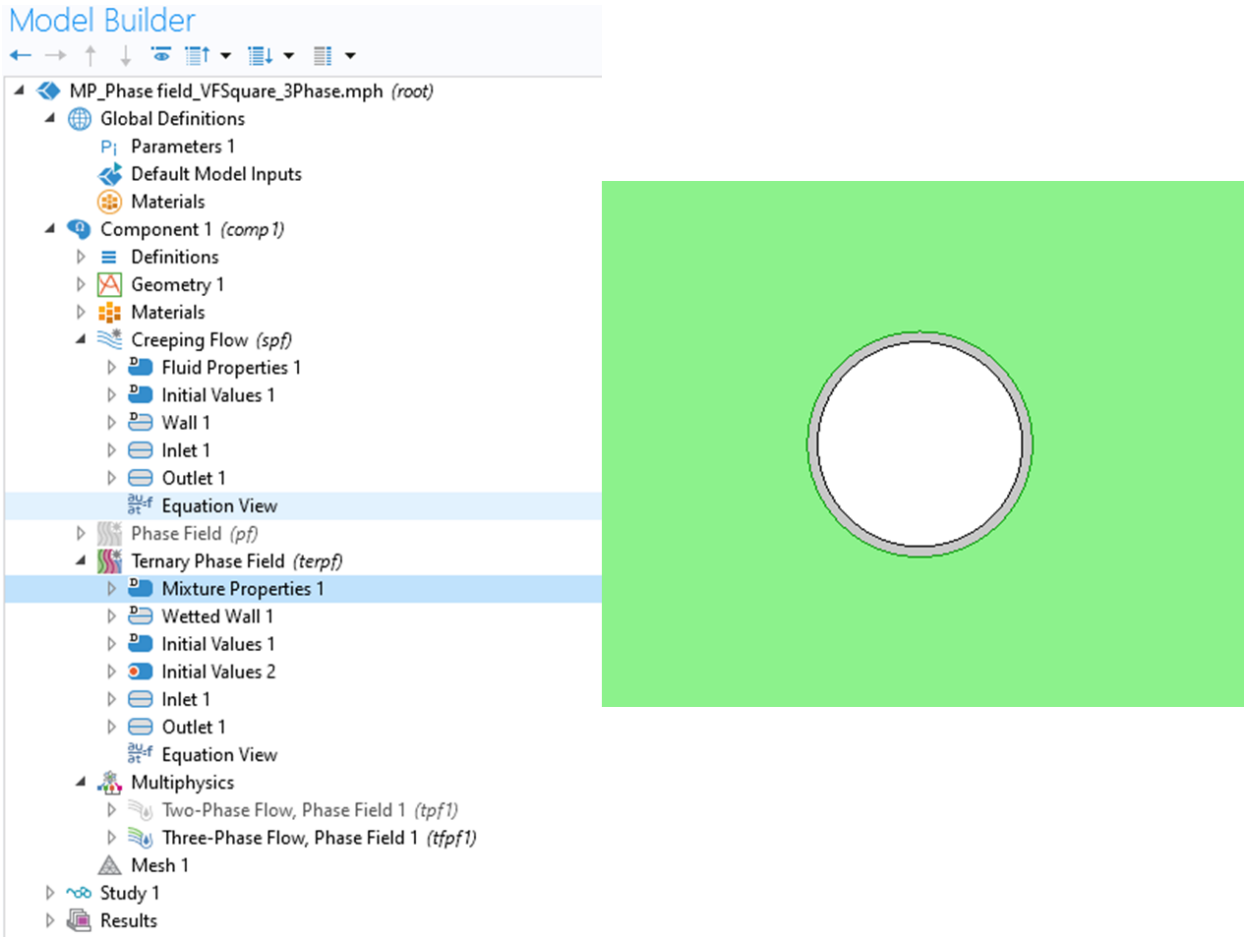

Figure 4.14. COMSOL interface using three phases to design viscous fingering simulation.

Alternatively, we tried to implement an extremely thin layer between the inlet and the bulk layer in the simulation to model the surfactant as shown in Fig. 4.14 as most of the packages characterizing two-phase flows did not have a distinct interface. We approximated the surfactant monolayer as an extremely thin third phase (grey in Fig. 4.14) between the inner and the outer phases (green in Fig. 4.14). Using the similar setup as described above, we used a ternary phase field to simulate the viscous fingering dynamics. The challenge with the ternary method was that the program was not stable enough to show meaningful results. We suspected the thin layer introduced too much instability to the simulation as the interface deformed and stretched due to the inlet.

Overall, there are two methods using COMSOL that were explored to simulate viscous fingering phenomena with surfactants at the interface. Each method had its own challenges. As most of the multiphase simulations do not have a specified interface but a thin band with a sharp concentration gradient across the phases, it is generally more challenging to capture the exact surface transport dynamics and the impact of surfactants. If using a two-phase model, it is recommended to use a program that provides more flexibility in terms of customization. It is possible to include the governing equations to capture the changes in the surfactant surface concentrations and surface flow. However, COMSOL does not offer that flexibility. Other software such as Open Foam might be a better option. The second method is to simulate the surfactant layer using an extremely thin third phase. The challenge of this method is the stability of the third phase. The surfactant phase needs to be elastic or stretchable along the surface deformation. We were not able to use COMSOL to run simulations that were stable enough to produce meaningful results.

Appendix. A Supporting information for “Influence of surface rheology on viscous fingering.”

A.1 Useful equations in cylindrical coordinates

When $\boldsymbol{n} = \hat{\boldsymbol{e}}_{\boldsymbol{r}}$ only, i.e. $n_r = 1, n_\theta = 0$,

$$\boldsymbol{\nabla} = \hat{\boldsymbol{e}}_{\boldsymbol{r}} \frac{\partial}{\partial r}() + \hat{\boldsymbol{e}}_{\boldsymbol{\theta}} \frac{1}{r} \frac{\partial}{\partial \theta}()$$

$$\boldsymbol{\nabla}_{\boldsymbol{s}} = \hat{\boldsymbol{e}}_{\boldsymbol{\theta}} \frac{1}{r} \frac{\partial}{\partial \theta}()$$

$$\boldsymbol{\nabla} \cdot \boldsymbol{n} = \frac{1}{r}$$

$$\boldsymbol{\nabla n} = \frac{1}{r} \hat{\boldsymbol{e}}_{\boldsymbol{\theta}} \hat{\boldsymbol{e}}_{\boldsymbol{\theta}}$$

$$\boldsymbol{\nabla}_{\boldsymbol{s}} \cdot \boldsymbol{n} = \frac{1}{r}$$

$$\boldsymbol{\nabla}_{\boldsymbol{s}} \boldsymbol{n} = \frac{1}{r} \hat{\boldsymbol{e}}_{\boldsymbol{\theta}} \hat{\boldsymbol{e}}_{\boldsymbol{\theta}}$$

$$\boldsymbol{\nabla} \cdot \boldsymbol{u_j} = -\frac{\partial^2 \phi_j}{\partial r^2} - \frac{1}{r} \frac{\partial \phi_j}{\partial r} - \frac{1}{r^2} \frac{\partial^2 \phi_j}{\partial \theta^2}$$

$$\boldsymbol{\nabla u_j} = -\hat{\boldsymbol{e}}_{\boldsymbol{r}} \hat{\boldsymbol{e}}_{\boldsymbol{r}} \frac{\partial^2 \phi_{\boldsymbol{j}}}{\partial r^2} - \hat{\boldsymbol{e}}_{\boldsymbol{r}} \hat{\boldsymbol{e}}_{\boldsymbol{\theta}} \left(\frac{1}{r} \frac{\partial^2 \phi_j}{\partial r \partial \theta} - \frac{1}{r^2} \frac{\partial \phi_j}{\partial \theta} \right) - \hat{\boldsymbol{e}}_{\boldsymbol{\theta}} \hat{\boldsymbol{e}}_{\boldsymbol{r}} \left(\frac{1}{r} \frac{\partial^2 \phi_j}{\partial r \partial \theta} - \frac{1}{r^2} \frac{\partial \phi_j}{\partial \theta} \right) - \hat{\boldsymbol{e}}_{\boldsymbol{\theta}} \hat{\boldsymbol{e}}_{\boldsymbol{\theta}} \left(\frac{1}{r} \frac{\partial \phi_j}{\partial r} + \frac{1}{r^2} \frac{\partial^2 \phi_j}{\partial \theta^2} \right)$$

$$\boldsymbol{\nabla}_{\mathbf{s}} \cdot \boldsymbol{u_j} = -\frac{1}{r} \frac{\partial \phi_j}{\partial r} - \frac{1}{r^2} \frac{\partial^2 \phi_j}{\partial \theta^2}$$

$$\boldsymbol{\nabla}_{\mathbf{s}} \boldsymbol{u_1} = \hat{\boldsymbol{e}}_{\boldsymbol{\theta}} \hat{\boldsymbol{e}}_{\boldsymbol{r}} \left[\frac{1}{r^2} \frac{\partial \phi_j}{\partial \theta} - \frac{1}{r} \frac{\partial^2 \phi_j}{\partial r \partial \theta} \right] + \hat{\boldsymbol{e}}_{\boldsymbol{\theta}} \hat{\boldsymbol{e}}_{\boldsymbol{\theta}} \left[-\frac{1}{r} \frac{\partial \phi_j}{\partial r} - \frac{1}{r^2} \frac{\partial^2 \phi_j}{\partial \theta^2} \right]$$

A.2 Derivation of equation (2.10) from equation (2.9)

From the main body of the paper, equation (2.9) is shown below,

$$\rho_s \frac{D\boldsymbol{u}}{Dt} - (\boldsymbol{n}\cdot\boldsymbol{\sigma_2} - \boldsymbol{n}\cdot\boldsymbol{\sigma_1})$$

$$= \boldsymbol{\nabla_s}\gamma - \gamma(\boldsymbol{\nabla_s}\cdot\boldsymbol{n})\boldsymbol{n} + (\kappa_s - \eta_s)\boldsymbol{\nabla_s}(\boldsymbol{\nabla_s}\cdot\boldsymbol{u}) - (\kappa_s - \eta_s)(\boldsymbol{\nabla_s}\cdot\boldsymbol{u})[\boldsymbol{\nabla_s}\cdot\boldsymbol{n}]\boldsymbol{n}$$

$$+\boldsymbol{\nabla_s}\cdot\{\eta_s[\boldsymbol{\nabla_s}\boldsymbol{u}\cdot\boldsymbol{I_s} + \boldsymbol{I_s}\cdot(\boldsymbol{\nabla_s}\boldsymbol{u})^{\boldsymbol{T}}]\}. \qquad (2.9)$$

In order to obtain the normal stress balance, we will neglect the inertia terms and dot a unit normal vector $\boldsymbol{n}$ to the right of equation (2.9),

The left-hand side (LHS) of equation (2.9) becomes

$$\boldsymbol{n}\cdot\boldsymbol{\sigma_1}\cdot\boldsymbol{n} - \boldsymbol{n}\cdot\boldsymbol{\sigma_2}\cdot\boldsymbol{n} = -(p_1 - p_2) + \boldsymbol{n}\cdot\boldsymbol{\tau_1}\cdot\boldsymbol{n} - \boldsymbol{n}\cdot\boldsymbol{\tau_2}\cdot\boldsymbol{n}.$$

As $\boldsymbol{\tau_j} = \boldsymbol{\eta_j}\left(\boldsymbol{\nabla u_j} + (\boldsymbol{\nabla u_j})^{\boldsymbol{T}}\right)$ for $j = 1{,}2$ and $\boldsymbol{n} = n_r\hat{\boldsymbol{e}}_{\boldsymbol{r}} + n_\theta\hat{\boldsymbol{e}}_{\boldsymbol{\theta}} + n_z\hat{\boldsymbol{e}}_{\boldsymbol{z}}$, we can express the velocity in terms of potential and obtain the LHS of equation (2.9)

$$-(p_1 - p_2) - 2\eta_1\left[n_r^2\frac{\partial^2\phi_1}{\partial r^2} + 2n_rn_\theta\left(\frac{1}{r}\frac{\partial^2\phi_1}{\partial r\partial\theta} - \frac{1}{r^2}\frac{\partial\phi_1}{\partial\theta}\right) + n_\theta^2\left(\frac{1}{r}\frac{\partial\phi_1}{\partial r} + \frac{1}{r^2}\frac{\partial^2\phi_1}{\partial\theta^2}\right)\right]$$

$$+ 2\eta_2\left[n_r^2\frac{\partial^2\phi_2}{\partial r^2} + 2n_rn_\theta\left(\frac{1}{r}\frac{\partial^2\phi_2}{\partial r\partial\theta} - \frac{1}{r^2}\frac{\partial\phi_2}{\partial\theta}\right) + n_\theta^2\left(\frac{1}{r}\frac{\partial\phi_2}{\partial r} + \frac{1}{r^2}\frac{\partial^2\phi_2}{\partial\theta^2}\right)\right].$$

Simplify the unit normal vector to be $\boldsymbol{n} = \hat{\boldsymbol{e}}_{\boldsymbol{r}}$, i.e. $n_r = 1, n_\theta = 0$, we obtain

$$-(p_1 - p_2) - 2\eta_1\frac{\partial^2\phi_1}{\partial r^2} + 2\eta_2\frac{\partial^2\phi_2}{\partial r^2}.$$

The right-hand side (RHS) of equation (9) becomes

$$\boldsymbol{\nabla_s}\gamma\cdot\boldsymbol{n} - \gamma(\boldsymbol{\nabla_s}\cdot\boldsymbol{n}) + (\kappa_s - \eta_s)\boldsymbol{\nabla_s}(\boldsymbol{\nabla_s}\cdot\boldsymbol{u})\cdot\boldsymbol{n} - (\kappa_s - \eta_s)(\boldsymbol{\nabla_s}\cdot\boldsymbol{u})[\boldsymbol{\nabla_s}\cdot\boldsymbol{n}]$$

$$+\boldsymbol{\nabla_s}\cdot\{\eta_s[\boldsymbol{\nabla_s u}\cdot\boldsymbol{I_s}+\boldsymbol{I_s}\cdot(\boldsymbol{\nabla_s u})^{\boldsymbol{T}}]\}\cdot\boldsymbol{n}.$$

As $\boldsymbol{n}=\hat{\boldsymbol{e}}_{\boldsymbol{r}}$, we can simplify each term of the RHS to be

$$\boldsymbol{\nabla_s}\gamma\cdot\boldsymbol{n}=\frac{1}{r}\frac{\partial\gamma}{\partial\theta}\hat{\boldsymbol{e}}_{\boldsymbol{\theta}}\cdot\hat{\boldsymbol{e}}_{\boldsymbol{r}}=0;$$

$$-\gamma(\boldsymbol{\nabla_s}\cdot\boldsymbol{n})=-\gamma\left(\frac{1}{r}\right)=-\gamma(\boldsymbol{\nabla}\cdot\boldsymbol{n});$$

$$(\kappa_s-\eta_s)\boldsymbol{\nabla_s}(\boldsymbol{\nabla_s}\cdot\boldsymbol{u})\cdot\boldsymbol{n}=(\kappa_s-\eta_s)\left(-\frac{1}{r^3}\frac{\partial^3\phi_1}{\partial\theta^3}-\frac{1}{r^2}\frac{\partial^2\phi_1}{\partial r\partial\theta}\right)\hat{\boldsymbol{e}}_{\boldsymbol{\theta}}\cdot\hat{\boldsymbol{e}}_{\boldsymbol{r}}=0;$$

$$-(\kappa_s-\eta_s)(\boldsymbol{\nabla_s}\cdot\boldsymbol{u})[\boldsymbol{\nabla_s}\cdot\boldsymbol{n}]=-(\kappa_s-\eta_s)\left(-\frac{1}{r^2}\frac{\partial^2\phi_1}{\partial\theta^2}-\frac{1}{r}\frac{\partial\phi_1}{\partial r}\right)(\boldsymbol{\nabla}\cdot\boldsymbol{n});$$

$$\boldsymbol{\nabla_s}\cdot\{\eta_s[\boldsymbol{\nabla_s u}\cdot\boldsymbol{I_s}+\boldsymbol{I_s}\cdot(\boldsymbol{\nabla_s u})^{\boldsymbol{T}}]\}\cdot\boldsymbol{n}$$

$$=-2\eta_s\frac{1}{r}\left(-\frac{1}{r^2}\frac{\partial^2\phi_1}{\partial\theta^2}-\frac{1}{r}\frac{\partial\phi_1}{\partial r}\right)\hat{\boldsymbol{e}}_{\boldsymbol{r}}\cdot\hat{\boldsymbol{e}}_{\boldsymbol{r}}+2\eta_s\left(-\frac{1}{r^2}\frac{\partial^2\phi_1}{\partial r\partial\theta}-\frac{1}{r^3}\frac{\partial^3\phi_1}{\partial\theta^3}\right)\hat{\boldsymbol{e}}_{\boldsymbol{\theta}}\cdot\hat{\boldsymbol{e}}_{\boldsymbol{r}}=$$

$$=-2\eta_s\frac{1}{r}\left(-\frac{1}{r^2}\frac{\partial^2\phi_1}{\partial\theta^2}-\frac{1}{r}\frac{\partial\phi_1}{\partial r}\right).$$

As a result, the RHS of equation (2.9) becomes

$$-\gamma(\boldsymbol{\nabla_s}\cdot\boldsymbol{n})-\left[(\kappa_s-\eta_s)(\boldsymbol{\nabla_s}\cdot\boldsymbol{n})+2\eta_s\frac{1}{r}\right]\left(-\frac{1}{r^2}\frac{\partial^2\phi_1}{\partial\theta^2}-\frac{1}{r}\frac{\partial\phi_1}{\partial r}\right).$$

With the addition of the transversal curvature, we can combine the terms and obtain:

$$\begin{aligned}-(p_1-p_2)-2\eta_1\frac{\partial^2\phi_1}{\partial r^2}+2\eta_2\frac{\partial^2\phi_2}{\partial r^2}&=-\gamma\left(\frac{2}{b}+\boldsymbol{\nabla_s}\cdot\boldsymbol{n}\right)\\&-\left[(\kappa_s-\eta_s)(\boldsymbol{\nabla_s}\cdot\boldsymbol{n})+2\eta_s\frac{1}{r}\right]\left(-\frac{1}{r^2}\frac{\partial^2\phi_1}{\partial\theta^2}-\frac{1}{r}\frac{\partial\phi_1}{\partial r}\right),\end{aligned}\qquad(2.10)$$

A.3 Derivation of equation (2.21) from equation (2.20)

Equation (2.20) is shown below, we will derive each term separately.

$$a\frac{\partial}{\partial r}\left[p_{01}+2\eta_1\frac{\partial^2\phi_{01}}{\partial r^2}-\left(p_{02}+2\eta_2\frac{\partial^2\phi_{02}}{\partial r^2}\right)\right]\Bigg|_{r=R}$$

$$+\left[p_{11}+2\eta_1\frac{\partial^2\phi_{11}}{\partial r^2}-\left(p_{12}+2\eta_2\frac{\partial^2\phi_{12}}{\partial r^2}\right)\right]\Bigg|_{r=R}+\gamma\left(\frac{a}{R(t)^2}+\frac{1}{R(t)^2}\frac{\partial^2 a}{\partial\theta^2}\right)$$

$$=-\frac{(\kappa_s+\eta_s)}{R(t)^2}\left[a\frac{\partial}{\partial r}\left(\frac{\partial\phi_{01}}{\partial r}\right)\Big|_{r=R}+\left(\frac{\partial\phi_{11}}{\partial r}\right)\Big|_{r=R}\right]$$

$$-\left[(\kappa_s+\eta_s)\left(-\frac{2a}{R(t)^3}\right)+(\kappa_s-\eta_s)\frac{n^2a}{R(t)^3}\right]*$$

$$\left[\left(\frac{\partial\phi_{01}}{\partial r}\right)\Big|_{r=R}+a\frac{\partial}{\partial r}\left(\frac{\partial\phi_{01}}{\partial r}\right)\Big|_{r=R}+\left(\frac{\partial\phi_{11}}{\partial r}\right)\Big|_{r=R}\right]. \qquad (2.20)$$

1st term on the LHS of equation (2.20):

$$a\frac{\partial}{\partial r}\left[p_{01}+2\eta_1\frac{\partial^2\phi_{01}}{\partial r^2}-\left(p_{02}+2\eta_2\frac{\partial^2\phi_{02}}{\partial r^2}\right)\right]\Bigg|_{r=R}$$

$$=a\frac{\partial}{\partial r}\left[p_{01}-p_{02}+2\eta_1\frac{\partial^2\phi_{01}}{\partial r^2}-2\eta_2\frac{\partial^2\phi_{02}}{\partial r^2}\right]\Bigg|_{r=R}$$

$$=a\left\{\frac{\partial}{\partial r}\left[\frac{\phi_{01}}{M_1}-\frac{\phi_{02}}{M_2}\right]\Big|_{r=R}+\frac{\partial}{\partial r}\left[2\eta_1\frac{\partial^2\phi_{01}}{\partial r^2}-2\eta_2\frac{\partial^2\phi_{02}}{\partial r^2}\right]\Bigg|_{r=R}\right\}$$

$$=a\left\{\left[\frac{1}{M_1}\frac{\partial\phi_{01}}{\partial r}-\frac{1}{M_2}\frac{\partial\phi_{02}}{\partial r}\right]\Big|_{r=R}+\frac{\partial}{\partial r}\left[\frac{Q}{\pi R(t)^2}(\eta_1-\eta_2)\right]\right\}$$

$$=a\left\{\left[\frac{1}{M_1}\left(-\frac{Q}{2\pi R(t)}\right)-\frac{1}{M_2}\left(-\frac{Q}{2\pi R(t)}\right)\right]-\frac{2Q}{\pi R^3(t)}(\eta_1-\eta_2)\right\}$$

$$= a\left\{-\frac{Q}{2\pi R(t)}\left(\frac{1}{M_1}-\frac{1}{M_2}\right) - \frac{2Q}{\pi R(t)^3}(\eta_1-\eta_2)\right\}$$

$$= -\frac{Q}{2\pi R(t)}a\left\{\left(\frac{1}{M_1}-\frac{1}{M_2}\right)+\frac{4}{R(t)^2}(\eta_1-\eta_2)\right\}$$

$$= -\frac{Q}{2\pi R(t)}\left\{\left(\frac{M_2-M_1}{M_1M_2}\right)+\frac{4}{R^2(t)}\left(\frac{b^2}{12M_1}-\frac{b^2}{12M_2}\right)\right\}a$$

$$= -\frac{Q}{2\pi R(t)}\left\{\left(\frac{M_2-M_1}{M_1M_2}\right)+\left(\frac{4b^2(M_2-M_1)}{12M_1M_2R(t)^2}\right)\right\}a$$

2nd and 3rd terms on the LHS of equation (2.20):

$$\left[p_{11}+2\eta_1\frac{\partial^2\phi_{11}}{\partial r^2}-\left(p_{12}+2\eta_2\frac{\partial^2\phi_{12}}{\partial r^2}\right)\right]\Bigg|_{r=R}+\gamma\left(\frac{a}{R(t)^2}+\frac{1}{R(t)^2}\frac{\partial^2 a}{\partial\theta^2}\right)$$

$$= \left[\frac{\phi_{11}}{M_1}-\frac{\phi_{12}}{M_2}+\left[2\eta_1\frac{\partial^2\phi_{11}}{\partial r^2}-2\eta_2\frac{\partial^2\phi_{12}}{\partial r^2}\right]\right]\Bigg|_{r=R}+\gamma\left(\frac{a}{R(t)^2}-\frac{n^2a}{R(t)^2}\right)$$

$$= -\left(\frac{Q}{2n\pi R(t)}+\frac{R}{n}\frac{f'(t)}{f(t)}\right)\left(\frac{1}{M_1}+\frac{1}{M_2}\right)a$$

$$+2\left(\frac{Q}{2n\pi R(t)}+\frac{R}{n}\frac{f'(t)}{f(t)}\right)\frac{n}{R(t)^2}[-\eta_1(n-1)-\eta_2(n+1)]a+\gamma\left(\frac{1}{R(t)^2}-\frac{n^2}{R(t)^2}\right)a$$

$$= \left\{-\gamma\frac{n^2-1}{R(t)^2}+\left(\frac{Q}{2n\pi R(t)}\right)\left[-\left(\frac{1}{M_1}+\frac{1}{M_2}\right)-\frac{2n}{R(t)^2}[\eta_1(n-1)+\eta_2(n+1)]\right]\right.$$

$$\left.+\left(\frac{R}{n}\right)\frac{f'(t)}{f(t)}\left[-\left(\frac{1}{M_1}+\frac{1}{M_2}\right)-\frac{2n}{R(t)^2}[\eta_1(n-1)+\eta_2(n+1)]\right]\right\}a$$

$$= \left\{ -\gamma \frac{n^2-1}{R(t)^2} - Q\left[\frac{M_1+M_2}{2M_1M_2n\pi R(t)} + \frac{\eta_1(n-1)+\eta_2(n+1)}{\pi R(t)^3} \right] \right.$$

$$\left. - \left(\frac{(M_1+M_2)R(t)}{M_1M_2n} + \frac{2\eta_1(n-1)+2\eta_2(n+1)}{R(t)} \right) \frac{f'(t)}{f(t)} \right\} a$$

$$= \left\{ -\gamma \frac{n^2-1}{R(t)^2} - Q\left[\frac{M_1+M_2}{2M_1M_2n\pi R(t)} + \frac{b^2[M_2(n-1)+M_1(n+1)]}{12M_1M_2\pi R(t)^3} \right] \right.$$

$$\left. - \left(\frac{(M_1+M_2)R(t)}{M_1M_2n} + \frac{b^2[M_2(n-1)+M_1(n+1)]}{6M_1M_2R(t)} \right) \frac{f'(t)}{f(t)} \right\} a$$

1st term on the RHS of equation (2.20):

$$-\left(\frac{\kappa_s+\eta_s}{R(t)^2}\right)\left[a\frac{\partial}{\partial r}\left(\frac{\partial \phi_{01}}{\partial r}\right)\Big|_{r=R} + \left(\frac{\partial \phi_{11}}{\partial r}\right)\Big|_{r=R}\right]$$

$$= -\left(\frac{\kappa_s+\eta_s}{R(t)^2}\right)\left[\frac{Qa}{2\pi R(t)^2} - a\frac{n}{R(t)}\left(\frac{Q}{2n\pi R(t)} + \frac{R}{n}\frac{f'(t)}{f(t)}\right)\right]$$

$$= -\left(\frac{\kappa_s+\eta_s}{R(t)^2}\right)\left[\frac{Q}{2\pi R(t)^2} - \frac{n}{R(t)}\left(\frac{Q}{2n\pi R(t)} + \frac{R}{n}\frac{f'(t)}{f(t)}\right)\right] a$$

$$= -\left(\frac{\kappa_s+\eta_s}{R(t)^2}\right)\left[\frac{Q}{2\pi R(t)^2} - \left(\frac{Q}{2\pi R(t)^2} + \frac{f'(t)}{f(t)}\right)\right] a$$

$$= \left(\frac{\kappa_s+\eta_s}{R(t)^2}\right)\frac{f'(t)}{f(t)} a.$$

2nd term on the RHS of equation (2.20):

$$= -\left(-(\kappa_s+\eta_s)\ \frac{2a}{R(t)^3} + (\kappa_s-\eta_s)\frac{n^2a}{R(t)^3}\right)\left[\left(\frac{\partial \phi_{01}}{\partial r}\right)|_{r=R} + a\frac{\partial}{\partial r}\left(\frac{\partial \phi_{01}}{\partial r}\right)|_{r=R} + \left(\frac{\partial \phi_{11}}{\partial r}\right)|_{r=R}\right]$$

$$= -\left(-(\kappa_s + \eta_s)\,\frac{2a}{R(t)^3} + (\kappa_s - \eta_s)\frac{n^2 a}{R(t)^3}\right)\left[-\frac{Q}{2\pi R} + a\frac{Q}{2\pi R^2} - a\frac{n}{R(t)}\left(\frac{Q}{2n\pi R(t)} + \frac{R}{n}\frac{f'(t)}{f(t)}\right)\right]$$

neglecting higher order terms,

$$= \frac{Q}{2\pi R}\left(-(\kappa_s + \eta_s)\,\frac{2a}{R(t)^3} + (\kappa_s - \eta_s)\frac{n^2 a}{R(t)^3}\right)$$

$$= \frac{Q}{2\pi R(t)^4}[n^2(\kappa_s - \eta_s) - 2(\kappa_s + \eta_s)]a$$

Combine all terms, we obtain

$$-\frac{Q}{2\pi R(t)}\left\{\left(\frac{M_2 - M_1}{M_1 M_2}\right) + \left(\frac{4b^2(M_2 - M_1)}{12M_1 M_2 R(t)^2}\right)\right\}a$$

$$+\left\{-\gamma\frac{n^2 - 1}{R(t)^2} - Q\left[\frac{M_1 + M_2}{2M_1 M_2 n\pi R(t)} + \frac{b^2[M_2(n-1) + M_1(n+1)]}{12M_1 M_2 \pi R(t)^3}\right]\right.$$

$$\left.-\left(\frac{(M_1 + M_2)R(t)}{M_1 M_2 n} + \frac{b^2[M_2(n-1) + M_1(n+1)]}{6M_1 M_2 R(t)}\right)\frac{f'(t)}{f(t)}\right\}a$$

$$= \left(\frac{\kappa_s + \eta_s}{R(t)^2}\right)\frac{f'(t)}{f(t)}a + Q\,\frac{n^2(\kappa_s - \eta_s) - 2(\kappa_s + \eta_s)}{2\pi R(t)^4}a$$

Rearrange to obtain equation (2.21):

$$-\gamma\frac{n^2 - 1}{R(t)^2} + Q\{\frac{(n-1)M_1 - M_2(n+1)}{2M_1 M_2 n\pi R(t)} - \frac{b^2[M_1(n-1) + M_2(n+1)]}{12M_1 M_2 \pi R(t)^3}$$

$$-\frac{n^2(\kappa_s - \eta_s) - 2(\kappa_s + \eta_s)}{2\pi R(t)^4}\} =$$

$$\left[\frac{(M_1 + M_2)R(t)}{M_1 M_2 n} + \frac{b^2[M_1(n+1) + M_2(n-1)]}{6M_1 M_2 R(t)} + \frac{\kappa_s + \eta_s}{R(t)^2}\right]\frac{f'(t)}{f(t)}. \qquad (2.21)$$

A.4 Derivation of equation (2.32) from equation (2.21)

Equation (2.21) is shown below

$$-\gamma\frac{n^2-1}{R(t)^2}+Q\{\frac{(n-1)M_1-M_2(n+1)}{2M_1M_2n\pi R(t)}-\frac{b^2[M_1(n-1)+M_2(n+1)]}{12M_1M_2\pi R(t)^3} -\frac{\left(n^2(\kappa_s-\eta_s)-2(\kappa_s+\eta_s)\right)}{2\pi R(t)^4}\}= \left[\frac{(M_1+M_2)R(t)}{M_1M_2n}+\frac{b^2[M_1(n+1)+M_2(n-1)]}{6M_1M_2R(t)}+\frac{\kappa_s+\eta_s}{R(t)^2}\right]\frac{f'(t)}{f(t)}. \quad (2.21)$$

Removing the terms associated with viscous normal stresses and surface viscous stresses, we obtain

$$-\gamma\frac{n^2-1}{R(t)^2}+Q\left\{\frac{(n-1)M_1-M_2(n+1)}{2M_1M_2n\pi R(t)}\right\}=\left[\frac{(M_1+M_2)R(t)}{M_1M_2n}\right]\sigma,$$

where σ is the growth rate and is equal to $f'(t)/f(t)$.

As $M_1 \gg M_2$ and $M_2 = b^2/(12\,\eta_2)$, we simplify the equation above and obtain

$$-\gamma M_2\frac{n^3-n}{R(t)^3}+\frac{Q(n-1)}{2\pi R(t)^2}=\sigma.$$

Setting the derivative of the growth rate to zero:

$$\frac{\partial\sigma}{\partial n}=0=-\gamma M_2\frac{3{n_{max}}^2-1}{R(t)^3}+\frac{Q}{2\pi R(t)^2}.$$

Rearranging to find n_{max}

$${n_{max}}^2=\frac{1}{3}\frac{QR(t)}{2\pi M_2\gamma}+1.$$

As

$$Ca=\frac{\dot{R}\eta_2}{\gamma}=\frac{6Q\eta_2}{12\pi\gamma R},$$

we can express n_{max} in terms of Ca:

$$n_{max} = \frac{1}{\sqrt{3}}\left[12Ca\frac{R(t)^2}{b^2} + 1\right]^{\frac{1}{2}}. \tag{2.32}$$

Appendix. B Supporting information for “Impact of soluble surfactants on liquid jets”

B.1 Derivation of Eq. (3.22), the expression of $\delta\Gamma$

Eq. (3.10), Eq. (3.17), and Eq (3.18) are shown as follows,

$$\frac{\partial\tilde{\Gamma}}{\partial\tilde{t}}+\tilde{u}\frac{\partial\tilde{\Gamma}}{\partial\tilde{z}}+\frac{\tilde{\Gamma}}{2}\frac{\partial\tilde{u}}{\partial\tilde{z}}=\frac{1}{Pe}\frac{\partial^2\tilde{\Gamma}}{\partial\tilde{z}^2}+\frac{\tilde{\Gamma}_\infty-\tilde{\Gamma}}{\tau_a}-\frac{\tilde{\Gamma}}{\tau_d}\exp\left(-\tilde{\beta}\tilde{\Gamma}/\tilde{E}_0\right), \tag{3.10}$$

$$\tilde{u}(\tilde{z},\tilde{t})=\delta\tilde{u}e^{\sigma\tilde{t}+ik\tilde{z}}, \tag{3.17}$$

$$\tilde{\Gamma}(\tilde{z},\tilde{t})=1+\delta\tilde{\Gamma}e^{\sigma\tilde{t}+ik\tilde{z}}, \tag{3.18}$$

Note that we have already solved the expression of $\delta\tilde{u}$ to be

$$\delta\tilde{u}=\frac{2i\sigma\varepsilon}{k}$$

The base state of Eq. (3.12) is

$$0=\frac{1}{\tau_a}\left(\tilde{\Gamma}_\infty-1\right)-\frac{1}{\tau_d}\exp\left(-\tilde{\beta}\tilde{\Gamma}/\tilde{E}_0\right)$$

Substituting Eq. (3.17) and Eq. (3.18) into Eq. (3.10) to obtain the perturbed state

$$\begin{aligned}\delta\tilde{\Gamma}\sigma e^{\sigma\tilde{t}+ik\tilde{z}}+\tilde{u}\delta\tilde{\Gamma}ike^{\sigma\tilde{t}+ik\tilde{z}}+\frac{1}{2}\left(1+\delta\tilde{\Gamma}e^{\sigma\tilde{t}+ik\tilde{z}}\right)\delta\tilde{u}ike^{\sigma\tilde{t}+ik\tilde{z}}&\\ =-\frac{1}{Pe}\delta\tilde{\Gamma}k^2e^{\sigma\tilde{t}+ik\tilde{z}}+\frac{1}{\tau_a}\left(\tilde{\Gamma}_\infty-1-\delta\tilde{\Gamma}e^{\sigma\tilde{t}+ik\tilde{z}}\right)&\\ -\frac{1+\delta\tilde{\Gamma}e^{\sigma\tilde{t}+ik\tilde{z}}}{\tau_d}\exp\left(-\tilde{\beta}/\tilde{E}_0\right)\exp\left(-\tilde{\beta}/\tilde{E}_0\delta\tilde{\Gamma}e^{\sigma\tilde{t}+ik\tilde{z}}\right)&\end{aligned}$$

Taking only the leading order terms to obtain

$$\sigma\delta\tilde{\Gamma}e^{\sigma\tilde{t}+ik\tilde{z}}+\frac{1}{2}\tilde{u}_0 ike^{\sigma\tilde{t}+ik\tilde{z}}$$

$$=-\frac{1}{Pe}k^2\,\delta\tilde{\Gamma}e^{\sigma\tilde{t}+ik\tilde{z}}+\frac{\tilde{\Gamma}_\infty-1}{\tau_a}-\frac{\delta\tilde{\Gamma}}{\tau_a}e^{\sigma\tilde{t}+ik\tilde{z}}$$

$$-\frac{1+\delta\tilde{\Gamma}e^{\sigma\tilde{t}+ik\tilde{z}}}{\tau_d}\exp\left(-\tilde{\beta}/\tilde{E}_0\right)\exp\left(-\tilde{\beta}/\tilde{E}_0\delta\tilde{\Gamma}e^{\sigma\tilde{t}+ik\tilde{z}}\right)$$

Assume $\tilde{\beta}\tilde{E}_0\delta\tilde{\Gamma}e^{\sigma\tilde{t}+ik\tilde{z}}\approx 0$, then

$$\exp\left(-\tilde{\beta}/\tilde{E}_0\delta\tilde{\Gamma}e^{\sigma\tilde{t}+ik\tilde{z}}\right)=1-\tilde{\beta}/\tilde{E}_0\delta\tilde{\Gamma}e^{\sigma\tilde{t}+ik\tilde{z}}$$

Thus, the equation becomes

$$\sigma\delta\tilde{\Gamma}e^{\sigma\tilde{t}+ik\tilde{z}}+\frac{1}{2}\tilde{u}_0 ike^{\sigma\tilde{t}+ik\tilde{z}}$$

$$=-\frac{1}{Pe}k^2\,\delta\tilde{\Gamma}e^{\sigma\tilde{t}+ik\tilde{z}}+\frac{\tilde{\Gamma}_\infty-1}{\tau_a}-\frac{\delta\tilde{\Gamma}}{\tau_a}e^{\sigma\tilde{t}+ik\tilde{z}}-\frac{\exp\left(-\tilde{\beta}/\tilde{E}_0\right)}{\tau_d}$$

$$-\frac{\exp\left(-\tilde{\beta}/\tilde{E}_0\right)}{\tau_d}\delta\tilde{\Gamma}e^{\sigma\tilde{t}+ik\tilde{z}}+\frac{1}{\tau_d}\exp\left(-\tilde{\beta}/\tilde{E}_0\right)\tilde{\beta}/\tilde{E}_0\delta\tilde{\Gamma}e^{\sigma\tilde{t}+ik\tilde{z}}$$

$$+\frac{\delta\tilde{\Gamma}e^{\sigma\tilde{t}+ik\tilde{z}}}{\tau_d}\exp\left(-\tilde{\beta}/\tilde{E}_0\right)\tilde{\beta}/\tilde{E}_0\delta\tilde{\Gamma}e^{\sigma\tilde{t}+ik\tilde{z}}$$

Taking the leading order and subtracting the base state to obtain

$$\sigma\delta\tilde{\Gamma}e^{\sigma\tilde{t}+ik\tilde{z}}+\frac{1}{2}\tilde{u}_0 ike^{\sigma\tilde{t}+ik\tilde{z}}$$

$$=-\frac{1}{Pe}k^2\,\delta\tilde{\Gamma}e^{\sigma\tilde{t}+ik\tilde{z}}-\frac{\delta\tilde{\Gamma}}{\tau_a}e^{\sigma\tilde{t}+ik\tilde{z}}+\frac{\left(\tilde{\beta}/\tilde{E}_0-1\right)\exp\left(-\tilde{\beta}/\tilde{E}_0\right)}{\tau_d}\delta\tilde{\Gamma}e^{\sigma\tilde{t}+ik\tilde{z}}$$

Canceling$e^{\sigma\tilde{t}+ik\tilde{z}}$, substituting $\delta\tilde{u}$, and reorganizing to obtain Eq. (3.22)

$$\delta\tilde{\Gamma} = \frac{\sigma\varepsilon}{\sigma + \frac{k^2}{Pe} + \frac{1}{\tau_a} + \frac{\left(1 - \tilde{\beta}/\tilde{E}_0\right)\exp\left(-\tilde{\beta}/\tilde{E}_0\right)}{\tau_d}}$$

B.2 Derivation of Eq. (3.23), the dispersion relation between σ and k

Eq. (3.9), Eq. (3.16) - (3.22) are shown as follows

$$\frac{\partial\tilde{u}}{\partial\tilde{t}} + \tilde{u}\frac{\partial\tilde{u}}{\partial\tilde{z}} = -\frac{\partial(\tilde{\gamma}\tilde{\kappa})}{\partial\tilde{z}} + \frac{2}{\tilde{R}}\frac{\partial\tilde{\gamma}}{\partial\tilde{z}} + \frac{3Oh}{\tilde{R}^2}\frac{\partial}{\partial\tilde{z}}\left(\tilde{R}^2\frac{\partial\tilde{u}}{\partial\tilde{z}}\right) + \frac{Oh}{2\tilde{R}^2}\frac{\partial}{\partial\tilde{z}}\left(Bq_d\tilde{R}\frac{\partial\tilde{u}}{\partial\tilde{z}}\right) + \frac{9Oh}{2\tilde{R}^2}\frac{\partial}{\partial\tilde{z}}\left(Bq_s\tilde{R}\frac{\partial\tilde{u}}{\partial\tilde{z}}\right), \tag{3.9}$$

$$\tilde{R}(\tilde{z},\tilde{t}) = 1 + \varepsilon e^{\sigma\tilde{t}+ik\tilde{z}}, \tag{3.14}$$

$$\tilde{u}(\tilde{z},\tilde{t}) = \delta\tilde{u}e^{\sigma\tilde{t}+ik\tilde{z}}, \tag{3.15}$$

$$\tilde{\Gamma}(\tilde{z},\tilde{t}) = 1 + \delta\tilde{\Gamma}e^{\sigma\tilde{t}+ik\tilde{z}}, \tag{3.16}$$

$$\tilde{\gamma} = 1 - \tilde{E}_0\tilde{\Gamma} + \tilde{\beta}\tilde{\Gamma}^2/2 \tag{3.17}$$

$$\delta\tilde{u} = \frac{2i\sigma\varepsilon}{k}, \tag{3.19}$$

$$\delta\tilde{\Gamma} = \frac{\sigma\varepsilon}{\sigma + k^2/Pe + 1/\tau_a + (1 - \tilde{\beta}/\tilde{E}_0)\exp(-\tilde{\beta}/\tilde{E}_0)/\tau_d}, \tag{3.20}$$

We can solve for the perturbed $\tilde{\kappa}$ by substituting the perturbed $\tilde{R}(\tilde{z},\tilde{t})$ and keep the leading order terms to obtain

$$\tilde{\kappa} = 1 - \varepsilon e^{\sigma\tilde{t}+ik\tilde{z}} + \varepsilon k^2 e^{\sigma\tilde{t}+ik\tilde{z}}$$

Assuming Bq_s and Bq_d are constant and simplify Eq. (3.9) to obtain

$$\frac{\partial \tilde{u}}{\partial \tilde{t}} + \tilde{u}\frac{\partial \tilde{u}}{\partial \tilde{z}} = -\tilde{\kappa}\frac{\partial \tilde{\gamma}}{\partial \tilde{z}} - \tilde{\gamma}\frac{\partial \tilde{\kappa}}{\partial \tilde{z}} + \frac{2}{\tilde{R}}\frac{\partial \tilde{\gamma}}{\partial \tilde{z}} + 3Oh\frac{\tilde{R}^2}{\tilde{R}^2}\frac{\partial^2 \tilde{u}}{\partial \tilde{z}^2} + 3Oh\frac{1}{\tilde{R}^2}\frac{\partial \tilde{u}}{\partial z}\frac{\partial \tilde{R}^2}{\partial \tilde{z}}$$

$$+ (Bq_d + 9Bq_s)\frac{Oh\tilde{R}}{2\tilde{R}^2}\frac{\partial^2 \tilde{u}}{\partial \tilde{z}^2} + (Bq_d + 9Bq_s)\frac{Oh}{2\tilde{R}^2}\frac{\partial \tilde{u}}{\partial \tilde{z}}\frac{\partial \tilde{R}}{\partial \tilde{z}}$$

Taking only the leading order terms to obtain

$$\frac{\partial \tilde{u}}{\partial \tilde{t}} = -\tilde{\kappa}\frac{\partial \tilde{\gamma}}{\partial \tilde{z}} - \tilde{\gamma}\frac{\partial \tilde{\kappa}}{\partial \tilde{z}} + \frac{2}{\tilde{R}}\frac{\partial \tilde{\gamma}}{\partial \tilde{z}} + 3Oh\frac{\tilde{R}^2}{\tilde{R}^2}\frac{\partial^2 \tilde{u}}{\partial \tilde{z}^2} + (Bq_d + 9Bq_s)\frac{Oh\tilde{R}}{2\tilde{R}^2}\frac{\partial^2 \tilde{u}}{\partial \tilde{z}^2}$$

Substitute in Eq. (3.16) - Eq. (3.21) to obtain

$$\delta\tilde{u}\sigma e^{\sigma\tilde{t}+ik\tilde{z}} = -\left(1 - \varepsilon e^{\sigma\tilde{t}+ik\tilde{z}} + \varepsilon k^2 e^{\sigma\tilde{t}+ik\tilde{z}}\right)\left(\tilde{\beta} - \tilde{E}_0\right)ik\delta\tilde{\Gamma}e^{\sigma\tilde{t}+ik\tilde{z}}$$

$$-\left(1 - \tilde{E}_0\left(1 + \delta\tilde{\Gamma}e^{\sigma\tilde{t}+ik\tilde{z}}\right) + \frac{\tilde{\beta}}{2}\left(1 + 2\delta\tilde{\Gamma}e^{\sigma\tilde{t}+ik\tilde{z}}\right)\right)(-k + k^3)\varepsilon i e^{\sigma\tilde{t}+ik\tilde{z}}$$

$$-\frac{2}{\tilde{R}}\left(\tilde{\beta} - \tilde{E}_0\right)ik\delta\tilde{\Gamma}e^{\sigma\tilde{t}+ik\tilde{z}} - 3Oh\delta\tilde{u}k^2 e^{\sigma\tilde{t}+ik\tilde{z}} - (Bq_d + 9Bq_s)\frac{Oh}{2\tilde{R}}\delta\tilde{u}k^2 e^{\sigma\tilde{t}+ik\tilde{z}}$$

Note that all the $1/\tilde{R}$ terms can be simplified by taking the leading order terms as follows

$$\frac{1}{\tilde{R}} = \frac{1}{1 + \varepsilon e^{\sigma\tilde{t}+ik\tilde{z}}} = \frac{1 - \varepsilon e^{\sigma\tilde{t}+ik\tilde{z}}}{1^2 - \left(\varepsilon e^{\sigma\tilde{t}+ik\tilde{z}}\right)^2} = 1 - \varepsilon e^{\sigma\tilde{t}+ik\tilde{z}}$$

Simplify to only the leading order terms and divide $e^{\sigma t+ikz}$ to obtain

$$\sigma\,\delta\tilde{u} = -\left(\tilde{\beta} - \tilde{E}_0\right)ik\delta\tilde{\Gamma} - \left(1 - \tilde{E}_0 + \frac{\tilde{\beta}}{2}\right)(-k + k^3)\varepsilon i + 2\left(\tilde{\beta} - \tilde{E}_0\right)ik\delta\tilde{\Gamma}$$

$$-(6 + Bq_d + 9Bq_s)\frac{Oh}{2}\,\delta\tilde{u}k^2$$

Substitute $\delta\tilde{u}$ and $\delta\tilde{\Gamma}$ to obtain

$$\sigma\frac{2i\sigma\varepsilon}{k} = \left(\tilde{\beta}-\tilde{E}_0\right)ik\frac{\sigma\varepsilon}{\sigma+\frac{k^2}{Pe}+\frac{1}{\tau_a}+\frac{\left(1-\tilde{\beta}/\tilde{E}_0\right)\exp\left(-\tilde{\beta}/\tilde{E}_0\right)}{\tau_d}}+\left(1-\tilde{E}_0+\frac{\tilde{\beta}}{2}\right)(k-k^3)\varepsilon i$$

$$-(6+Bq_d+9Bq_s)\frac{Oh}{2}\frac{2i\sigma\varepsilon}{k}k^2$$

Multiplies both sides by $k/\sigma i\varepsilon$ and reorganize to obtain Eq. (3.23)

$$2\sigma = \left(1-\tilde{E}_0+\frac{\tilde{\beta}}{2}\right)\frac{k^2-k^4}{\sigma}+\frac{\left(\tilde{\beta}-\tilde{E}_0\right)k^2}{\sigma+\frac{k^2}{Pe}+\frac{1}{\tau_a}+\frac{\left(1-\frac{\tilde{\beta}}{\tilde{E}_0}\right)\exp\left(-\frac{\tilde{\beta}}{\tilde{E}_0}\right)}{\tau_d}}$$
$$-(6+Bq_d+9Bq_s)Ohk^2 \qquad (3.23)$$

B.3 linear analysis on the impact of Pe

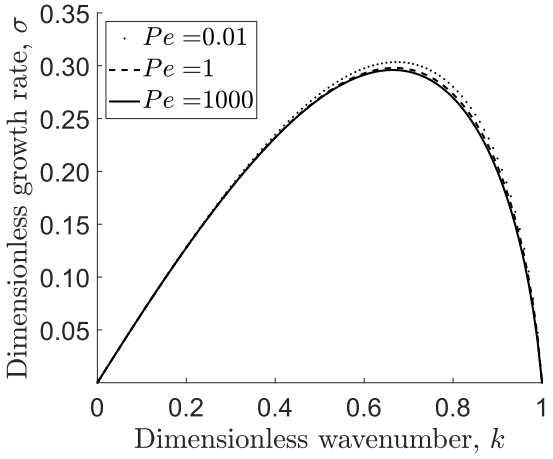

Figure 8. Stability of jets with $\tilde{E}_0 = 0.01$, $\tau_s = 1$, $Oh = 0.04$, $Bq_d = 1$, $Bq_s = 0$, at different values of Pe. As Pe increases, the system becomes more stable.

B.4 Elastic liquid jet with insoluble surfactants

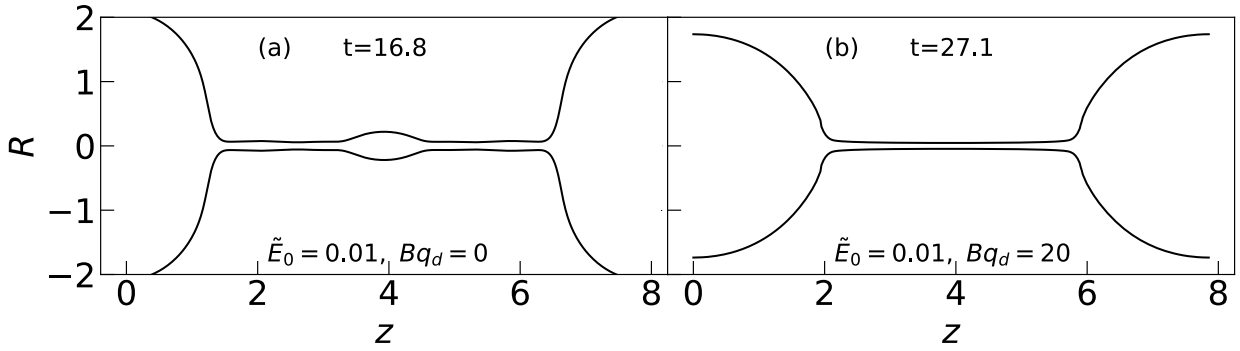

B. 1 Viscoelastic jets with $\tilde{E}_0 = 0.01, \tau_s = 0.05,\ Oh = 0.04, De = 0.8, Bq_s = 0, Pe = 1000$ at (a) $Bq_d = 0,, (b) Bq_s = 20$. As Bq_s increases, the system becomes more stable and does not form satellite beads throughout the process.

B.5 Additional jet fluid instability simulations

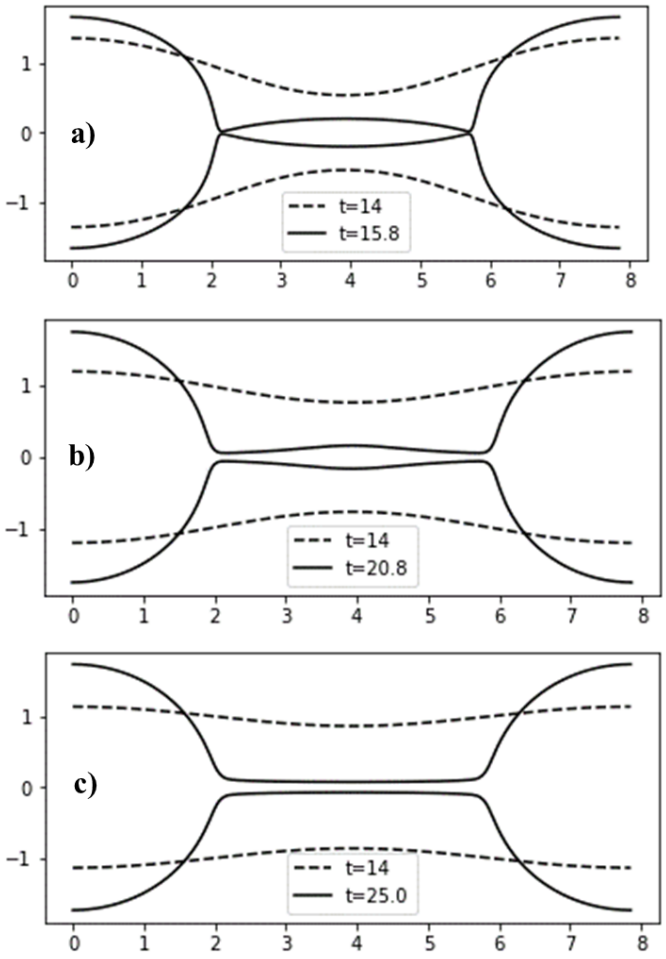

B. 2 The development of Newtonian jets using the Langmuir model at$k = 0.8$, $E_0 = 0.01$, $\tau_s = 0.01$ and a). $Bq_d = 0$, b) $Bq_d = 10$, and c) $Bq_d = 20$.

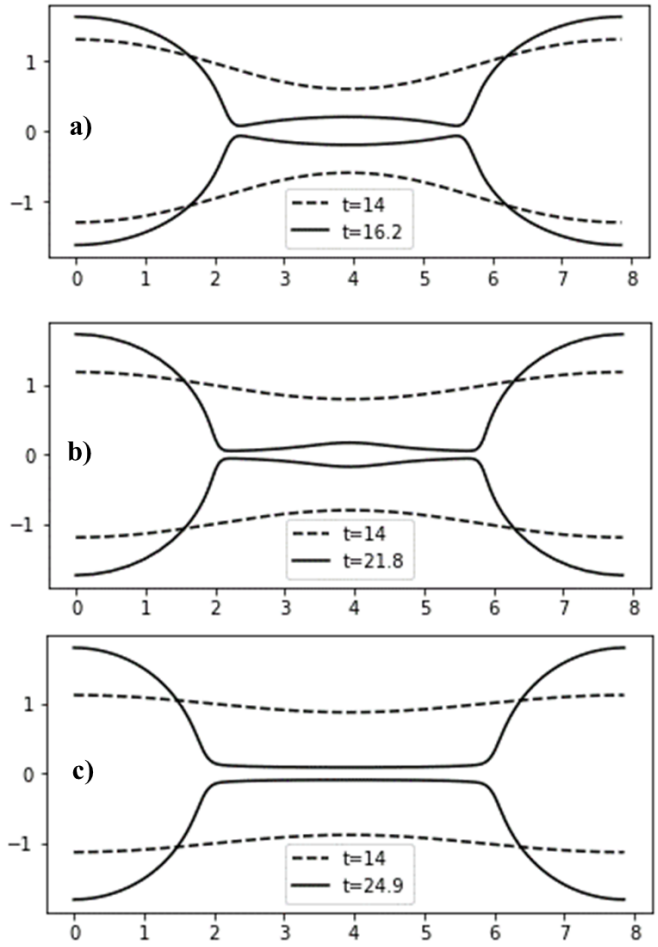

B. 3 The development of Newtonian jets using the Frumkin model at $k = 0.8$, $\beta = -0.1$, $E_0 = 0.01$, $\tau_s = 0.01$ and a). $Bq_d = 0$, b) $Bq_d = 10$, and c) $Bq_d = 20$.

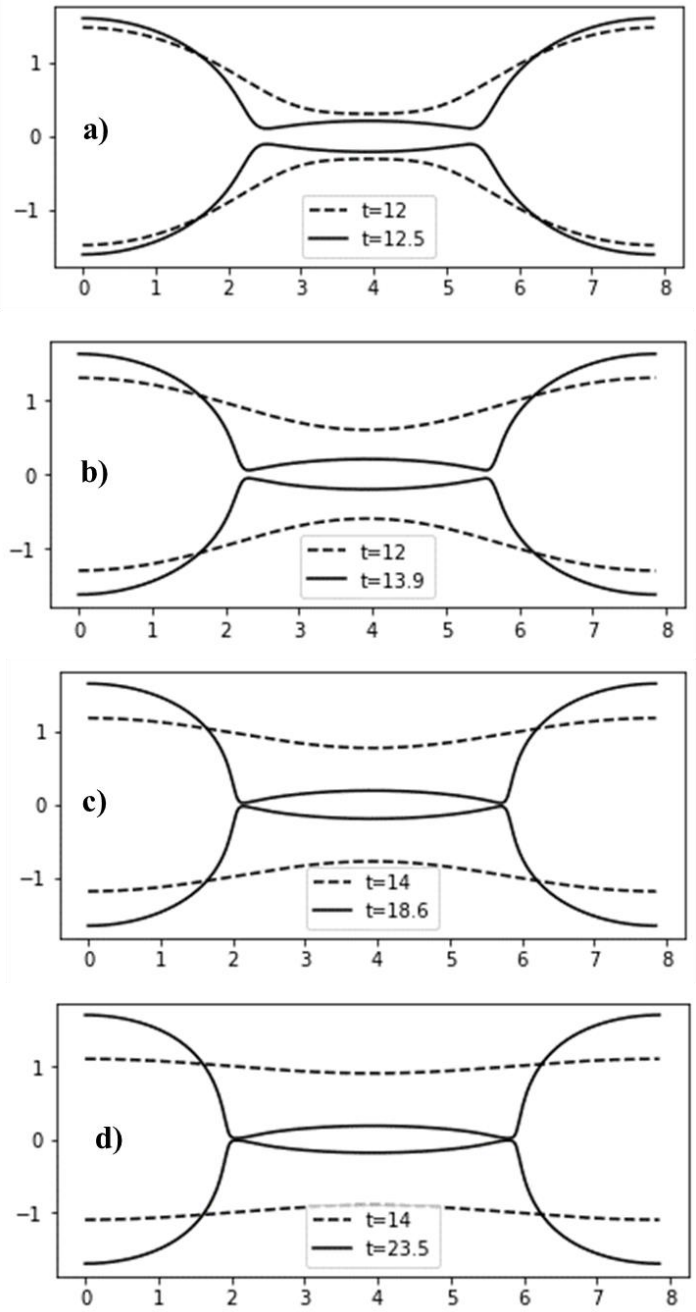

B. 4 The development of Newtonian jets using the Frumkin model at $k = 0.8$, $Bq_d = 0$, $E_0 = 0.01$, $\tau_s = 0.01$ and a) $\beta = 1$, b) $\beta = 0.5$, c) $\beta = -0.5$, and d) $\beta = -1$.

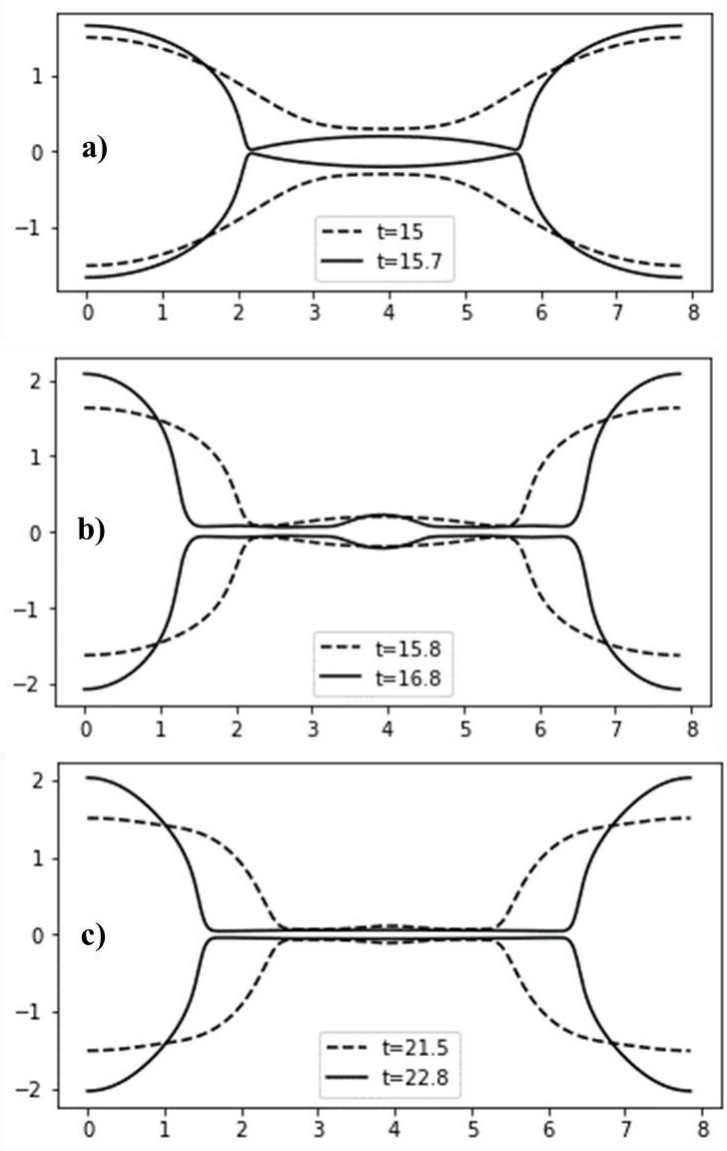

B. 5 The development of Newtonian jets using the Langmuir model at $k = 0.8$, $Bq_d = 0$, $\tau_s = 0.01$ and a) $E_0 = 0$, b) $E_0 = 0.01$, and c) $E_0 = 0.1$.

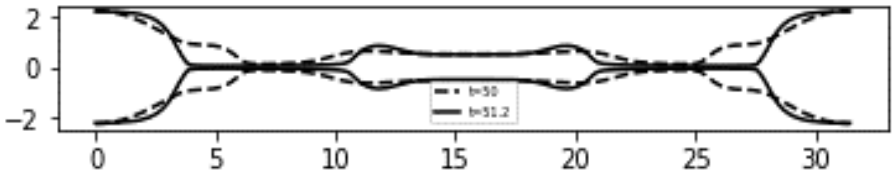

B. 6 The development of Newtonian jets using the Langmuir model at $k = 0.2$, $Bq_d = 20$, $E_0 = 0.01$, $\tau_s = 0.01$.

References

[1] L. E. Scriven and C. V. Sternling, *The Marangoni Effects*, Nature **187**, 186 (1960).

[2] H. Manikantan and T. M. Squires, *Surfactant Dynamics: Hidden Variables Controlling Fluid Flows*, J. Fluid Mech. **892**, 1 (2020).

[3] V. G. Levich and D. B. Spalding, *Physicochemical Hydrodynamics* (Prentice-Hall Inc., 1962).

[4] K. Koczo, L. A. Lobo, and D. T. Wasan, *Effect of Oil on Foam Stability: Aqueous Foams Stabilized by Emulsions*, J. Colloid Interface Sci. **150**, 492 (1992).

[5] D. Langevin, *Rheology of Adsorbed Surfactant Monolayers at Fluid Surfaces*, Annu. Rev. Fluid Mech. **46**, 47 (2014).

[6] Z. A. Zell, A. Nowbahar, V. Mansard, L. G. Leal, S. S. Deshmukh, J. M. Mecca, C. J. Tucker, and T. M. Squires, *Surface Shear Inviscidity of Soluble Surfactants*, Proc. Natl. Acad. Sci. U. S. A. **111**, 3677 (2014).

[7] N. Jaensson and J. Vermant, *Tensiometry and Rheology of Complex Interfaces*, Curr. Opin. Colloid Interface Sci. **37**, 136 (2018).

[8] G. G. Fuller and J. Vermant, *Complex Fluid-Fluid Interfaces: Rheology and Structure*, Annu. Rev. Chem. Biomol. Eng. **3**, 519 (2012).

[9] G. J. Elfring, L. G. Leal, and T. M. Squires, *Surface Viscosity and Marangoni Stresses at Surfactant Laden Interfaces*, J. Fluid Mech. **792**, 712 (2016).

[10] M. J. Boussinesq, *Speed of the Slow, Uniform Fall of a Liquid Spherical Drop in a*

Viscous Fluid of Lesser Specific Weight., Ann. Chim. Phys. **29**, 364 (1913).

[11] L. E. Scriven, *Dynamics of a Fluid Interface*, Chem. Eng. Sci. **12**, 98 (1960).

[12] S. A. Koehler, S. Hilgenfeldt, and H. A. Stone, *Liquid Flow through Aqueous Foams: The Node-Dominated Foam Drainage Equation*, Phys. Rev. Lett. **82**, 4232 (1999).

[13] M. Durand and D. Langevin, *Physicochemical Approach to the Theory of Foam Drainage*, Eur. Phys. J. E **7**, 35 (2002).

[14] M. S. Bhamla, C. E. Giacomin, C. Balemans, and G. G. Fuller, *Influence of Interfacial Rheology on Drainage from Curved Surfaces*, Soft Matter **10**, 6917 (2014).

[15] V. Narsimhan, *Letter: The Effect of Surface Viscosity on the Translational Speed of Droplets*, Phys. Fluids **30**, (2018).

[16] T. M. Fischer, M. Sickert, and F. Rondelez, *Comment on "Shear Viscosity of Langmuir Monolayers in the Low-Density Limit" [3] (Multiple Letters)*, Phys. Rev. Lett. **92**, 139603 (2004).

[17] M. Sickert and F. Rondelez, *Shear Viscosity of Langmuir Monolayers in the Low-Density Limit*, Phys. Rev. Lett. **90**, 4 (2003).

[18] P. Stevenson, *Remarks on the Shear Viscosity of Surfaces Stabilised with Soluble Surfactants*, J. Colloid Interface Sci. **290**, 603 (2005).

[19] T. Verwijlen, P. Moldenaers, H. A. Stone, and J. Vermant, *Study of the Flow Field in the Magnetic Rod Interfacial Stress Rheometer*, Langmuir **27**, 9345 (2011).

[20] V. Prasad, S. A. Koehler, and E. R. Weeks, *Two-Particle Microrheology of Quasi-2D Viscous Systems*, Phys. Rev. Lett. **97**, 1 (2006).

[21] P. Cicuta and A. M. Donald, *Microrheology: A Review of the Method and Applications*, Soft Matter **3**, 1449 (2007).

[22] J. A. McGlynn, N. Wu, and K. M. Schultz, *Multiple Particle Tracking Microrheological Characterization: Fundamentals, Emerging Techniques and Applications*, J. Appl. Phys. **127**, 201101 (2020).

[23] J. R. Samaniuk and J. Vermant, *Micro and Macrorheology at Fluid-Fluid Interfaces*, Soft Matter **10**, 7023 (2014).

[24] J. Lucassen and R. S. Hansen, *Damping of Waves on Monolayer-Covered Surfaces. I. Systems with Negligible Surface Dilational Viscosity*, J. Colloid Interface Sci. **22**, 32 (1966).

[25] K. J. Stebe and D. Barthès-Biesel, *Marangoni Effects of Adsorption—Desorption Controlled Surfactants on the Leading End of an Infinitely Long Bubble in a Capillary*, J. Fluid Mech. **286**, 25 (1995).

[26] S. Q. Choi, S. Steltenkamp, J. A. Zasadzinski, and T. M. Squires, *Active Microrheology and Simultaneous Visualization of Sheared Phospholipid Monolayers*, Nat. Commun. **2**, (2011).

[27] D. Renggli, A. Alicke, R. H. Ewoldt, and J. Vermant, *Operating Windows for Oscillatory Interfacial Shear Rheology*, J. Rheol. (N. Y. N. Y). **64**, 141 (2020).

[28] A. P. Kotula and S. L. Anna, *Insoluble Layer Deposition and Dilatational Rheology at a Microscale Spherical Cap Interface*, Soft Matter **12**, 7038 (2016).

[29] Simone Stewart, *Schlieren Imaging of Viscous Fingering and Buoyancy Driven*

Convection, https://art-csep.cnsi.ucsb.edu/gallery/schlieren-imaging-viscous-fingering-and-buoyancy-driven-convection.

[30] R. Farajzadeh, A. Andrianov, R. Krastev, G. J. Hirasaki, and W. R. Rossen, *Foam-Oil Interaction in Porous Media: Implications for Foam Assisted Enhanced Oil Recovery*, Adv. Colloid Interface Sci. **183**–**184**, 1 (2012).

[31] A. Andrianov, R. Farajzadeh, M. Mahmoodi Nick, M. Talanana, and P. L. J. Zitha, *Immiscible Foam for Enhancing Oil Recovery: Bulk and Porous Media Experiments*, Ind. Eng. Chem. Res. **51**, 2214 (2012).

[32] P. G. . Saffman and G. Taylor, *The Penetration of a Fluid into a Porous Medium or Hele-Shaw Cell Containing a More Viscous Liquid*, Proc. R. Soc. London. Ser. A. Math. Phys. Sci. **245**, 312 (1958).

[33] J. W. Mclean and P. G. Saffman, *The Effect of Surface Tension on the Shape of Fingers in a Hele Shaw Cell*, J. Fluid Mech. **102**, 455 (1981).

[34] C. W. Park and G. M. Homsy, *Two-Phase Displacement in Hele Shaw Cells: Theory*, J. Fluid Mech. **139**, 291 (1984).

[35] L. Schwartz, *Stability of Hele–Shaw Flows: The Wetting-layer Effect*, Phys. Fluids **29**, 3086 (1986).

[36] H. Tani and A. Tani, *Effect of the Wetting Layer on the Fingering Pattern in a Hele-Shaw Cell*, J. Phys. Soc. Japan **83**, 2 (2014).

[37] T. Maxworthy, *Experimental Study of Interface Instability in a Hele-Shaw Cell*, Phys. Rev. A **39**, 5863 (1989).

[38] H. Kim, T. Funada, D. D. Joseph, and G. M. Homsy, *Viscous Potential Flow Analysis of Radial Fingering in a Hele-Shaw Cell*, Phys. Fluids **21**, (2009).

[39] T. T. Al-Housseiny, P. A. Tsai, and H. A. Stone, *Control of Interfacial Instabilities Using Flow Geometry*, Nat. Phys. **8**, 747 (2012).

[40] H. S. Rabbani, D. Or, Y. Liu, C. Y. Lai, N. B. Lu, S. S. Datta, H. A. Stone, and N. Shokri, *Suppressing Viscous Fingering in Structured Porous Media*, Proc. Natl. Acad. Sci. U. S. A. **115**, 4833 (2018).

[41] D. Pihler-Puzović, P. Illien, M. Heil, and A. Juel, *Suppression of Complex Fingerlike Patterns at the Interface between Air and a Viscous Fluid by Elastic Membranes*, Phys. Rev. Lett. **108**, 1 (2012).

[42] T. Gao, M. Mirzadeh, P. Bai, K. M. Conforti, and M. Z. Bazant, *Active Control of Viscous Fingering Using Electric Fields*, Nat. Commun. **10**, 1 (2019).

[43] G. Lin, J. M. Frostad, and G. G. Fuller, *Influence of Interfacial Elasticity on Liquid Entrainment in Thin Foam Films*, Phys. Rev. Fluids **3**, 114001 (2018).

[44] A. K. Sachan, S. Q. Choi, K. H. Kim, Q. Tang, L. Hwang, K. Y. C. Lee, T. M. Squires, and J. A. Zasadzinski, *Interfacial Rheology of Coexisting Solid and Fluid Monolayers*, Soft Matter **13**, 1481 (2017).

[45] P. Tchoukov, F. Yang, Z. Xu, T. Dabros, J. Czarnecki, and J. Sjöblom, *Role of Asphaltenes in Stabilizing Thin Liquid Emulsion Films*, Langmuir **30**, 3024 (2014).

[46] D. Langevin and J. F. Argillier, *Interfacial Behavior of Asphaltenes*, Adv. Colloid Interface Sci. **233**, 83 (2016).

[47] C. C. Chang, A. Nowbahar, V. Mansard, I. Williams, J. Mecca, A. K. Schmitt, T. H. Kalantar, T. C. Kuo, and T. M. Squires, *Interfacial Rheology and Heterogeneity of Aging Asphaltene Layers at the Water-Oil Interface*, Langmuir **34**, 5409 (2018).

[48] M. Durand, G. Martinoty, and D. Langevin, *Liquid Flow through Aqueous Foams: From the Plateau Border-Dominated Regime to the Node-Dominated Regime*, Phys. Rev. E - Stat. Physics, Plasmas, Fluids, Relat. Interdiscip. Top. **60**, R6307 (1999).

[49] H. C. Burkholder and J. C. Berg, *Effect of Mass Transfer on Laminar Jet Breakup: Part I. Liquid Jets in Gases*, AIChE J. **20**, 863 (1974).

[50] S. Whitaker, *Studies of the Drop-Weight Method for Surfactant Solutions. III. Drop Stability, the Effect of Surfactants on the Stability of a Column of Liquid*, J. Colloid Interface Sci. **54**, 231 (1976).

[51] R. W. Coyle and J. C. Berg, *The Effects of Mass Transfer and Solute Adsorption on the Size of Drops Produced by Liquid-Liquid Jet Breakup*, Chem. Eng. Sci. **39**, 168 (1984).

[52] H. Wee, B. W. Wagoner, V. Garg, P. M. Kamat, and O. A. Basaran, *Pinch-off of a Surfactant-Covered Jet*, J. Fluid Mech. **908**, (2021).

[53] N. M. Kovalchuk, E. Nowak, and M. J. H. Simmons, *Effect of Soluble Surfactants on the Kinetics of Thinning of Liquid Bridges during Drops Formation and on Size of Satellite Droplets*, Langmuir **32**, 5069 (2016).

[54] A. Ponce-Torres, J. M. Montanero, M. A. Herrada, E. J. Vega, and J. M. Vega, *Influence of the Surface Viscosity on the Breakup of a Surfactant-Laden Drop*, Phys. Rev. Lett. **118**, 1 (2017).

[55] J. R. Walker and R. V. Calabrese, *Analysis of Surfactant Laden Liquid–Liquid Dispersion Using an Axisymmetric Laminar Jet*, Can. J. Chem. Eng. **89**, 1096 (2011).

[56] A. Alhushaybari and J. Uddin, *Absolute Instability of Free-Falling Viscoelastic Liquid Jets with Surfactants*, Phys. Fluids **32**, (2020).

[57] E. Antonopoulou, O. G. Harlen, M. Rump, T. Segers, and M. A. Walkley, *Effect of Surfactants on Jet Break-up in Drop-on-Demand Inkjet Printing*, Phys. Fluids **33**, (2021).

[58] P. M. Kamat, B. W. Wagoner, S. S. Thete, and O. A. Basaran, *Role of Marangoni Stress during Breakup of Surfactant-Covered Liquid Threads: Reduced Rates of Thinning and Microthread Cascades*, Phys. Rev. Fluids **3**, 043602 (2018).

[59] V. Dravid, S. Songsermpong, Z. Xue, C. M. Corvalan, and P. E. Sojka, *Two-Dimensional Modeling of the Effects of Insoluble Surfactant on the Breakup of a Liquid Filament*, Chem. Eng. Sci. **61**, 3577 (2006).

[60] Y. C. Liao, E. I. Franses, and O. A. Basaran, *Deformation and Breakup of a Stretching Liquid Bridge Covered with an Insoluble Surfactant Monolayer*, Phys. Fluids **18**, (2006).

[61] R. V. Craster, O. K. Matar, and D. T. Papageorgiou, *Pinchoff and Satellite Formation in Surfactant Covered Viscous Threads*, Phys. Fluids **14**, 1364 (2002).

[62] P. Bazazi, H. A. Stone, and S. H. Hejazi, *Dynamics of Droplet Pinch-Off at Emulsified Oil-Water Interfaces: Interplay between Interfacial Viscoelasticity and Capillary Forces*, Phys. Rev. Lett. **130**, 34001 (2023).

[63] A. M. Alsharif and J. Uddin, *Instability of Viscoelastic Curved Liquid Jets with Surfactants*, J. Nonnewton. Fluid Mech. **216**, 1 (2015).

[64] A. Martínez-Calvo and A. Sevilla, *Universal Thinning of Liquid Filaments under Dominant Surface Forces*, Phys. Rev. Lett. **125**, 114502 (2020).

[65] H. Wee, B. W. Wagoner, P. M. Kamat, and O. A. Basaran, *Effects of Surface Viscosity on Breakup of Viscous Threads*, Phys. Rev. Lett. **124**, 204501 (2020).

[66] E. Antonopoulou, O. G. Harlen, M. Rump, T. Segers, and M. A. Walkley, *Effect of Surfactants on Jet Break-up in Drop-on-Demand Inkjet Printing*, Phys. Fluids **33**, 072112 (2021).

[67] Y. C. Liao, H. J. Subramani, E. I. Franses, and O. A. Basaran, *Effects of Soluble Surfactants on the Deformation and Breakup of Stretching Liquid Bridges*, Langmuir **20**, 9926 (2004).

[68] A. Ponce-Torres, M. Rubio, M. A. Herrada, J. Eggers, and J. M. Montanero, *Influence of the Surface Viscous Stress on the Pinch-off of Free Surfaces Loaded with Nearly-Inviscid Surfactants*, Sci. Rep. **10**, 1 (2020).

[69] H. Diamant and D. Andelman, *Kinetics of Surfactant Adsorption at Fluid−Fluid Interfaces*, J. Phys. Chem. **100**, 13732 (1996).

[70] P. A. Kralchevsky, K. D. Danov, and N. D. Denkov, *Chemical Physics of Colloid Systems and Interfaces*, in *Handbook of Surface and Colloid Chemistry, Third Edition* (CRC Press, 2008), pp. 197–377.

[71] L. Paterson, *Radial Fingering in a Hele Shaw Cell*, J. Fluid Mech. **113**, 513 (1981).

[72] J. C. Slattery, L. Sagis, and E.-S. Oh, *Interfacial Transport Phenomena.*, 2nd ed. (Springer, 2007).

[73] See Supplemental Material at [URL] for Detailed Derivations., n.d.

[74] R. E. Kurtz, A. Lange, and G. G. Fuller, *Interfacial Rheology and Structure of Straight-Chain and Branched Fatty Alcohol Mixtures*, Langmuir **22**, 5321 (2006).

[75] D. Georgieva, V. Schmitt, F. Leal-Calderon, and D. Langevin, *On the Possible Role of Surface Elasticity in Emulsion Stability*, Langmuir **25**, 5565 (2009).

[76] D. Buzza, C. D. Lu, M. Cates, D. Buzza, C. D. Lu, M. C. Linear, S. Rheology, F. Journal, and D. Lu, *Linear Shear Rheology of Incompressible Foams To Cite This Version : HAL Id : Jpa-00248141*, **5**, 37 (1995).

[77] T. J. Stoodt and J. C. Slattery, *Effect of the Interfacial Viscosities upon Displacement*, AIChE J. **30**, 564 (1984).

[78] O. A. Logvinov, *Immiscible Viscous Fingering in an Annular Hele-Shaw Cell with a Source*, J. Porous Media **22**, 119 (2019).

[79] S. S. Cardoso and A. W. Woods, *The Formation of Drops through Viscous Instability*, J. Fluid Mech. **289**, 351 (1995).

[80] A. Hooshanginejad, B. C. Druecke, and S. Lee, *Stability Analysis of a Particle Band on the Fluid-Fluid Interface*, J. Fluid Mech. **869**, 1 (2019).

[81] E. O. Dias and J. A. Miranda, *Wavelength Selection in Hele-Shaw Flows: A Maximum-Amplitude Criterion*, Phys. Rev. E - Stat. Nonlinear, Soft Matter Phys. **88**, 1 (2013).

[82] E. O. Dias, E. Alvarez-Lacalle, M. S. Carvalho, and J. A. Miranda, *Minimization of Viscous Fluid Fingering: A Variational Scheme for Optimal Flow Rates*, Phys. Rev. Lett. **109**, 1 (2012).

[83] L. R. Arriaga, I. Löpez-Montero, J. Ignés-Mullol, and F. Monroy, *Domain-Growth Kinetic Origin of Nonhorizontal Phase Coexistence Plateaux in Langmuir Monolayers: Compression Rigidity of a Raft-like Lipid Distribution*, J. Phys. Chem. B **114**, 4509 (2010).

[84] D. Pihler-Puzović, A. Juel, G. G. Peng, J. R. Lister, and M. Heil, *Displacement Flows under Elastic Membranes. Part 1. Experiments and Direct Numerical Simulations*, J. Fluid Mech. **784**, 487 (2015).

[85] J. V. Fontana, A. Juel, N. Bergemann, M. Heil, and A. L. Hazel, *Modelling Finger Propagation in Elasto-Rigid Channels*, ArXiv (2020).

[86] A. Q. Shen, B. Gleason, G. H. McKinley, and H. A. Stone, *Fiber Coating with Surfactant Solutions*, Phys. Fluids **14**, 4055 (2002).

[87] B. Scheid, J. Delacotte, B. Dollet, E. Rio, F. Restagno, E. A. Van Nierop, I. Cantat, D. Langevin, and H. A. Stone, *The Role of Surface Rheology in Liquid Film Formation*, Europhys. Lett. **90**, 24002 (2010).

[88] S. M. Troian, E. Herbolzheimer, and S. A. Safran, *Model for the Fingering Instability of Spreading Surfactant Drops*, Phys. Rev. Lett. **65**, 333 (1990).

[89] A. A. Darhuber and S. M. Troian, *Principles of Microfluidic Actuation by Modulation of Surface Stresses*, Annu. Rev. Fluid Mech. **37**, 425 (2005).

[90] D. Langevin, *On the Rupture of Thin Films Made from Aqueous Surfactant Solutions*, Adv. Colloid Interface Sci. **275**, 102075 (2020).

[91] Z. Briceño-Ahumada, A. Maldonado, M. Impéror-Clerc, and D. Langevin, *On the*

Stability of Foams Made with Surfactant Bilayer Phases, Soft Matter **12**, 1459 (2016).

[92] M. Saad Bhamla, C. Chai, M. A. Àlvarez-Valenzuela, J. Tajuelo, and G. G. Fuller, *Interfacial Mechanisms for Stability of Surfactant-Laden Films*, PLoS One **12**, 1 (2017).

[93] O. A. Basaran, H. Gao, and P. P. Bhat, *Nonstandard Inkjets*, Annu. Rev. Fluid Mech. **45**, 85 (2013).

[94] C. F. Brooks, G. G. Fuller, C. W. Frank, and C. R. Robertson, *Interfacial Stress Rheometer to Study Rheological Transitions in Monolayers at the Air-Water Interface*, Langmuir **15**, 2450 (1999).

[95] D. O. Johnson and K. J. Stebe, *Oscillating Bubble Tensiometry: A Method for Measuring the Surfactant Adsorptive-Desorptive Kinetics and the Surface Dilatational Viscosity*, J. Colloid Interface Sci. **168**, 21 (1994).

[96] H. A. Stone and H. Masoud, *Mobility of Membrane-Trapped Particles*, J. Fluid Mech. **781**, 494 (2015).

[97] A. Martínez-Calvo and A. Sevilla, *Temporal Stability of Free Liquid Threads with Surface Viscoelasticity*, J. Fluid Mech. **846**, 877 (2018).

[98] F. Li and D. He, *Dynamics of a Surfactant-Laden Viscoelastic Thread in the Presence of Surface Viscosity*, (2023).

[99] J. Eggers, *Nonlinear Dynamics and Breakup of Free-Surface Flows*, Rev. Mod. Phys. **69**, 1 (1997).

[100] M. G. Forest and Q. Wang, *Change-of-Type Behavior in Viscoelastic Slender Jet Models*, Theor. Comput. Fluid Dyn. **2**, 1 (1990).

[101] A. M. Ardekani, V. Sharma, and G. H. McKinley, *Dynamics of Bead Formation, Filament Thinning and Breakup in Weakly Viscoelastic Jets*, J. Fluid Mech. **665**, 46 (2010).

[102] M. Durand and H. A. Stone, *Relaxation Time of the Topological T1 Process in a Two-Dimensional Foam*, Phys. Rev. Lett. **97**, 1 (2006).

[103] A. P. Adamson, Arthur W and Gast, *Physical Chemistry of Surfaces*, Wiley **524**, (1990).

[104] Lord Rayleigh, *On The Instability Of Jets*, Proc. London Math. Soc. **s1**-**10**, 4 (1878).

[105] M. L. E. Timmermans and J. R. Lister, *The Effect of Surfactant on the Stability of a Liquid Thread*, J. Fluid Mech. **459**, 289 (2002).

[106] Lord Rayleigh, *On the Stability of a Cylinder of Viscous Liquid under Capillary Force.*, Phil. Mag. **34**, (1892).

[107] K. J. Stebe and C. Maldarelli, *Remobilizing Surfactant Retarded Fluid Particle Interfaces. II. Controlling the Surface Mobility at Interfaces of Solutions Containing Surface Active Components*, Journal of Colloid And Interface Science.

[108] Y. Zhang, G. Hu, Y. Liu, J. Wang, G. Yang, and D. Li, *Suppression and Utilization of Satellite Droplets for Inkjet Printing: A Review*, Processes **10**, (2022).

[109] U. Sen, C. Datt, T. Segers, H. Wijshoff, J. H. Snoeijer, M. Versluis, and D. Lohse, *The Retraction of Jetted Slender Viscoelastic Liquid Filaments*, J. Fluid Mech. **929**, 1 (2021).

[110] H. Giesekus, *A Simple Constitutive Equation for Polymer Fluids Based on the Concept of Deformation-Dependent Tensorial Mobility*, J. Nonnewton. Fluid Mech. **11**, 69 (1982).

[111] N. J. Alvarez, S. L. Anna, T. Saigal, R. D. Tilton, and L. M. Walker, *Interfacial Dynamics and Rheology of Polymer-Grafted Nanoparticles at Air-Water and Xylene-Water*

Interfaces, Langmuir **28**, 8052 (2012).

[112] K. Kim, S. Q. Choi, J. A. Zasadzinski, and T. M. Squires, *Interfacial Microrheology of DPPC Monolayers at the Air-Water Interface*, Soft Matter **7**, 7782 (2011).